The Stellar Initial Mass Function and Total Mass Profiles of Early-Type Galaxies

By

Adriano Poci

Supervised by: Dr Richard McDermid

A thesis submitted to Macquarie University

for the degree of Master of Research

Department of Physics

December 2015

Examiner's Copy

Typeset in LaTeX 2_ε.

Except where acknowledged in the customary manner, the material presented in this thesis is, to the best of my knowledge, original and has not been submitted in whole or part for a degree in any university.

Adriano Poci

Acknowledgements

I thank my family for putting up with me in general, as well as specifically my anti-social behaviour while preparing this document. I specifically thank my mother, for additionally providing life-sustaining nourishment in conveniently-portable packaging so that I may enjoy home-cooked meals while solving the problems of the Universe.

Thanks to Tom for refusing to play Showdown with me during the year, which forced me to do actual work. I may never have finished this project otherwise. Thanks to Dan for alleviating my self-esteem issues.

I would also like to thank my (few) friends, who tried as hard as they could to feign interest in astrophysics, as I babbled endlessly about the profound implications of the IMF and dark matter. So basically, thanks for not completely exiling me from the group for talking about science in night clubs.

To Frana, thank you for reading through this document more than once, and similarly pretending you care about astrophysics. Your advice throughout the year, such as "I don't even understand how code can have 'bugs'.", was thoroughly helpful through stressful times. Seriously though, without your proof-reading, this would likely be a mess of alternating tenses, blatantly omitted words and a disturbing lack of commas. You're alright.

I would like to thank Michele Cappellari, Shravan Shetty and the doctoral office at Oxford University for hosting me during the year. Your seemingly boundless knowledge inspires me to do better.

Thanks to the ExGal group for fruitful weekly discussions of all things astrophysics. You constantly provided new perspectives on how research was conducted, which helped developed my own research habits. Of course, it was also a much-welcomed relaxing environment after a long week's 'work'.

Finally, I thank my super supervisor, Richard McDermid. Given the page limit, though, I must stick to only the most important things. Firstly, for putting up with (way too many of) my impromptu hours-long office interruptions that would have driven anyone insane. Thanks for thinking more about my future than I have. Finally, of course, for the assistance in this project. Without your help, I'd probably still be stumbling over the example JAM model.

Abstract

The universality of the stellar Initial Mass Function (IMF) remains an open question to this day. Studies where individual stars can be counted provide strong evidence for universality in and around the Milky Way, while recent extragalactic studies find evidence for a dependence on galactic properties. In this work, we constrain the systematic variations of the IMF that have been observed in early-type galaxies, by constructing detailed dynamical models from kinematic observations. We account for the effects of spatially-varying stellar populations by computing star-formation histories from the observed spectra, and incorporating the resulting stellar mass-to-light ratio variations into the dynamical models. In addition, we determine total mass distributions, and separate the contributions from the stellar and dark matter components. This allows for inferences on the central dark matter fraction, as well as constraints on scaling relations of the total mass profile slope with galactic observables.

Contents

1 Introduction

1.1 Galaxy Formation & Evolution

Galaxy formation and evolution is a broad and critical aspect of astrophysics. It endeavours to describe the physical mechanisms and processes that determine how, and in what environments, galaxies form, as well as their resulting properties. To this end, much progress has been made since the field's inception in the early twentieth century. Credit for this inception is commonly attributed to Edwin Hubble's confirmation that some sources visible through telescopes were extragalactic - residing outside of our own Milky Way galaxy (Hubble, 1929). Since then, the field has solved a number of issues concerning the origin of these extragalactic sources by establishing the hierarchical model; provoking the introduction of dark matter (Rubin & Ford, 1970); and has challenged theories in cosmology through the formation of quasars and Active Galactic Nuclei (AGN) at extremely high-redshift, which must have formed in the very early Universe (for example, see Momjian et al., 2014).

The hierarchical model of galaxy formation - the current 'standard model' - dictates that haloes of cold dark matter (CDM) merge hierarchically, seeded by primordial fluctuations in the early Universe (White & Rees, 1978). This hierarchical merging is illustrated in Figure 1.1, created as part of the Millennium-II Simulation project (Boylan-Kolchin et al., 2009). Once large enough, these haloes

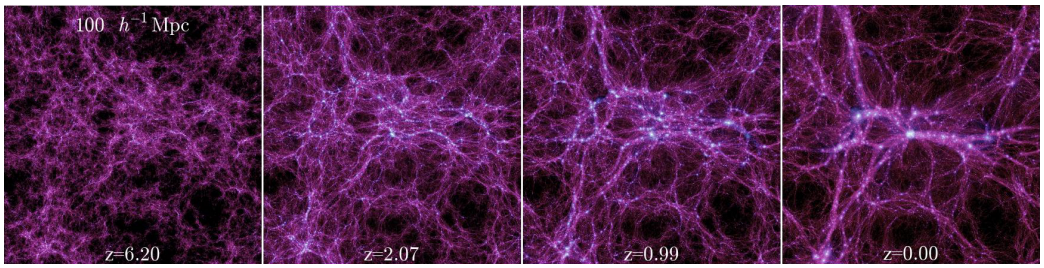

Figure 1.1: A simulation of the hierarchical merging of dark matter haloes. Created as part of the Millinneium-II Simulation project (Boylan-Kolchin et al., 2009), panels from left to right show the evolution of a region of dark matter through cosmic time, from $z = 6.20$ to $z = 0.00$ (present day). It can be seen that the dark matter has merged gradually through time to produce the large central halo and small satellite halos at $z = 0$.

provide gravitational over-densities for baryonic matter to coalesce within, which in turn form the galaxies we observe. The CDM paradigm has been very successful in explaining a diverse range of observations, including the accurate predictions of rotation curves of spiral galaxies (Begeman et al., 1991). In addition, CDM simulations accurately reproduce the large scale structure in the Universe (Springel et al., 2005). This structure is the observed grouping of galaxies and galaxy clusters into filamentary over-densities, separated by voids in which luminous matter is relatively scarce (for example, see Peacock et al., 2001).

Despite the progress made thus far, and the success of the hierarchical CDM paradigm, there remains a great rift in our understanding of how luminous galaxies come to form within these CDM halos. In particular, the formation of the various galaxy types that are observed in the present day evades a clear explanation. Galaxies are typically separated into two broad categories; early-type (spheroidals) and late-type (spirals), as was first illustrated by the Hubble 'Tuning Fork' shown in Figure 1.2 (Hubble, 1936). Early-type galaxies are, on average, more compact, redder, less morphologically complex (no spiral arms, weak bars), and more massive than late-type galaxies. However, if galaxies form by simple coalescence within a CDM halo, it is then unclear as to what physical processes determine the galaxy type, or the observed variation in the present-day galaxy population. The number and relative size of merger events since a galaxy's assembly - its 'merger history' - is believed to play a key role in the observed diversity in the present-day galaxy population. Due to the instability of a typical disk in a late-type galaxy, it is believed that major mergers usually result in massive early-type galaxies (Steinmetz & Navarro, 2002), since it would require very special geometric conditions to leave the disk unperturbed. However, there has been recent evidence indicating that the orientation of the merger is not the only concern. Through observations of the molecular gas content in merger remnants, Ueda

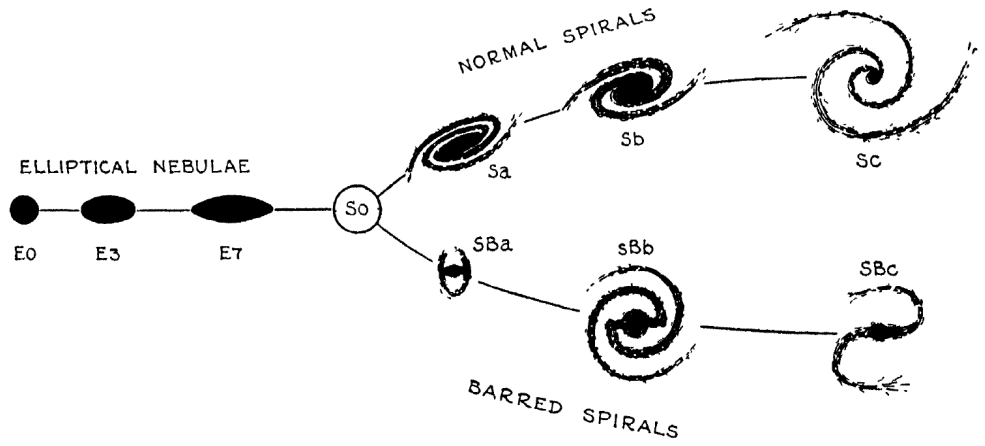

Figure 1.2: A depiction of the Hubble Tuning Fork. This shows the diversity of galaxy types observed in the present-day Universe. Early-type galaxies reside on the left, while late-type galaxies fill the right side of the diagram.

et al. (2014) find that 'wet' mergers - major mergers of gas-rich progenitors - can result in the formation of a gaseous disk. Martig & Bournaud (2010) find that the recycling of gas due to typical stellar mass-loss mechanisms can induce growth in the disk. This is due mainly to star formation in the gas that has remained in the 'disk' component following the galaxy's earlier mergers (with the assistance of cold gas accretion onto the disk). They find that this makes the disk less vulnerable to disruption by subsequent merging, and they claim that this explains how we can observe disk galaxies in the present day, despite those galaxies having gone through mergers. Steinmetz & Navarro (2002) have also found that galaxies can re-form their disks post-merging by smooth gas accretion. Finally, simulations of spiral-galaxy formation have shown that many different progenitor morphologies can lead to a spiral galaxy, and that disk-dominated systems are typically accompanied by steady gas accretion (Martig et al., 2012), supporting the findings of Steinmetz & Navarro (2002). These results indicate that the merger history is not the only impacting factor, and that the mechanism that determines galaxy type is a complex combination of various physical process, including gas kinematics and interactions, stellar feedback processes, and of course gravitational interaction. Such processes are not not directly addressed in the pure-CDM paradigm, and thus these aspects of galaxy formation remain unresolved.

1.2 Stellar Initial Mass Function

In an attempt to address many of these issues, attention has turned in recent times to the stellar Initial Mass Function (IMF). The IMF is an empirically-derived probability distribution function which describes the distribution of stellar masses in a single star formation event. It is an important tool in many areas of research in both theoretical and observational astrophysics. For instance, de Souza

et al. (2014) model the expected rates of the supernova explosions of Population III stars (the first generation of stars that formed from pure unenriched gas) in the early Universe. Since these stars have never been detected directly, the authors argue that detection via their supernovae is the best strategy with current technology. Their rate calculations are explicitly dependent on the assumed IMF, since this will determine the number of stars of sufficient mass to cause a detectable supernova. They also show that the rates of particular classes of supernovae can vary by up to a factor of 10 for different IMF assumptions. Agertz et al. (2011) simulate the formation of disc galaxies, which includes treatment of supernovae and stellar feedback processes. Their calculations of both stellar mass-loss and supernova mass ejection similarly depend explicitly on the assumed IMF. Wilkins et al. (2008) characterise the star formation rates of galaxies through cosmic time. The IMF in this context is necessary for deducing stellar masses from the observations, which are then used to produce the star formation rates. As can be seen, the IMF is important for an abundance of research areas, from stellar physics, to galaxy formation and galaxy evolution.

The IMF is typically assumed to be a power law, and is expressed as

$$\begin{aligned} \xi\left(M\right) &\equiv \frac{\mathrm{d}n}{\mathrm{d}M} \\ &= kM^{-\alpha} \end{aligned} \tag{1.1}$$

where α is the normalisation, M is the stellar mass, n is the stellar count per differential mass range $M + \mathrm{d}M$, and k is the proportionality constant.

Alternatively, the IMF can be expressed as a function of logarithmic mass;

$$\begin{aligned} \xi\left(\log_{10}\left(M\right)\right) &\equiv \frac{\mathrm{d}N}{\mathrm{d}\log_{10}\left(M\right)} \\ &= kM^{-\Gamma} \end{aligned} \tag{1.2}$$

where N is now the stellar count per differential *logarithmic* mass range $\log_{10}\left(M\right) + \mathrm{d}\log_{10}\left(M\right)$.

The parameters of Eqs. 1.1 and 1.2, denoted here as α and Γ, respectively, are related by

$$\alpha = \Gamma + 1$$

The IMF was initially defined in the form of Eq. 1.2 by Salpeter (1955), who observationally derived values for Γ and k of 1.35 and 0.03, respectively. His study concluded that a single power law characterised by these values was a good approximation to the real mass function within the range of

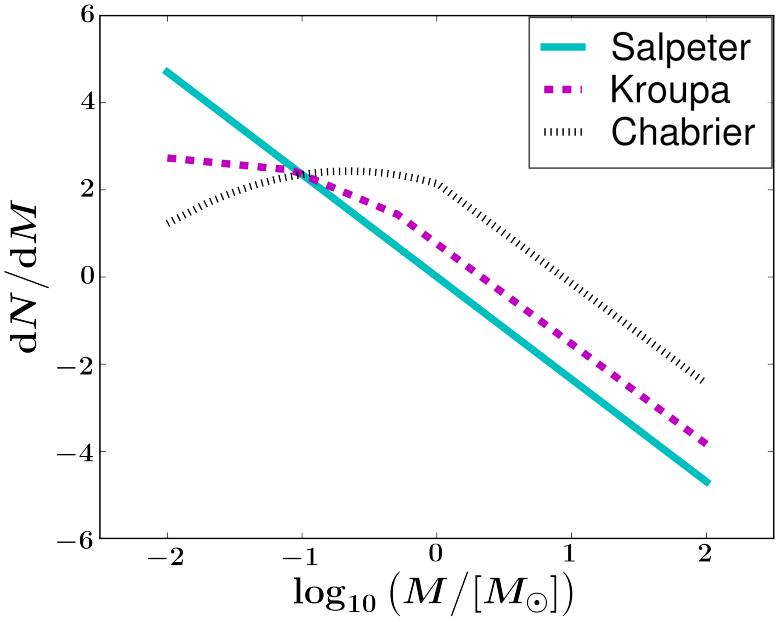

Figure 1.3: The published IMFs of Salpeter, Kroupa, and Chabrier, normalised to give the same stellar number density at 0.1 $M_\odot$.

stellar masses $-0.4 \lesssim \log_{10}(M/M_\odot) \lesssim 1$ (Salpeter, 1955). Subsequent studies introduced ranges of masses with different exponents. For instance, the Kroupa (2001) IMF is defined piece-wise;

$$\Gamma(M) = \begin{cases} -0.7 & 0.01 < M/M_\odot < 0.08 \\ 0.3 & 0.08 < M/M_\odot < 0.5 \\ 1.3 & M/M_\odot > 0.5 \end{cases} \tag{1.3}$$

The Chabrier (2003) IMF, given in Eq. 1.4, is also defined piece-wise, however the different mass bins are described by entirely different functional forms.

$$\xi(\log_{10}(M)) = \begin{cases} \frac{0.086}{\log_{10}(M)} \exp\left[-\frac{(\log_{10}(M)-\log_{10}(0.22))^2}{2\times 0.57^2}\right] & M/M_\odot < 1 \\ kM^{-1.3} & M/M_\odot > 1 \end{cases} \tag{1.4}$$

The log-normal component of this definition (for $M/M_\odot < 1$) is also similar to that originally proposed by Miller & Scalo (1979). An illustration of some of the published IMF forms is given in Figure 1.3.

The IMF is of vital importance for the calculation of galaxy mass using the observed light, which is itself of critical importance for understanding not just their formation, but galaxies in general. To understand why the IMF is difficult to determine in galaxies, it is important to consider exactly what is detected when observing an integrated stellar population - that is, when individual stars cannot be resolved. Figure 1.4 (taken from Conroy & van Dokkum, 2012) illustrates the cumulative contribution

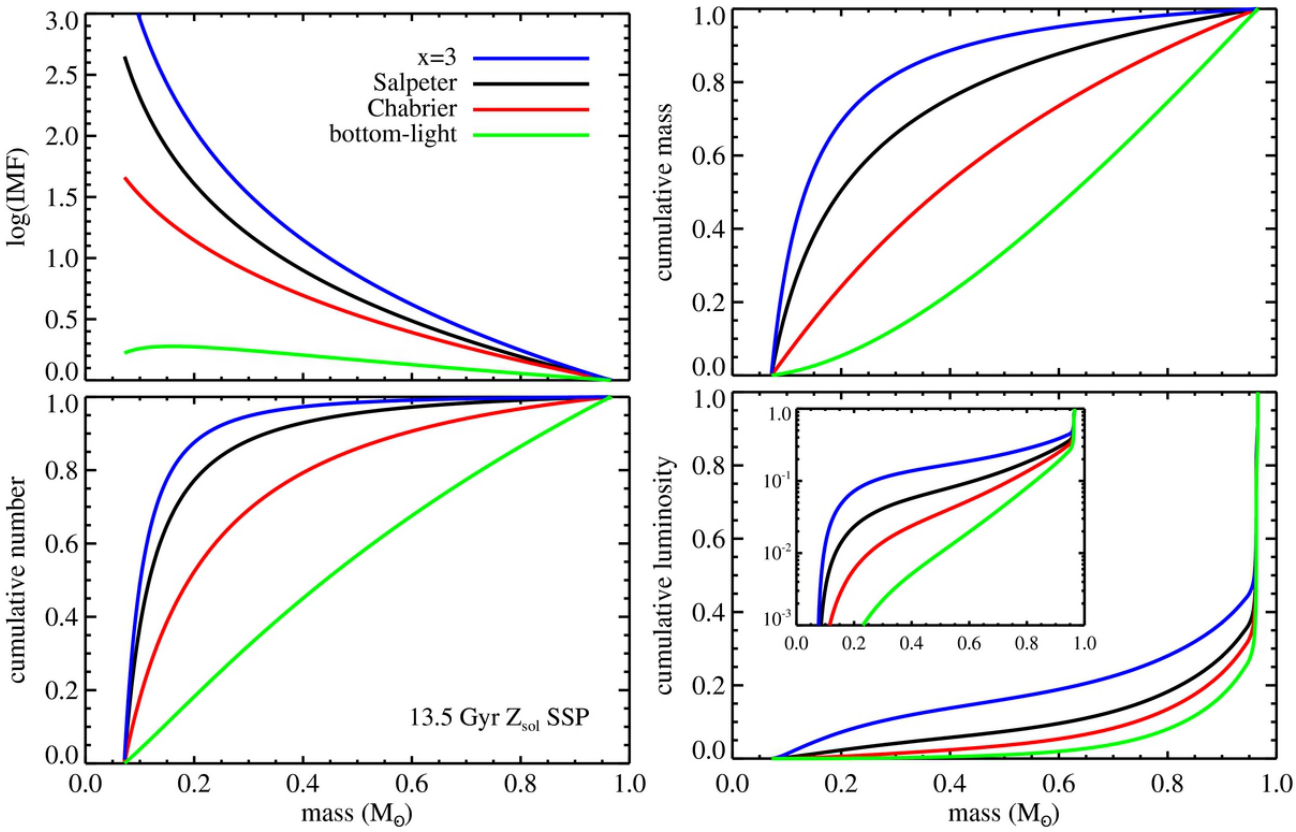

Figure 1.4: The cumulative contribution as a function of stellar mass to the number of stars (bottom left), mass in stars (top right), and bolometric luminosity (bottom right; with a log-linear version inset), as found by Conroy & van Dokkum (2012). Four different IMFs were modelled (top left), using a 13.5 Gyr population with solar metallicity. The low-mass end dominates in both mass and number, but contributes very little to the luminosity.

to the mass and luminosity of an integrated stellar population as a function of stellar mass, as modelled by a 13.5 Gyr solar-metallicity population. It shows that in old populations, which is typically the case in massive early-type galaxies, low-mass stars are the most numerous, and dominate the stellar mass of the galaxy. However, they only contribute a small amount to the luminosity, which is instead dominated by the high-mass population. Thus, the observation is itself dominated by the higher-mass population, since it relies on the luminosity. In order to calculate the stellar mass of the galaxy, it is necessary to infer the number of low-mass stars from measurements dominated by the higher-mass population. Measuring stellar mass from such observations therefore depends heavily on the assumed nature of the IMF. Thus, it is crucial to constrain the IMF forms given above, to ultimately explain how stars form in such galaxies.

1.2.1 Observational Constraints on the IMF

For direct measures of the IMF - that is, literally counting stars in resolved systems such as globular clusters in the Milky Way - binarity in stellar systems can skew the measured mass distribution (Bastian et al., 2010). This arises simply because binaries are typically unresolved, and so appear as a single star. Studies of the IMF, then, would include these systems as single stars with relatively high mass, rather than counting the two lower-mass stars that the system is actually composed of. The result of this is that extra weight is unduly given to the high-mass end of the IMF. To resolve this issue, attempts have been made to correct IMF studies for the binary fraction. However, both the intrinsic binary fraction and the detectability of the companion are seen to depend on stellar type (for example, see Bastian et al., 2010; Lada, 2006, respectively). Thus, attempts to correct for the binary fraction are complicated by this type-dependence.

Ideal observational targets for resolved IMF studies are those that have remained unchanged since their formation (that is, have undergone no significant star formation), allowing for a direct measure of the distribution of stellar masses. This is indeed the motivation for selecting globular clusters. However, observations indicate that globular clusters can lose stars following dynamical interactions (Schilbach & Röser, 2008). This means that measuring the present-day mass distribution would provide an inaccurate measure of the IMF, even in systems that are passive (non-star-forming), and genuinely contain only one stellar population. This poses a difficult problem for this type of study, as there is typically very little evidence that such clusters have lost stars, or what the masses of those stars were.

The slope of the IMF depends in part on the number density of low-mass stars. However, these stars radiate significantly less light compared to their higher-mass counterparts. This makes the IMF particularly difficult to constrain via direct methods. Low-mass ($M/M_{\odot} < 0.3$) stars have strong NaI and Wing-Ford FeH emission lines, while these are weak or absent in higher-mass stars of the same temperature (van Dokkum & Conroy, 2010), and so spectral information can be used to place very strong constraints the presence of low-mass stars. However, the low-mass stars must be sufficiently abundant in order to be detected in the spectra.

Stellar remnants such as black holes and neutron stars further complicate the issue. These types of remnants originate from massive stars, and so their number density contributes to the high-mass region of the IMF. However, they radiate very little light, if any at all. Thus, a significant portion of the high-mass population is unseen by observation because they have evolved into remnants, impacting the measured number density of high-mass stars, and consequently the inferred IMF.

By definition, the IMF traces a single star formation event. However, by the epoch of observation (the present day), there has been sufficient time for galaxies to have completed multiple star formation events. This produces complex star formation histories that make inferences of the IMF much more difficult, since it then becomes necessary to separate populations into distinct formation events in order to determine the contributions to the IMF, as opposed to the present-day mass function.

It is non-trivial to disentangle many of the complex evolutionary features in a population, such as multiple star bursts, stellar ageing, and feedback processes. Thus it is clear that constraints on the IMF via observations are difficult to obtain in practise, whatever method of investigation is adopted.

1.2.2 Universality

The most contentious aspect of the IMF is whether it is universal across space and time, or depends in some way on galaxy parameters. A universal IMF has been the adopted norm since the IMF's inception, though the evidence for non-universality is rapidly amassing. As discussed above, however, any evidence for IMF variations or otherwise is particularly difficult to interpret, and is often riddled with subtleties. Furthermore, since the direct (resolved systems) and indirect (integrated light) measurements of the IMF are such distinct methodologies, comparison between the two is not straight-forward. Evidence for variation has come solely from indirect methods, and so there has yet to be a consistent comparison. Nevertheless, evidence both for and against is presented below to set the foundations on which this project is built.

Studies of the Milky Way have provided strong evidence for a universal IMF (Kroupa, 2001, 2002). Typical direct IMF methods study star clusters in the Milky Way. Star clusters are believed to form in a single star-burst, and are hence appropriate for such IMF studies. However, only those clusters within the Milky Way are fully resolvable, so these conclusions can not be compared to other environments. Wyse (1997) studied environments outside the Milky Way by analysing heavy-element yields of Type Ia and Type II supernovae, and their effect on the intracluster medium (ICM) of galaxy clusters. Of course, the enrichment of the ICM depends on the number of massive stars that exploded as supernovae and produced heavy elements. They modelled various IMF assumptions and found that, in order to match observed abundances, a universal Salpeter IMF was favoured. More recently, work has been done studying the impact of observed low-mass X-ray binaries on the IMF (Peacock et al., 2014). They find that the number densities of these objects are roughly constant across nearby early-type galaxies of various masses. This implies that the number densities of high-mass progenitors to these binaries,

and subsequently the IMF, are also constant. However, as discussed above, the binary fraction is difficult to handle, and the authors state that numbers of such binaries are poorly constrained (Peacock et al., 2014). Further evidence for a universal IMF is based on, as mentioned above, the evolution of globular clusters after their formation. Shanahan & Gieles (2015) model the expected effect on the mass functions, taking into account this type of dynamical and stellar evolution. They find that after a significant time, systems can evolve to have different observed mass distributions, even though they were drawn from the same initial distribution, due to such things as differences in initial metallicities. The observed M/L, for instance, has been observed to depend on metallicity (for example, see Strader et al., 2009). Thus, if a comparison was made between two systems with different initial metallicities using an IMF inference technique that relied on the observed M/L, a non-universal IMF would be deduced, even if the two systems were in fact drawn from the same mass distribution. This argument, however, can not rule out IMF variation; the authors only propose an alternate explanation for the observations.

The evidence in favour of a varying IMF has accumulated significantly in recent years. Eisenhauer (2001) have observed evolution of the IMF, based on analysis of the earliest star-burst galaxies in the Universe. They claim that if the earliest galaxies were governed by the present-day Milky Way-like IMF, there would have been too few high-mass stars to account for the enrichment of the gas content in galaxy clusters observed in the present day. Thus, they conclude, the IMF in the early Universe must have favoured more high-mass stars compared to the present-day IMF. Further evidence for the evolution of the IMF has been found by van Dokkum (2008). They studied the effect of the IMF on the evolution of the mass-to-light ratio (M/L). By observing early-type galaxies in a number of galaxy clusters at redshifts $0.02 \leq z \leq 0.83$, and characterising the evolution of the M/L, they find that an IMF slope which is significantly flatter than that of a Salpeter ($\Gamma < 1.35$) is favoured at high redshift (the high end of their redshift range). Conversely, the present-day Milky Way IMF is well-described by a slope of $\Gamma \sim 1.35$, and so this indicates an evolution of the slope of the IMF from early epochs to the present day. Further evidence suggesting a time-dependent IMF has come from the analysis of low-mass x-ray binary fractions (Weidner et al., 2013). Studying the NaI and Wing-Ford FeH spectral features (which are particularly prevalent in very low-mass stars), van Dokkum & Conroy (2012) have found evidence for IMF variation. Their study concluded that more massive early-type galaxies are better described by more bottom-heavy IMFs, indicating a dependence of the IMF slope on galaxy mass. Recently, Martín-Navarro et al. (2015) have found, from a sample of 24 ETGs, that the IMF depends on metallicity, which itself varies between galaxies. They also posit that this metallicity dependence is in fact the driver behind the observed IMF variation.

1.2.3 Systematic Variation

Recently, Cappellari et al. (2012) have found strong trends of the IMF with galaxy mass. Their work uses dynamical and spectral information, which are both integrated-light methods. Integrated-light methods are used when the observed systems are unresolved, and so the observations are integrated along the line-of-sight, meaning there is information only in two of the three spatial dimensions. The aim of their work was to derive the 'mis-match' between the mass inferred from observation, and the mass inferred by assuming a Salpeter IMF. They show that this mismatch increases with galaxy mass. The authors define $\alpha_{\rm dyn.} \equiv (M/L)_{\rm stars} \,/\, (M/L)_{\rm Salp}$ to compute this mismatch. $(M/L)_{\rm stars}$ is computed from dynamical models. It is therefore affected by both the luminous and dark matter content of the galaxy, which both contribute to the gravitational potential and hence the kinematics. $(M/L)_{\rm Salp}$, on the other hand, is the M/L one would calculate by applying a Salpeter IMF to the observed light directly. It is therefore affected only by the luminous component. With this definition, a value of $\alpha_{\rm dyn.} = 1$ implies that the measured IMF is exactly a Salpeter. Given that it is defined using the power-law (defined per unit mass) form of the IMF from Eq. 1.1, this implies that the value of the measured IMF slope is $\alpha = -2.35$. Any deviation from $\alpha_{\rm dyn.} = 1$ could be attributed to either dark matter, shifting $(M/L)_{\rm stars}$ due to its contribution to the gravitational potential; to the Salpeter IMF, which may not accurately represent the galaxy; or to a combination of these two effects. To disentangle variations caused by dark matter from those caused by a variable IMF, various models were tested by Cappellari et al. (2012) (defined in detail in Cappellari et al. (2013a)) which make different assumptions about the dark matter halo. The key result of their work, given in Figure 1.5, is that *the variations persist for all treatments of dark matter*. Thus, while *some* of the differences between dynamically-derived and spectroscopically-derived masses could be caused by dark matter, it alone is insufficient to explain the observations, and so IMF variation must be invoked.

The data used for this analysis is from the ATLAS^{3D} survey (Cappellari et al., 2011). ATLAS^{3D} collected integral-field data of 260 local ($D < 42$ Mpc) early-type galaxies using the SAURON (Bacon et al., 2001) integral-field unit (IFU). The data provided by IFUs, so-called 'data-cubes', prove to be excellent for unresolved IMF investigations. The three dimensions of the data cube include two spatial axes, and a spectrum at every coordinate, which provide the spatially-resolved kinematics and stellar population properties necessary for this type of study.

The modelling conducted to reach this result was based on a few key assumptions. Firstly, the galaxies in the sample were assumed to be intrinsically axisymmetric oblate spheroids. The ATLAS^{3D} sample was selected based specifically on morphological type, and so this assumption is reasonable. Secondly,

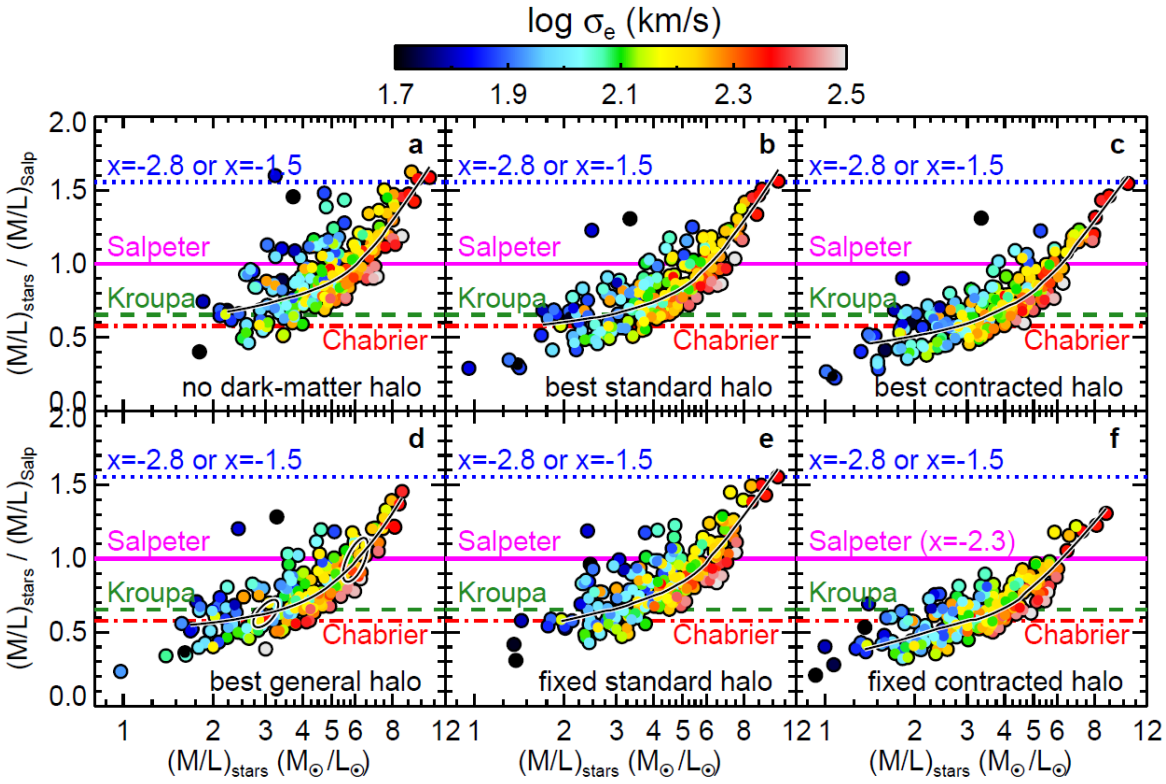

Figure 1.5: The systematic IMF trends found by Cappellari et al. (2012), for various models of the dark matter halo (indicated in the bottom-right of each panel). The horizontal lines show where a galaxy would lie if its IMF were of the indicated form, where x is the slope of the (linear) IMF. The points are coloured by the effective velocity dispersion, σ_e. The black line is the spatially-averaged LOESS (Cleveland, 1979) curve. Crucially, trends exist in all models.

the galaxies were assumed to have no spatial gradients in $(M/L)_{\rm Salp}$. As mentioned above, multiple stellar populations can complicate inferences of the IMF. Thus, to avoid this issue, a subset of the ATLAS$^{\rm 3D}$ sample was used for the results of Cappellari et al. (2012). The selection criterion for this subset was that the observed Hβ absorption had sufficiently small spatial variation, which is interpreted as small spatial variation in age. This is important for IMF deductions, and a consequence of this is that the variation in $(M/L)_{\rm Salp}$ should be equally small.

1.3 Mass-Density Profiles

Owing to the nature of the spatially-resolved kinematics measured by IFUs, it is possible to accurately model the mass-density profiles of observed galaxies. These profiles can assist in placing constraints on the IMF by providing accurate constraints on the dark matter content. Furthermore, computing mass models of the observations in this way helps to constrain simulations of galaxy formation, which must then produce galaxies with similar profiles. A typical mass-density profile is given in Figure 1.6.

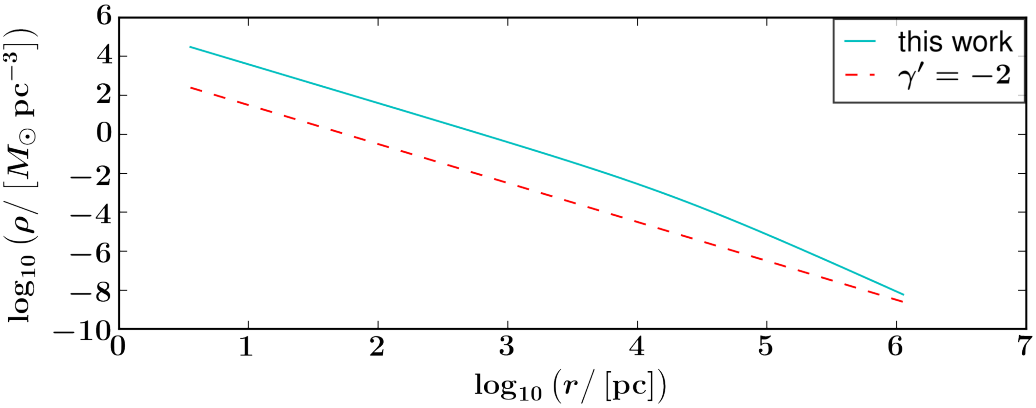

Figure 1.6: The total mass-density profile of NGC2685, computed by constructing a mass model from an IFU observation, assuming a spherical total mass distribution.

It is modelled from an IFU observation, assuming a spherical total (stellar and dark matter) mass distribution. The shape of this profile provides a lot of information regarding the contributions of baryonic and non-baryonic matter as a function of radius.

1.3.1 Core-Cusp Problem

Recent cosmological simulations have predicted that mass-density profiles characterising the density of pure-CDM halos should exhibit a 'cusp' in the central region - that is, a peak in density (for example, see Ishiyama et al., 2013; Navarro et al., 2004). Conversely, mass-density profiles inferred from observations indicate that these profiles should exhibit a 'core' towards this region - that is, a notable plateau (for example, see Kuzio de Naray et al., 2008; Oh et al., 2008, 2011). This discrepancy, the so-called 'core-cusp' problem, remains unresolved, and thus studying such mass-density profiles can provide insight into the physics of both dark and luminous matter in the context of galaxy formation.

1.3.2 Bulge-Halo Conspiracy

From gravitational lensing studies (Bolton et al., 2006), it has recently emerged that the total mass-density profiles have a very narrow distribution of slopes. This is the so-called "Bulge-Halo Conspiracy" Auger et al. (2010); Koopmans et al. (2009). The 'conspiracy' is that the luminous and dark matter components of these galaxies appear to conspire in such a way as to consistently produce total mass-density profiles with similar slope (resulting in the narrow distribution), apparently irrespective of the individual luminous and dark matter profiles. The bulge-halo conspiracy was discovered from the Sloan Lens Advanced Camera for Surveys (SLACS) project (Bolton et al., 2006). This work found that the average slope of the total mass-density profile (within 1 R_e) for a sample of early-type galaxies was

$\langle\gamma'\rangle = -2.078 \pm 0.027$, with a remarkably low intrinsic scatter of $\Delta_{\gamma'} = 0.16 \pm 0.02$ (Auger et al., 2010).

For this result, the SLACS Survey observed 131 systems, of which 73 were confirmed to be strong lenses (Auger et al., 2010). The lensing provides precise measurements of total enclosed mass (along the line-of-sight), and so models of the total mass distribution were made using this data. For this work, the distribution of orbital velocities within these systems was assumed to be completely uniform. From these models, as well as Sloan Digital Sky Survey (SDSS) and Hubble Space Telescope (HST) photometry, mass-density profiles were computed and analysed in order to draw conclusions about the distribution of total mass-density profile slopes for their sample.

Further evidence in favour of a 'bulge-halo conspiracy' has recently come from a study out to larger radii ($\sim 4\ R_e$) on a sample of 14 early-type galaxies, combining data from integral-field and long-slit spectroscopy (Cappellari et al., 2015). By producing dynamical models of these data, which similarly trace the total enclosed mass, they find comparable results, reporting $\langle\gamma'\rangle = 2.19 \pm 0.03$ with an intrinsic scatter of $\Delta_{\gamma'} = 0.11$.

However, there have not been many studies investigating the idea of the bulge-halo conspiracy, and sample sizes are typically small. Yet, if it is corroborated by subsequent studies, a consistent total-mass density profile slope across a broad range of galaxy masses, and possibly galaxy types, alludes to a fundamental and universal property of galaxy formation that requires further investigation.

1.4 This Project

The main aim of this work is to relax the assumption of spatially-constant $(M/L)_{\rm Salp}$ from the modelling conducted in § 1.2.3. The consequences of this are many-fold. Most obviously, it reduces the number of assumptions in the modelling, producing more realistic results across the sample. Furthermore, it may allow the sample size to be increased, by making it possible to include those galaxies within the ATLAS^{3D} sample which were initially excluded based on their Hβ absorption gradient. This is because negligible age variation is no longer a requirement of the modelling, since it is taken into account by the $(M/L)_{\rm Salp}$ gradient. This in turn produces more robust statistics, and hence more reliable results. Finally, it similarly makes it possible to apply these techniques to more general galaxy surveys, such as SAMI (Croom et al., 2012) and MaNGA (Bundy et al., 2015), which contain all types of galaxies - late-type and star-forming, for instance.

In addition to improving the robustness of the modelling and exploring the implications of a non-universal IMF, the total mass profiles can also be determined as a direct by-product of this work. In addition to including the effects of spatially-varying stellar populations for the first time, this work will determine the total, stellar, and dark matter mass profiles for an unprecedented number of galaxies, observed and modelled in an accurate and homogeneous manner. This will provide strong constraints on the validity of the bulge-halo conspiracy, and allow us to look for any additional dependency on other galaxy parameters.

2

Common Methods

2.1 Models

2.1.1 Multi-Gaussian Expansions

The multi-Gaussian Expansion (MGE) formalism (Cappellari, 2002; Emsellem et al., 1994; Monnet et al., 1992) is utilised for all methods in this work. The MGE process fits a series of Gaussians to the observed isophotes of each galaxy. As a result, the parameters of the MGE are all projected quantities, since the observations are themselves projected. This formalism provides an analytic description of the light, in a form that is computationally straight-forward to manipulate. The MGEs used for this work are those published by Scott et al. (2013). They are computed from SDSS r-band photometry, and so all calculations that require the MGEs implicitly produce r-band parameters.

Each Gaussian in an MGE is characterised by three *projected* parameters - the total counts T_j, dispersion σ_j, and axis ratio q'_j. An example fit using the MGE formalism is given in Figure 2.1 (Cappellari, 2002). Figure 2.2 (Scott et al., 2013) shows the Gaussians overlaid on the observed isophotes, and Table 2.1 lists all of the parameters of this MGE. The axis ratio is dimensionless, and the dispersion is measured in arcseconds. The units of the total counts depend on what the MGE is describing, however

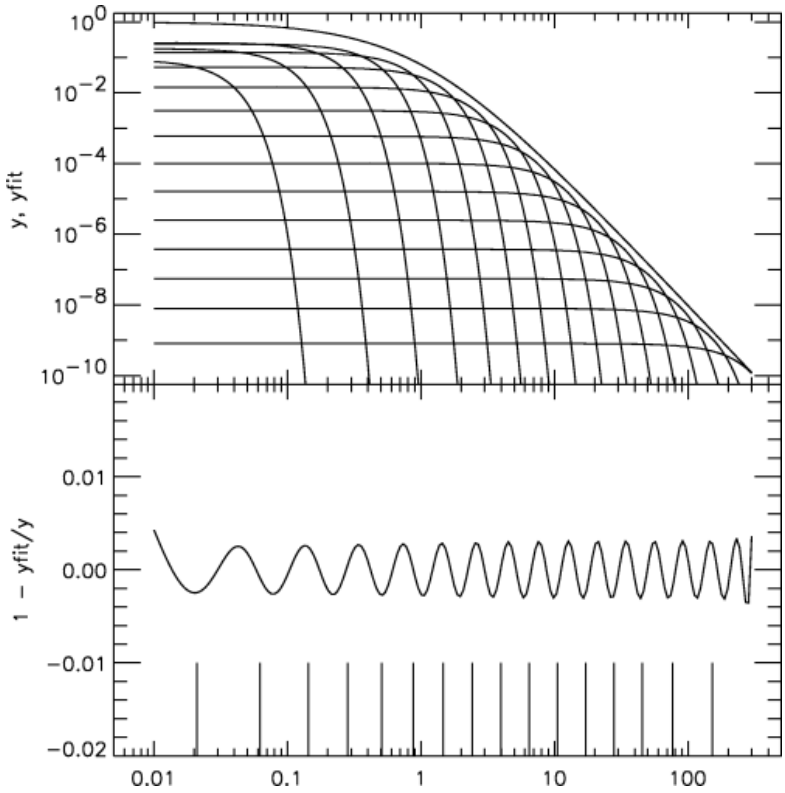

Figure 2.1: A typical 1D MGE fit to a density profile from Cappellari (2002). The top panel shows the profile, and the series of Gaussians that compose the MGE. The bottom panel shows the absolute error (curve), and the position of σ_j for each of the Gaussians in the top panel (vertical lines).

Total Counts T [$L_\odot$ pc^{-2}]	Dispersion σ [$''$]	Axis Ratio q'
25616.793	0.31847133	0.446332
6343.7342	1.5463585	0.300000
2219.7921	1.5730268	0.592663
2168.1794	3.5394999	0.444292
428.49081	5.6308019	0.750000
616.28130	9.3102148	0.300000
75.582357	19.944932	0.750000
325.23933	21.505537	0.300000
37.826520	46.483032	0.730271

Table 2.1: The MGE parameters of NGC2685 from Scott et al. (2013).

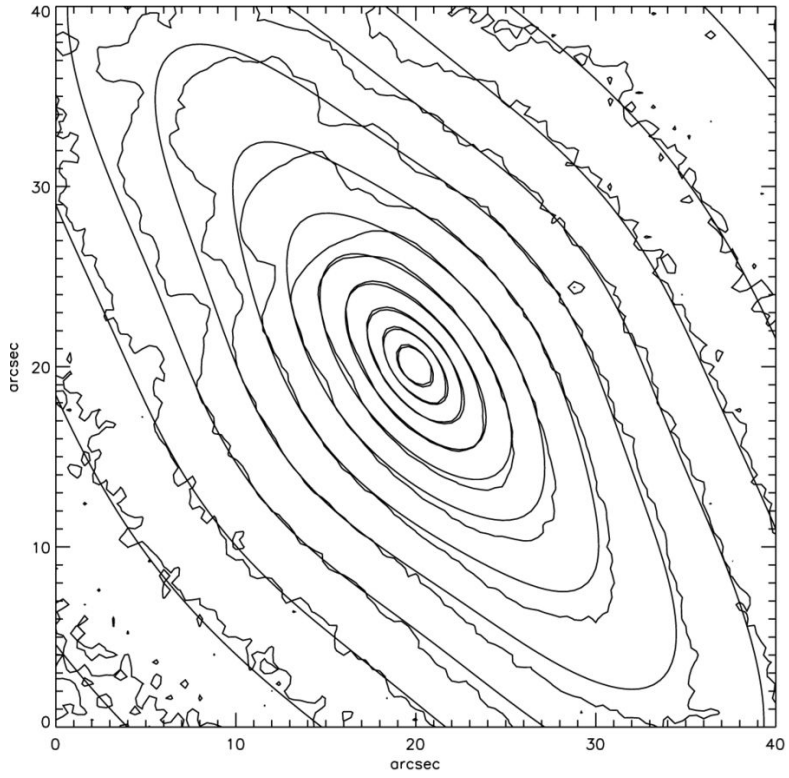

Figure 2.2: The observed isophotes and MGE of NGC2685 from Scott et al. (2013). The effects of dust are clearly visible in the isophotes. The Gaussians from Table 2.1 are interpolated and the reconstructed contours are plotted in increments of 1 mag arcsec^{-2}.

it is always a projected quantity. The MGEs from Scott et al. (2013) describe the intrinsic luminosity, and so they are in units of surface brightness, [$L_\odot$ pc^{-2}]. It is often the case that MGEs are used to describe the intrinsic mass (see § 2.1.2), and in this case the MGEs are in units of mass surface density, [$M_\odot$ pc^{-2}].

2.1.2 Jeans Anisotropic MGE Modelling

The Jeans Anisotropic MGE (JAM) technique (Cappellari, 2008) is used to model the kinematics of each galaxy. Specifically, JAM attempts to predict the moments of the velocity distribution at every location in the spatially-resolved IFU data, using the Jeans equations. To do this, the Jeans equations are integrated and simplified to described the velocity moments of a galaxy, given a parametrisation of both the stellar and total density. The reader is pointed to Cappellari (2008) for the mathematical derivation of the JAM formalism that is used in this work. The simplifying assumptions adopted for the JAM models used in this work are: (i) the orientation of the velocity ellipsoid is aligned with the cylindrical coordinate system (R, z, ϕ) (ii) the galaxies are axisymmetric, eliminating an entire Jeans equation (in the v_ϕ direction) (iii) the anisotropy of the velocity ellipsoid, which quantifies the departure

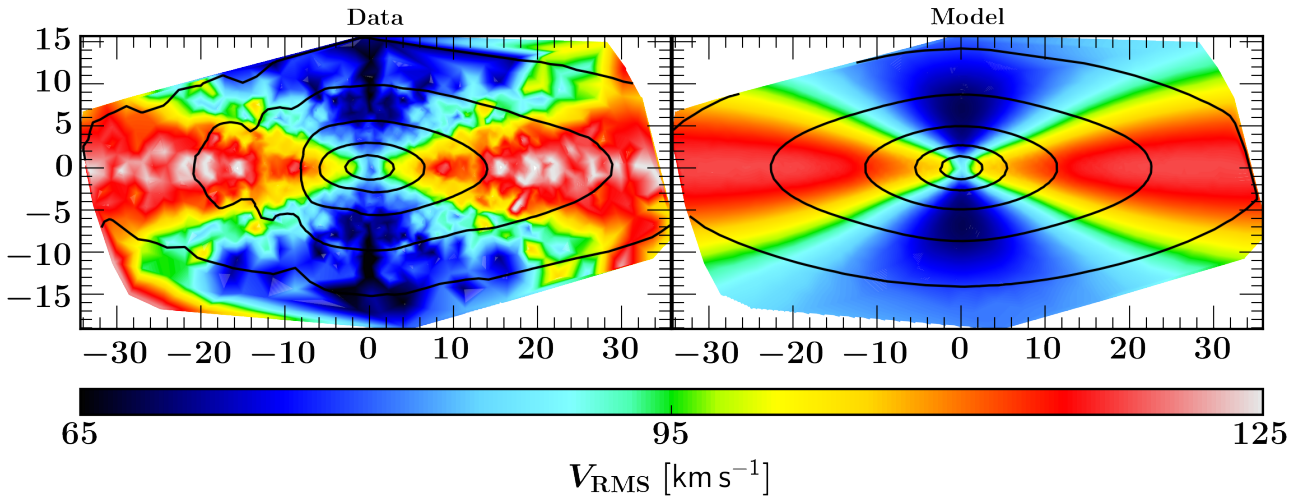

Figure 2.3: The best-fit JAM model for the RMS velocity field of NGC2685. The left panel is the RMS velocity computed directly from the ATLAS^{3D} data cube, according to $V_{\rm RMS} = \sqrt{V^2 + \sigma^2}$, where V is the mean stellar velocity and σ is the stellar velocity dispersion, as in Cappellari et al. (2013a). The isophotes from the observations are overlaid. The right panel is the best-fitting JAM model. The MGE is used to compute analytic isophotes, which are overlaid here in increments of 1 magnitude.

from an isotropic orbital distribution, is constant, and defined as

$$\beta_z \equiv 1 - \frac{\sigma_z}{\sigma_R} \tag{2.1}$$

for the vertical and tangential velocity dispersion, σ_z and σ_R, respectively. The parametrisation used for both the stellar and total density in the model computed here is the MGE formalism. The JAM model requires two sets of MGEs - one describing the light distribution of the kinematic tracer (in [$L_\odot$ pc^{-2}]), and one describing the gravitational potential (in [$M_\odot$ pc^{-2}]), where the gravitational potential MGE is computed by assuming an intrinsic mass density profile and projecting onto the observation. These two MGE models are completely independent, however, and are free to have different shapes and numbers of Gaussians. Of all the velocity moments predicted by JAM, we focus here on the Root Mean Squared (RMS) velocity, which is defined as $V_{\rm RMS} = \sqrt{V^2 + \sigma^2}$, for mean stellar velocity V and stellar velocity dispersion σ. The result of a typical JAM model is presented in Figure 2.3.

2.1.3 Stellar Templates

Single Stellar Population (SSP) templates are used to compute the $(M/L)_{\rm Salp}$ profiles, thereby relaxing the assumption of constant $(M/L)_{\rm Salp}$. The specific templates used here are those from the MIUSCAT library (Vazdekis et al., 2012). This library includes templates with broad ranges of age (0.063 – 17.78 Gyr) and metallicity (metal fraction Z range is 0.0004 – 0.03). The templates that comprise the library are model spectra, assigned an age and metallicity. Each spectrum is designed to

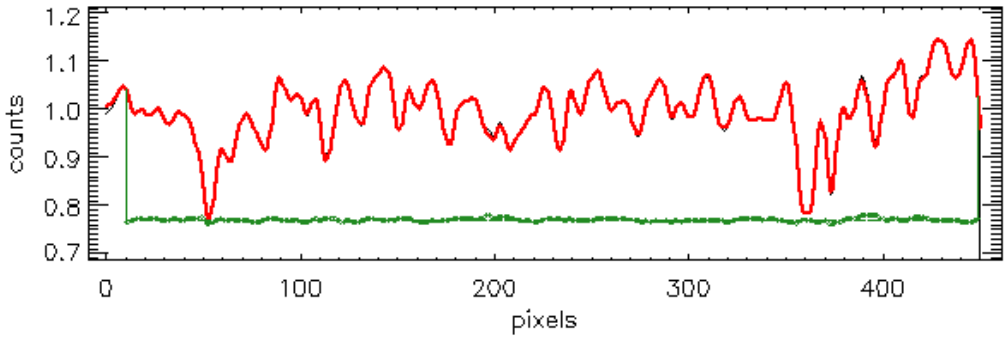

Figure 2.4: The spectrum (black) from one spaxel of the SAURON detector, and the best-fit linear combination of templates (red) from PPXF for NGC2685. The green points are the residuals of the fit.

mimic the integrated light of a mass-complete population of stars with the particular age and metallicity of the template. The library covers a wavelength range of 3465 – 9469 Å, which comfortably includes the SAURON spectral range of 4810 – 5400 Å. The extraction of the $(M/L)_{\rm Salp}$ maps is done as per McDermid et al. (2015), which is conducted as follows. Each template in the library includes tabulated data of both the mass and luminosity contained in stars and stellar remnants for its specific age and metallicity. For this work, the relative contributions of the stars and remnants are dictated by a Salpeter IMF. The first step of computing the $(M/L)_{\rm Salp}$ profile is to fit the MIUSCAT templates to the spectra from the IFU. The fits are made using the penalised pixel-fitting (pPXF) procedure of Cappellari & Emsellem (2004). This procedure attempts to parametrically recover the line-of-sight velocity distributions for each galaxy, by fitting template SSPs to the observed spectra adopting a penalised likelihood. The best-fitting model spectrum is used to determine the velocity moments, while the specific combination of template SSPs that the model spectrum was composed of provides information on the relative amounts of ages and metallicities present in the population. An example of this fit is presented in Figure 2.4.

The weights of the fit from pPXF, which are the coefficients of the linear combination of templates, dictate the relative contributions of each template to the model spectrum, in effect describing the proportion of stars in the galaxy with that age and metallicity. By scaling the tabulated mass of a particular template by its corresponding weight from the fit, the total mass contained in stars and remnants of that age and metallicity is determined. This is repeated for all templates with non-zero weights. A map of weights for the full parameter space of the MIUSCAT library is given in Figure 2.5. In addition to computing the total mass from these templates, we compute the total luminosity by scaling the tabulated luminosity of each template by its corresponding weight. The ratio of the total mass to the total luminosity is the $(M/L)_{\rm Salp}$ for that particular data bin. In this way, the two-dimensional spatial

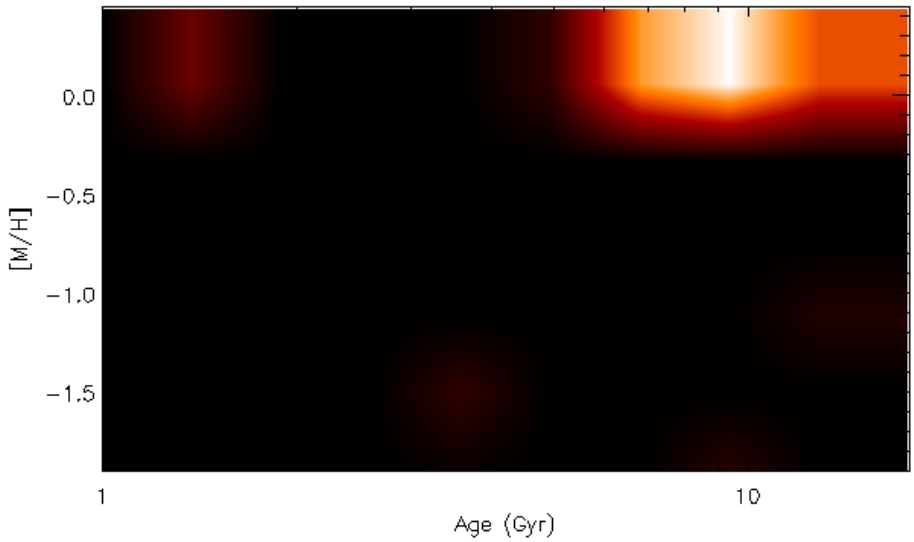

Figure 2.5: The weights from the fits of the ATLAS^{3D} spectra for NGC2685 to the MIUSCAT template library. The plot shows the entire range of the MIUSCAT library, in both age and metallicity. A bright region indicates that templates from the library with that corresponding age and metallicity have high weighting from the fit. This implies that there is a high fraction of the population with this age and metallicity. Dark regions indicate low or zero weighting for the corresponding templates. According to this figure, then, the majority of stars in NGC2685 formed $\sim$ 10 Gyr ago, with approximately solar metallicity.

distribution of $(M/L)_{\rm Salp}$ is built up by computing this fit in every bin. The data is binned such that the signal-to-noise (S/N) in every bin exceeds a value of 100. As a result, a bin in the outer regions would likely include more spaxels of the IFU detector than a bin in the central region. Figure 2.6 is a typical $(M/L)_{\rm Salp}$ map created from fitting the SSP templates. The $(M/L)_{\rm Salp}$ profile is then extracted directly from this map.

This is a degenerate process, since many different combinations of templates could reproduce the data equally well. To break this degeneracy, a regularisation is applied to the solutions. This regularisation preferentially selects 'smooth' solutions, which are those where the weights of the templates change gradually with age and metallicity. This regularisation does not prohibit non-smooth solutions, which may represent intense and short-lived star-bursts in the population. However, if two different combinations of templates reproduce the spectra equally-well, the smoothest solution will be adopted.

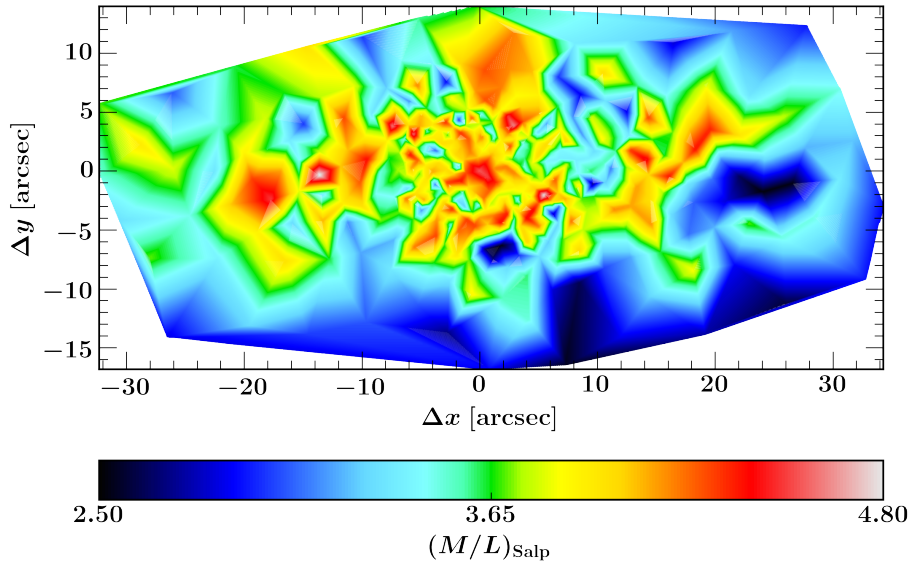

Figure 2.6: The spatially-resolved map of $(M/L)_{\mathrm{Salp}}$ for NGC2685 derived from the best-fitting templates from pPXF.

2.2 Optimisation

A major obstacle for interpreting kinematic data (in particular that of early-type galaxies) is deprojecting the two-dimensional image from the detector into a three-dimensional representation of the galaxy. This is a highly degenerate process. It is clear that early-type galaxies can be either thin and heavily inclined or thick and not inclined, and be indistinguishable by observations. Lifting this degeneracy requires some assumptions to be made about the intrinsic shape of the galaxy. For this work, as in § 1.2.3, this is assumed to be an axisymmetric oblate spheroid. This assumption allows for the determination of an inclination, since projection effects have an impact along only one of the galaxy's axes. Adding to this degeneracy is the issue of the vertical anisotropy, β_z. Since the galaxy can be fit for various values of anisotropy and inclination, it is necessary to find the optimal combination in a quantitative framework.

2.2.1 Least-Squares Fitting

The initial optimisation is done by finding the least-squares fit from a grid of plausible inclination and anisotropy values. Least-squares fitting requires the minimisation of the parameter χ^2, defined as

$$\chi^2 = \sum_k \left(\frac{d_k - m_k\,(i, \beta_z)}{\epsilon_k} \right)^2 \tag{2.2}$$

where d_k are the data points, m_k are the model values for a specific choice of inclination, i, and vertical anisotropy, β_z, and ϵ_k are the residuals of the fit. Thus, a two-dimensional grid of i and β_z values is

iterated over, and the χ^2 is computed for each fit. For this work, the data ranges were sampled linearly in β_z, and intrinsic axis ratio, q. The intrinsic and projected axis ratios, q and q', respectively, are related to inclination as follows

$$q^2 = \frac{(q')^2 - \cos^2(i)}{\sin^2(i)} \tag{2.3}$$

The coordinate in this parameter space that results in the smallest χ^2 is deemed the best-fitting set of parameters.

To ensure this set-up produces valid results, these fits are compared directly to values in the literature. Cappellari (2008) present their least-squares fitting of four galaxies from the ATLAS^{3D} sample. A direct comparison is presented in Figure 2.7. The purpose of these plots is locating the position of the minima, and while the two works do in fact agree within errors in most instances, there are some obvious differences between them that require explanation.

The differences between the two works could have arisen from many different sources. For instance, it is necessary to interpolate between the discrete points of the grid in order to produce the smooth, continuous surface. However, there are a number of interpolation methods - linear, cubic, nearest-neighbour, for instance - that could be used here, and this has the potential to produce slightly varied results.

Other caveats, based on more physical arguments, could also help explain these differences. NGC0524 for instance, was determined to be close to face-on ($i = 20 \pm 5$ °) based on thin dust disks (Cappellari et al., 2006). This means that there is a wide range of inclinations that can match the photometry, with varied levels of galaxy 'thickness'. As a result, the 3-σ contour encloses a 60° range, and so variation between this work and Cappellari (2008) is expected. The determination of the anisotropy, however, is evidently less degenerate and consequently better reproduced in this work. If one further introduces the observationally-motivated (Cappellari, 2008) constraint that $\beta_z \gtrsim 0.05$, then it can be seen that the physically-realistic minimum for NGC0524 is $(\beta_z, i) = (0.05, 18°)$, which agrees well with that found by Cappellari (2008), as well as the inclination determined from dust morphology. This is similarly the case for the other objects with minima in the region $\beta_z < 0.05$. With this consideration, the agreement between the two works is very good.

2.2.2 Markov Chain Monte Carlo

Markov Chain Monte Carlo (MCMC) Bayesian inference techniques are implemented here to more accurately optimise the free parameters, and better characterise the errors of the optimisation, compared

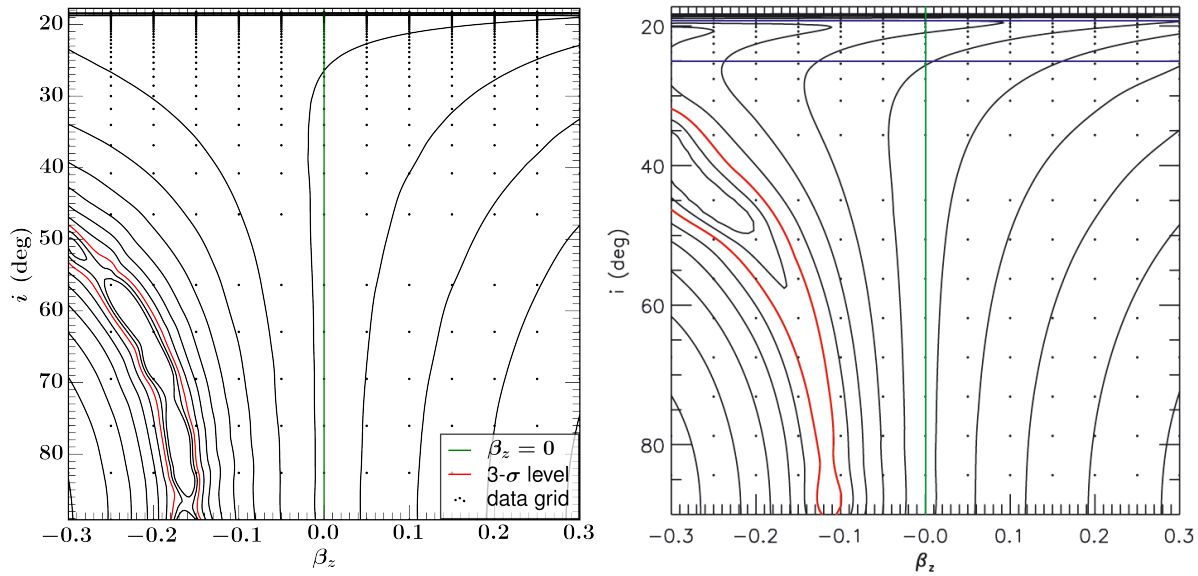

(a) NGC0524

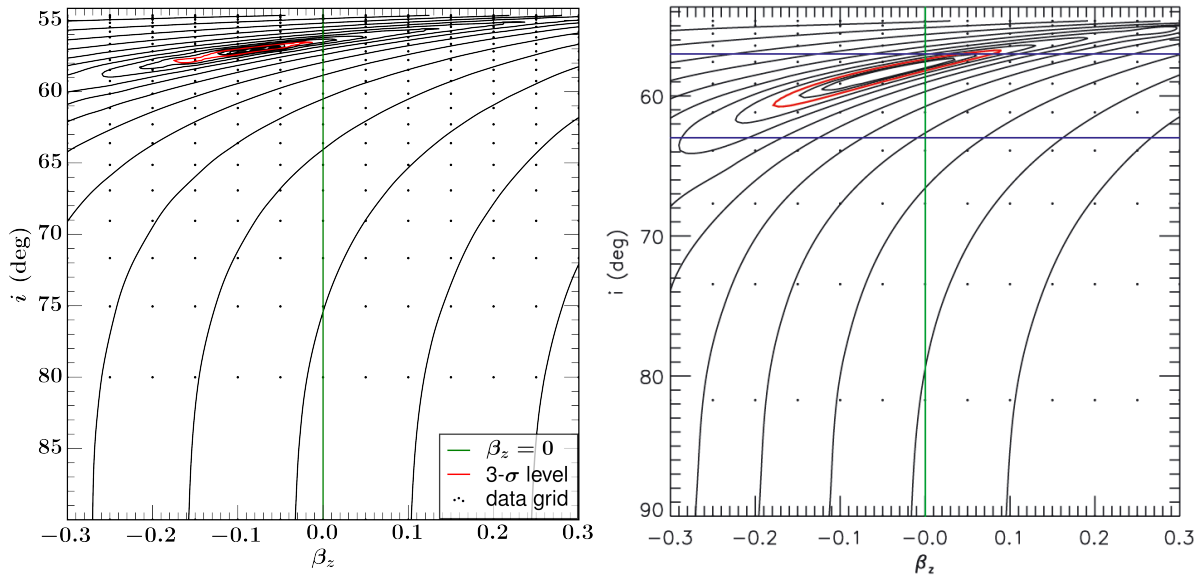

(b) NGC2974

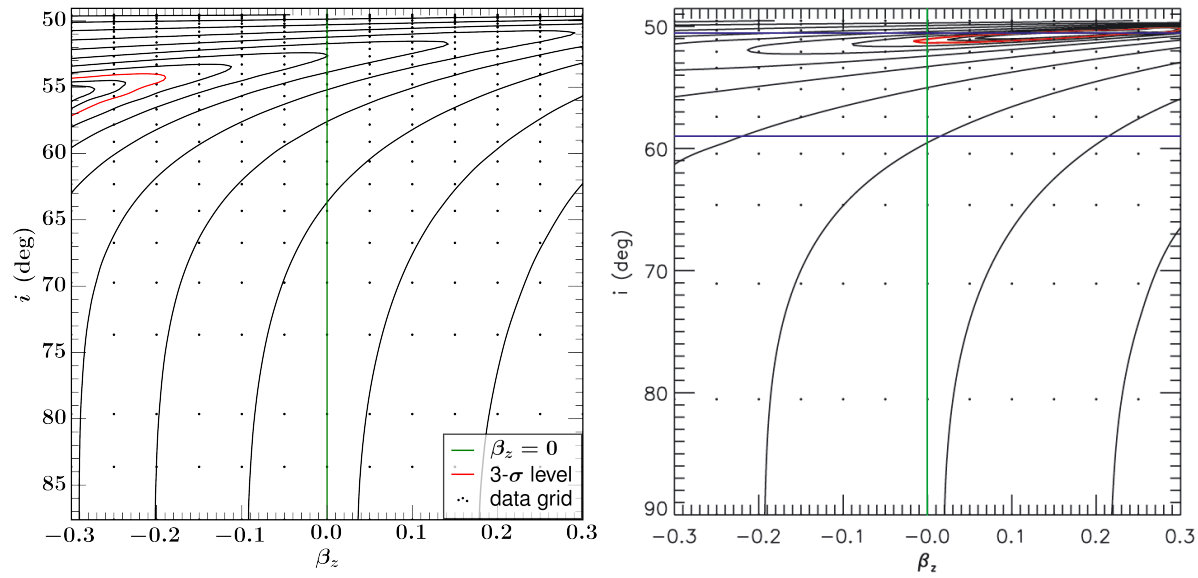

(c) NGC4150

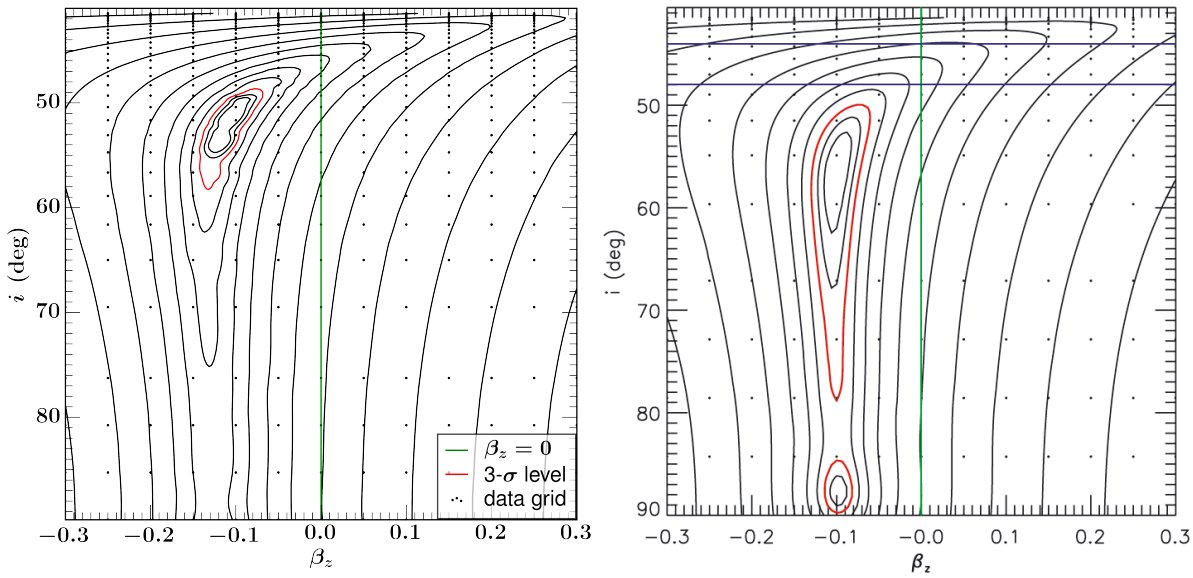

(d) NGC4459

Figure 2.7: A comparison between this work (left column) and Cappellari (2008) (right column) of the χ^2 surface from least-squares fitting. The surface is created by computing a JAM model at each of the points in the underlying grid. This grid is constructed by sampling linearly in β_z and q, which is the reason for the non-linear sampling in i.

to the Least-Squares fitting. MCMC is a fundamentally-probabilistic inference technique, used to draw random samples from a complex distribution where direct sampling is difficult or intractable. In this work, we use these random samples to approximate the distribution itself, from which we extract the sets of parameters that produce the best-fitting model. Since MCMC maximises likelihood, and consequently minimises the χ^2, for consistency and clarity these sets of parameters will be termed optima, rather than minima or maxima. While the difference between the MCMC and Least-Squares fitting methods may be small in a two-dimensional space, the advantages of MCMC become clear as the dimensionality of the parameter space increases, as will be the case in later stages of this work.

Markov Chains

Markov Chains are random processes that are subjected to transitions between states of a parameter space. The defining property of a Markov Chain is that the probability distribution of the current state must depend *only* on that of the previous state. However, the Markov Chains used for MCMC require a few additional constraints. They must be *aperiodic*, so that there is no cyclic behaviour in a finite number of transitions. They must also be *irreducible*, so that it is possible to move from one state to any other state in the space in a finite number of transitions. Irreducibility and aperiodicity are illustrated in Figures 2.8 and 2.9 (from Sandberg, 2007), respectively. The S_i states in the context of

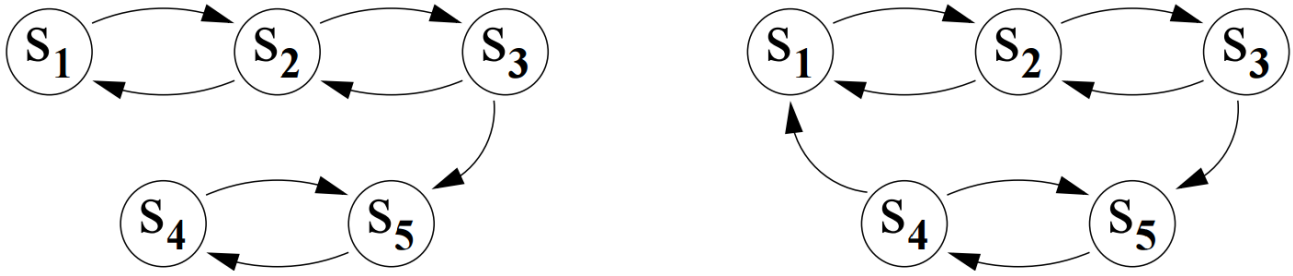

Figure 2.8: An illustration of irreducibility in Markov Chains. It is clear that all states are accessible only in the right-hand chain, and so it is irreducible.

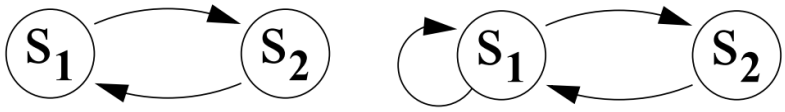

Figure 2.9: An illustration of aperiodicity in Markov Chains. Observe that the Markov Chain depicted by the left-hand chain is $[S_1, S_2, S_1, S_2, \ldots]$. This is clearly periodic, with period 2. The right-hand chain is aperiodic, since from state S_1, the chain can either move to S_2 or remain at S_1, and this decision is non-deterministic.

this work are simply coordinates in the (β_z, i) space, while arrows represent non-zero probabilities of making the transition in the direction illustrated.

After many iterations, the chain will converge to its so-called equilibrium, or 'posterior', distribution. Crucially, as a result of the above constraints on the Markov Chain, it is guaranteed to reach this distribution, *regardless of its initial position*, within a finite number of transitions. The characterisation of this distribution is indeed the primary use of Markov Chains, and in the context of this work, we use this distribution to determine the optimal parameters and associated errors.

Priors

MCMC requires certain input known as "priors". Priors, denoted here as $P(\text{model})$, are probability distribution functions that are specified for each parameter by the user, based on some *a priori* knowledge. In MCMC, the Markov Chain posterior distribution is characterised both by the priors and the distribution of the samples taken during the process. After each iteration of the chain, a decision is made by the Monte Carlo 'walker' as to which direction within the parameter space it will move. The 'likelihood', denoted $P(\text{data}|\text{model})$, of the current state will determine the probability of accepting the new location, whereby states with a high likelihood have a high probability of being accepted. However, acceptance is inherently non-deterministic, since it is based solely on probabilities. Should

the current state be rejected, the walker will return to the previous state and branch off in a different direction. The posterior distribution, $P(\text{model}|\text{data})$, is then estimated using Eq. 2.4 (Cappellari et al., 2013a):

$$P(\text{model}|\text{data}) \propto P(\text{data}|\text{model}) \cdot P(\text{model}) \tag{2.4}$$

Thus, the prior distribution (in general) contributes to the calculation of the direction and size of each step within the parameter space. Following convergence of the chain to its posterior distribution, the coordinate with the highest likelihood is selected as the optimal set of parameters. Using this approach, the regions in which the likelihood is small are avoided (to save computational time), while those regions with a high likelihood are sampled very finely to most-accurately locate the position of the optimal solution, as well improve MCMC's approximation to the posterior distribution.

For this work, flat priors were used for all free parameters. This means that any value within the limits of the parameter space has equal likelihood of occurring. Of course, this is only the case *prior* to the chain beginning. These priors are assumed simply because there is no physical reason why some region of the parameter space should be favoured over others, given the data set that is used for this work.

Posterior Distributions

Typical output of MCMC, characterising the posterior distribution for the 2-dimensional optimisation described above, is shown in Figure 2.10. A known potential pitfall of the MCMC process is the possibility of the walkers falling into a local optimum, rather than the global one, which skews the approximation of the posterior distribution. While the properties of the Markov Chains used for MCMC state that the global optimum will be reached after a finite number of steps, this is not necessarily a small number. As such, it is possible for the process to be terminated prior to this convergence, leaving the walker in the local optimum. To avoid this issue, we set the number of Monte Carlo walkers to 30, which is relatively high given the dimensionality of the space we are optimising within. The reason for this is that even if one walker was to probe a local optimum for the entire process, it is exceedingly unlikely that *all* walkers will follow this path, given the inherently-random nature of Monte Carlo sampling. This assists in probing the posterior distribution more thoroughly.

As with any statistical process, the approximation by MCMC to the 'true' posterior distribution of the Markov Chain improves with increasing total iterations of the MCMC process. Ideally, then, one should opt for the maximum number of iterations possible. However, in order to include more walkers (as above), and given the size of the ATLAS^{3D} sample, the total number of iterations is kept modest

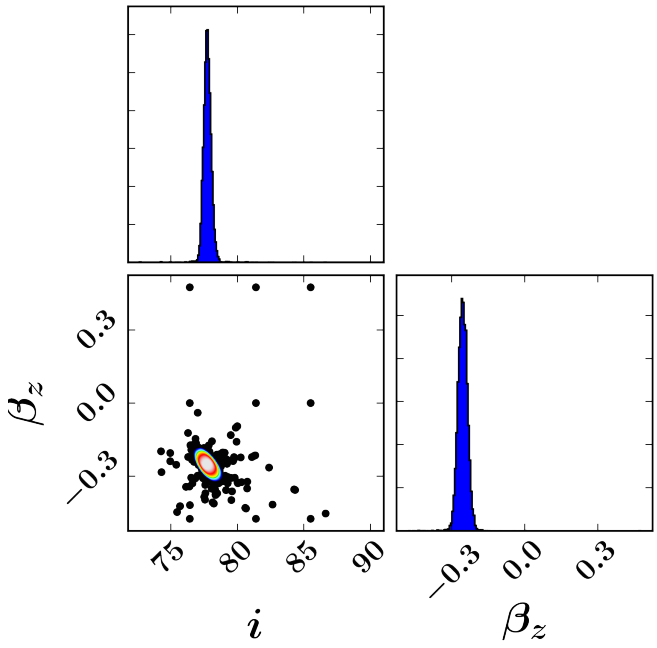

Figure 2.10: Output from the MCMC process for NGC2685. The histograms represent MCMC's approximation to the posterior distribution of the Markov Chain for each parameter. The corner panel shows the correlation between the parameters. The dots are coloured according to their likelihood - black (minimum likelihood) to white (maximum likelihood). The evenly-spaced grid of points overplotted in black shows the initial trial points. This grid was sampled manually prior to the commencement of MCMC, and the point with the highest likelihood was set as the initial position of the MCMC walkers.

to keep the total computation time realistic. To compensate, the entire parameter space is coarsely sampled using the evenly-spaced grid visible in Figure 2.10, prior to the commencement of MCMC. The walkers are then started at the point of the grid with the highest likelihood. This reduces the number of 'wasted' iterations that would have occurred in regions of very low likelihood. For each galaxy, each of the 30 walkers conducted 800 iterations, giving a cumulative total of $24,000$ steps. This is shown to be sufficient for convergence, given the smooth and clearly-defined distributions such as those in Figure 2.10.

Table 2.2 directly compares the optima, as determined by Least-Squares and MCMC techniques, for NGC2685. Given that MCMC can probe the space on finer scales, provides estimates of the errors, and is much more effective at handling higher-dimensional spaces, it is the clear choice for this work, and is subsequently used for all such parameter inferences.

	Least-Squares	MCMC
β_z	-0.2500	-0.2510 ± 0.0192
i	77.9683	77.7147 ± 0.2901

Table 2.2: The optimal solutions as determined by Least-Squares and MCMC optimisation techniques, for NGC2685. The input data are identical. The clear advantages of MCMC are being able to sample 'in between' the rigid grid points of Least-Squares, and estimating the uncertainties.

Implementation

The actual MCMC computation is done in Python, using an implementation of the Metropolis-Hastings algorithm (Hastings, 1970) termed EMCEE (Foreman-Mackey et al., 2013). Another package, PYMC (Fonnesbeck et al., 2015), was also trialled, however there are a few technical differences that made EMCEE the preferred package. For instance, the optimum in PYMC is taken as the mean of the posterior distribution after the total number of iterations. However, this method tends to depend on the amount of "burn-in" specified. The burn-in in MCMC is the number of iterations that are removed from the start of the chain. This is done to remove any effects of both the initial position of the walkers (which may or may not be arbitrarily specified), as well as the initial transitions, which are likely to be far from the optimum. These iterations would clearly skew the posterior distribution away from the optimum, so burn-in is recommended. However, there is no clear prescription for how many iterations to burn. In addition, PYMC sends one Monte Carlo walker to conduct the total number of iterations, while many walkers are desired for reasons previously stated. In addition to avoiding local optima, using many walkers with EMCEE allows for effective multi-threading (since each walker's path is completely independent of the others) which dramatically reduces computation time. Thus, to remove the dependence on burn-in and include many walkers, EMCEE is used throughout this work. EMCEE simply selects that coordinate with the highest likelihood, which clearly has no dependence on any other iteration, including the initial few. It also allows for the specification of the number of walkers to divide the total number of iterations amongst.

The correlation panel in Figure 2.10 shows the full range of each parameter that could have been probed by the MCMC walker (plus some numerical padding for aesthetics only). The limits for β_z are set at ± 0.5. Anisotropies of this magnitude are quite extreme, and we observe that the Monte Carlo walkers do not approach these limits in realistic models. However, they are set as such to give the walkers sufficient freedom. The inclination bounds need to be set dynamically for each galaxy. The JAM model requires that the minimum (intrinsic) axis ratio $q_{\min} \geq 0.05$. To find the minimum inclination bound, we consider the flattest projected axis ratio in the MGE. In the definition of Scott

et al. (2013), the flattest axis ratio corresponds to the minimum value from Column (3) of Table 2.1, which in turn sets the minimum for how face-on the galaxy can be. Mathematically, we solve Eq. 2.3 for $i_{\rm min}$ by setting q' to the flattest projected axis ratio and $q = 0.05$. The maximum inclination is set to 90°, which corresponds to a completely edge-on galaxy.

2.3 Mass-follows-Light

We present here our JAM models of the full ATLAS^{3D} sample, without yet introducing the $(M/L)_{\rm Salp}$ gradient. We do this to verify our optimisation and modelling process, as well as to provide the benchmark for which we compare later results to. For this benchmark, the mass is assumed to follow the light exactly, which corresponds to Model **(A)** from Cappellari et al. (2013a). This assumption implies that the MGEs for the light and gravitational potential are identical. Dark matter is not disregarded in this way, but rather it is assumed to be spatially distributed exactly like the luminous matter. Within 1 R_e, which is approximately the extent of the ATLAS^{3D} data, this is a reasonable assumption, since the baryonic matter is believed to dominate in this region (Cappellari et al., 2013a). When conducting the JAM fit, the central 2″ is excluded from the fit to avoid any bias to the observed velocity distribution of the inner-most stars due to the presence of a supermassive black hole with uncertain mass (though a point mass is included in our models to account for this black hole, with mass derived from the relation of Ferrarese & Merritt (2000)). This region is excluded throughout this work for all JAM models produced. Our initial benchmark and comparison to the literature is presented in Figure 2.11.

As can be seen, the agreement between our models and those of Cappellari et al. (2012) is very good. It is clear that for the lower-mass galaxies, the dynamical masses inferred from modelling agree well with Chabrier- or Kroupa-like IMF slopes, while intermediate-mass galaxies prefer a Salpeter-like slope. The heaviest galaxies tend towards 'heavier' IMF slopes. Since $\alpha_{\rm dyn.}$ is a mass normalisation, we know only that the inferred slope of the IMF for these galaxies is significantly deviant from that of a Salpeter. Galaxies in this mass range could be described by either a bottom-heavy IMF, where there is an abundance of low-mass stars, or a top-heavy IMF, which contains the remnants of high-mass stars. Thus, the blue line is degenerate in slope between $\alpha = -2.8$ and $\alpha = -1.5$. Indeed, this may explain why there is a comparatively broad range of galaxy masses with $\alpha_{\rm dyn.} \sim 1.5$. In addition to the general trend of $\alpha_{\rm dyn.}$, the trend in velocity dispersion is matched equally well in our work.

While Figure 2.11 provides a convenient visual comparison, it shows only that the two works agree on

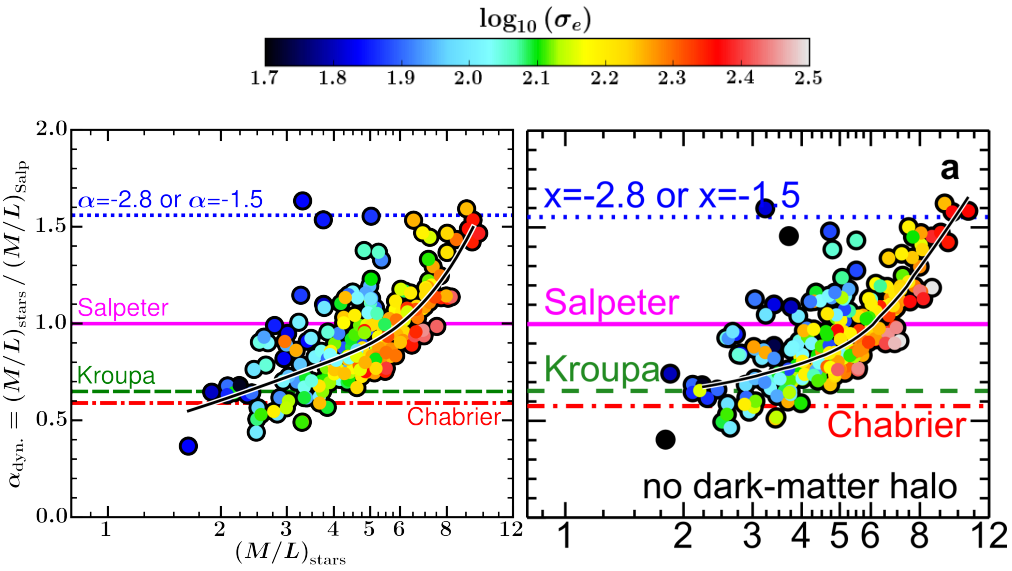

Figure 2.11: A comparison of the variation in the IMF mis-match parameter $\alpha_{\rm dyn.}$ between this work (left panel) and Cappellari et al. (2012) (right panel). The horizontal lines mark various power-law IMFs, with slopes of Chabrier (red dot-dashed line), Kroupa (green dashed line), Salpeter (magenta solid line), and either -2.8 or -1.5 (blue dotted line). The data points are coloured by effective velocity dispersion, σ_e.

average - that is, the qualitative trends match. A quantitative comparison is presented in Figure 2.12, where the published values of $(M/L)_{\rm stars}$ from Cappellari et al. (2013a) (Column (6), Table 1) are compared directly to the values determined by this work. The agreement here is excellent. From the coefficients of the straight-line fit, it can be seen that deviations from an ideal correlation are less than 1%. Points denoted by $\times$ are those which have a data quality of 0 as listed in Column (8) of Table 1 in Cappellari et al. (2013a). A data quality of zero indicates that the IFU data contains any combination of low (S/N), prominent bar or dust features, or usual kinematic features such as counter-rotating components. These factors negatively affect the JAM model, and these objects are hence excluded from conclusions drawn. Such objects are consistently represented by $\times$ symbols throughout this work.

The main goal of our work is to take into account the effects of stellar population variations on the results of Cappellari et al. (2012). Having matched their results adequately with our own modelling, we now introduce these effects in the form of a $(M/L)_{\rm Salp}$ gradient. To observe its effect on the IMF, we thus attempt to reproduce Figure 2.11 in both the Scaled Potential (Chapter 3) and General Power Law (Chapter 4) methods, in order to compare and contrast with our benchmark.

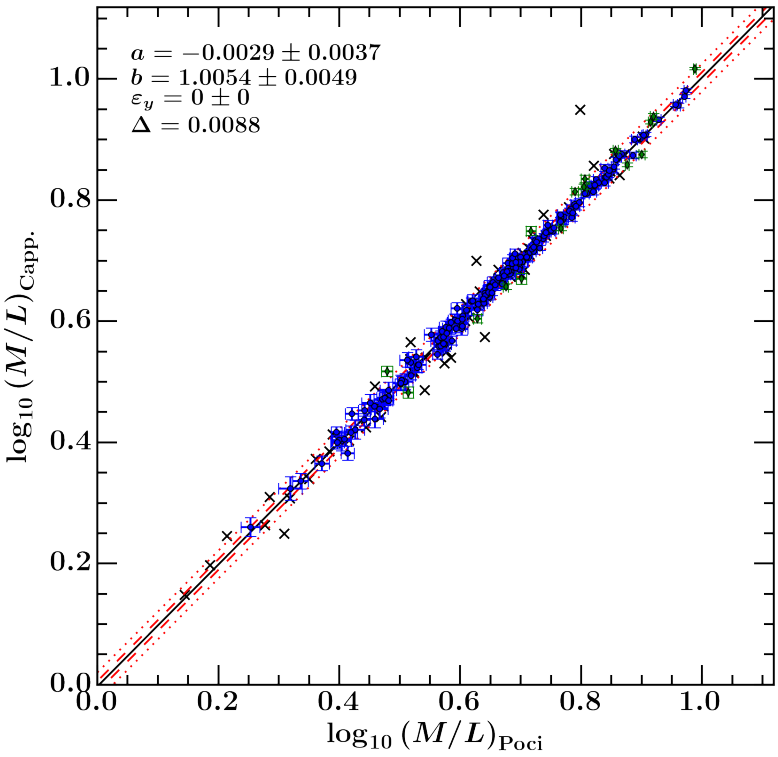

Figure 2.12: A direct, quantitative comparison of the $(M/L)_{\rm stars}$ between Cappellari et al. (2013a) and this work for the mass-follows-light model. The figure was made using the LTS_LINEFIT procedure of Cappellari et al. (2013a). The green diamonds are those points which are automatically excluded by LTS_LINEFIT from the fitting process. All blue and green points have error bars. The black line is the best-fitting line of the general form $y = a + b\,(x - x_0)$ (with $x_0 = 0$ in this case, and a and b inset). The dashed and dotted red lines are the 1- and 2.6-σ ranges, respectively (enclosing 68% and 99% of the values, respectively). ε_y is the intrinsic scatter, and Δ is the observed scatter. Points with quality 0 are overplotted, but excluded from the fit.

3

Scaled Potential

3.1 Methodology

In our first approach to incorporate the effects of spatial variations in the stellar populations, and consequently in the stellar M/L, the MGE describing the gravitational potential is scaled by the measured M/L at every spatial location. We thus refer to this as the Scaled Potential method. In order to compute the scaling values, we convert the two-dimensional map of $(M/L)_{\text{Salp}}$ given in Figure 2.6 into a one-dimensional profile. To do this, the map is parametrised on elliptical annuli aligned with the kinematic position angle, as measured by Krajnović et al. (2011). The annulus that will scale the j-th Gaussian has a radius of σ_j, with a maximum thickness of $3''$. Here, we have equated the physical radius to the dispersion of the Gaussians. To justify this, note that the j-th Gaussian contributes maximally at σ_j. As a result, it is reasonable to set $\sigma \approx r$. The thickness is reduced for consecutive Gaussians that are less than $3''$ apart, to produce contiguous annuli with the common border half-way between the two dispersion values. The j-th annulus has ellipticity $1 - q'_j$, to ensure the shape of the annuli match the Gaussians of the MGE. The profile is then composed of the mean $(M/L)_{\text{Salp}}$ values within each of the annuli. Thus, the scaling of the j-th Gaussian occurs as follows:

$$T'_j = T_j \times (M/L)_{\text{Salp}}\,(\sigma_j) \tag{3.1}$$

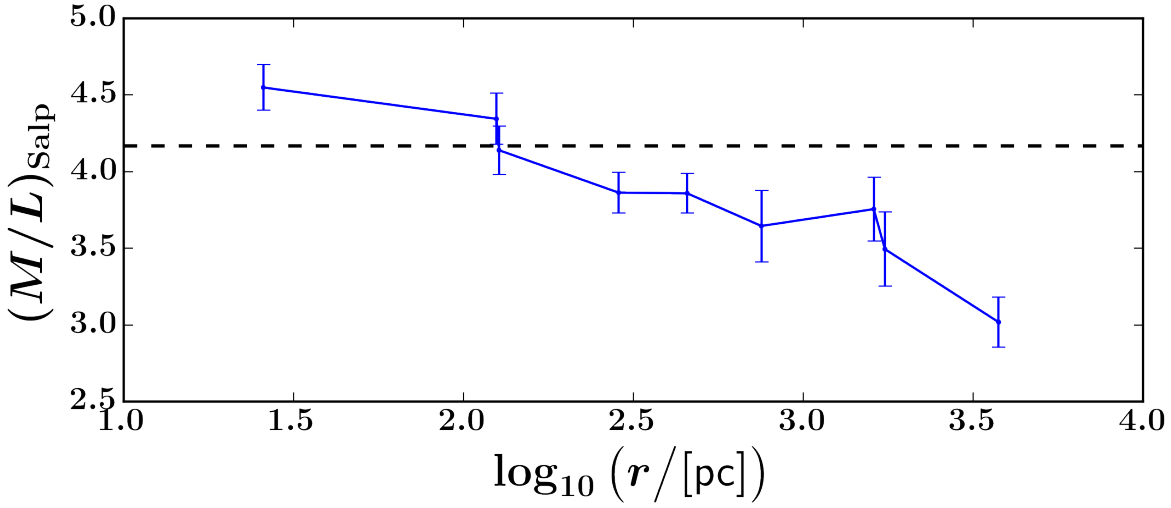

Figure 3.1: The $(M/L)_{\rm Salp}$ profile of NGC2685. Each data point is the mean value of the annulus of radius σ_j. The error bars are computed from the standard deviation of the $(M/L)_{\rm Salp}$ values within each annulus. The black dashed line is the luminosity-weighted constant $(M/L)_{\rm Salp}$ (Cappellari et al., 2013b) that is assumed for our initial benchmark in § 2.3.

where T'_j and T_j are the scaled and unscaled total counts, respectively, of the j-th Gaussian, and $(M/L)_{\rm Salp}(\sigma_j)$ is the value of the profile at σ_j. Crucially, the Gaussians referred to here are *only* from the MGE that describes the gravitational potential, since of course the light remains unchanged. It can be seen that Eq. 3.1 is effectively converting a surface brightness [$L_\odot$ pc^{-2}] into a mass surface density [$M_\odot$ pc^{-2}].

A typical $(M/L)_{\rm Salp}$ profile is given in Figure 3.1. It is clear from the profile that the spatial variation in the stellar M/L is significant. It has been shown that changes in the stellar M/L are closely linked to variations in age and metallicity within the stellar population (Kuntschner et al., 2010). In particular, metallicity is seen to decline with galactic radius (for example, see Forbes et al., 2011; La Barbera et al., 2012). Metallicity affects the opacity of the stars, which in turn directly impacts the observed luminosity. Thus, for decreasing metallicity, the measured L is increased due to lower opacity, subsequently reducing M/L in agreement with the general trend presented in Figure 3.1. It should be noted that the discontinuities present in the figure are simply plotting artefacts, since the MGE is computed at discrete locations. Following the scaling by this profile, both MGEs are given to JAM, and the modelling proceeds as it did in § 2.3. Since the only aspect of the models we change here is the introduction of the $(M/L)_{\rm Salp}$ profile, we emphasise that this is still under the assumption of mass-follows-light.

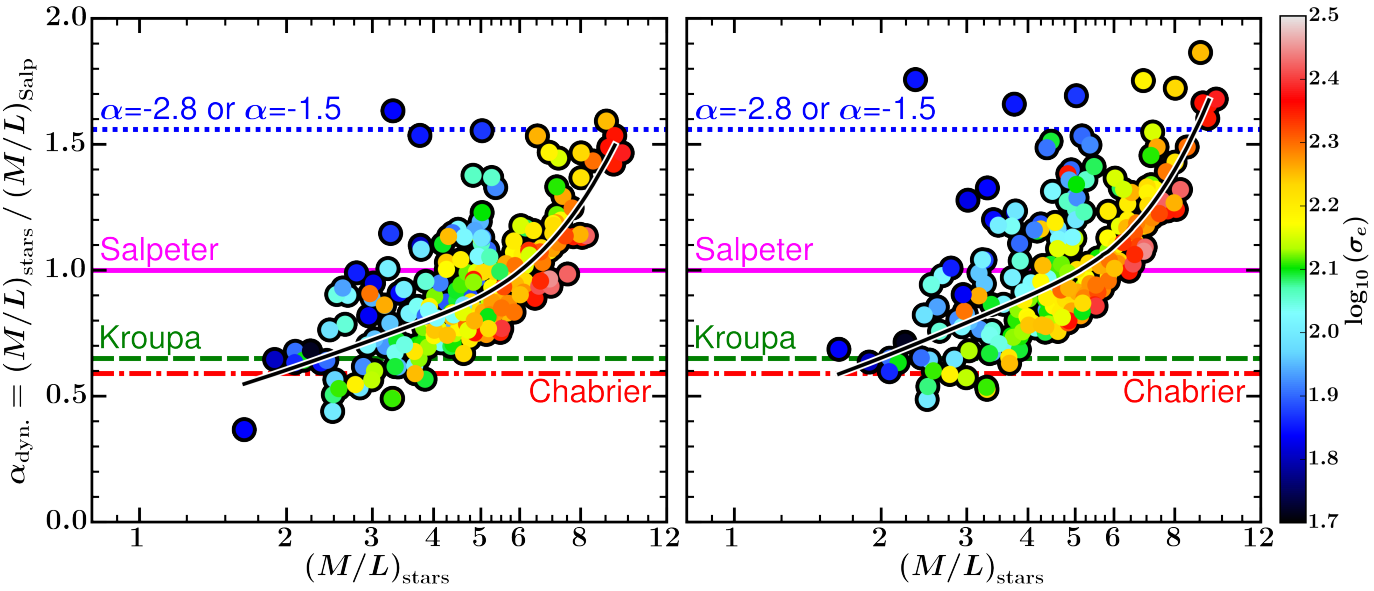

Figure 3.2: The observed variation of $\alpha_{\rm dyn.}$ for the Scaled Potential method (right panel) contrasted with the initial benchmark (left panel). Note the elevation of $\alpha_{\rm dyn.}$ in this method compared to mass-follows-light, and the increased gradient of the trend at high mass. Crucially, the IMF is still required to vary systematically, even taking the spatial variations in stellar populations into account.

3.2 Results & Discussion

The variation of $\alpha_{\rm dyn.}$ with $(M/L)_{\rm stars}$ as computing using the Scaled Potential method is presented in Figure 3.2. The most obvious conclusion from this result is that the systematic variation published by Cappellari et al. (2012) is not removed by accounting for radial variations in the stellar M/L, which are due to age and metallicity variations. This further strengthens evidence for a non-universal IMF. In addition, Figure 3.2 shows a general shift to higher $\alpha_{\rm dyn.}$, compared to Figure 2.11. The luminosity-weighted spatially-constant $(M/L)_{\rm Salp}$ value that was assumed for the mass-follows-light method is shown in Figure 3.1. The M/L from the central regions dominate the computation of this value, because they contribute more light compared to the outer regions. However, it can be seen that the outer values are relatively low, which are believed to be the result of (in general) lower metallicities in the outer regions (Kuntschner et al., 2010). Specifically, these outer values are lower than the constant $(M/L)_{\rm Salp}$ value. Since in the Scaled Potential method we no longer compute a single average, but rather multiple values at various radii, the outer regions have a more significant impact on the model. The net result is that $(M/L)_{\rm Salp}$ is reduced, with respect to the values in the mass-follows-light models, consequently increasing $\alpha_{\rm dyn.}$. The magnitude of this shift would depend on the $(M/L)_{\rm Salp}$ profile itself, which of course varies between galaxies. In addition to the elevation, Figure 3.2 appears to show a steeper trend, in particular in the low-mass region, when compared to Figure 2.11. We note that the

colours of the points represent the central velocity dispersion of each galaxy, and show a weak trend of increasing mass normalisation, $\alpha_{\mathrm{dyn.}}$, for increasing velocity dispersion, as found by others (Cappellari et al., 2013a; La Barbera et al., 2013; Spiniello et al., 2014).

There are a number of areas in which this method could be refined. For instance, since the stellar MGEs are computed from SDSS images, they are significantly more extended than the SAURON field. This poses an issue regarding the computation of, and scaling by, the $(M/L)_{\mathrm{Salp}}$ profile. The profiles are computed from the SAURON data, and so the outer-most Gaussians of the MGE do not have corresponding annuli in the $(M/L)_{\mathrm{Salp}}$ map. To resolve this issue for this work, all the Gaussians outside the SAURON field were scaled by the $(M/L)_{\mathrm{Salp}}$ value of the outer-most annulus. This was done to avoid complex curve-fitting, since these $(M/L)_{\mathrm{Salp}}$ profiles are in general neither monotonic nor a straight-line gradient. In addition, the spacing of the dispersion values of the Gaussians is often very irregular, further complicating attempts to fit curves. One possible resolution to this issue would be taking data using IFUs with larger fields. This is currently undergoing development, in fact, with instruments such as MUSE (Bacon et al., 2010) recently acquiring first-light. Alternatively, dynamical models have been made by combining current IFU observations of central regions with long-slit spectroscopy of the outer regions (Cappellari et al., 2015), to probe the galaxies on scales more akin to the extent of the MGEs.

4

General Power Law

4.1 Methodology

The mass-follows-light and Scaled Potential methods utilise Model **(A)** of Cappellari et al. (2013a), which assumes any dark matter that may be present follows the same spatial distribution as the observed luminosity. For this method, however, we make use of Model **(D)**, which is composed of a JAM model with a generalised spherical Navarro, Frenk, and White (NFW) dark matter halo (Navarro et al., 1996), in addition to the stellar component. An NFW halo profile is a broken power law with a slope of -1 for the inner region, and -3 for the outer region. However, it has been seen that attempting to describe both baryonic and dark matter can result in predictions of densities in the inner region that do not match observations. For instance, Gnedin et al. (2004) explain that the difference in geometry of the dark and baryonic components can lead to an overprediction of the inner dark matter densities. This is the result of the dark component typically being treated by assuming adiabatic contraction (on spherical shells), while the baryons are subject to violent (highly-elliptical) mergers within these haloes. Thus, in order to describe the total (stellar plus dark) mass distribution in our galaxies, we adopt the generalised total mass-density power law presented by Wyithe et al. (2001) (based on the analytic models of Zhao (1996)). We thus refer to this approach as the General Power Law method. Given in Eq. 4.1, and illustrated in Figure 1.6, the use of this power law in the context of our work is motivated by the work

of Barnabè et al. (2012) and Cappellari et al. (2015).

$$\rho_{\text{Tot.}}(r) = \frac{\rho_s}{2}\left(\frac{r}{r_s}\right)^{\gamma'}\left(1+\frac{r}{r_s}\right)^{-\gamma'-3} \tag{4.1}$$

where r_s is the break radius, ρ_s is the density at the break radius, and γ' is the slope of the profile. This break radius is that at which the density profile is exactly isothermal ($\rho(r) \propto r^{-2}$). The "generality" of this power law arises from the fact that it allows for a central region with a slope that is distinct from (though not independent of) the outer one. For this work, r_s is held fixed at 20 kpc. This is the optimal value found by Cappellari et al. (2013a), who also show that, since the extent of the data is always significantly less than 20 kpc, fitting for this parameter has a negligible effect on the results.

Using similar MCMC techniques to those described in § 2.2.2, the free parameters of this profile, $\log_{10}(\rho_s)$ and γ', are optimised by finding the best-fit JAM model to the ATLAS^{3D} kinematics. We thus have four free parameters for this method, $(\beta_z, i, \log_{10}(\rho_s), \gamma')$, requiring MCMC optimisation within a four-dimensional space. An example of this optimisation is presented in Figure 4.1.

In this expanded parameter space, at each iteration of MCMC, the current values of γ' and $\log_{10}(\rho_s)$ are used to create a new MGE model for the gravitational potential using the MGE_FIT_1D procedure of Cappellari (2002). This MGE is then, along with the *unscaled* stellar MGE, passed to JAM to fit to the kinematics and compute the likelihood of that coordinate.

The ranges of β_z and i remain identical to those used in previous methods. The limits on $\log_{10}(\rho_s)$ are set to ±6. Like β_z, we do not observed such extreme values in our models, and thus they are set as such to provide sufficient freedom to the Monte Carlo walkers. γ' is bounded between $-4 \leq \gamma' \leq 0$. The upper bound of 0 is set because it is physically unreasonable to allow for the total density to increase with radius. Slopes steeper than -4 are similarly never observed in any of our realistic models.

Following the convergence of MCMC, the most likely values of γ' and ρ_s are inserted into Eq. 4.1 to construct the best-fitting total mass-density profile. Since the main objective of this work is to constrain the IMF, it is necessary at this stage to decompose this profile into its stellar and dark matter components. Note that a key advantage of this General Power Law approach is that since the stellar MGE is fed to JAM unscaled, and the subsequent decomposition is conducted only on the region $2'' \leq r \leq r_{\text{max}}$, what happens to the stellar M/L outside this range is of no consequence. Whereas for the Scaled Potential method, the $(M/L)_{\text{Salp}}$ profile was extrapolated beyond the spectral data, for the General Power Law method, the stellar M/L beyond the region considered in the decomposition can be explicitly ignored, and therefore has no influence on the IMF and dark matter fraction inferred for

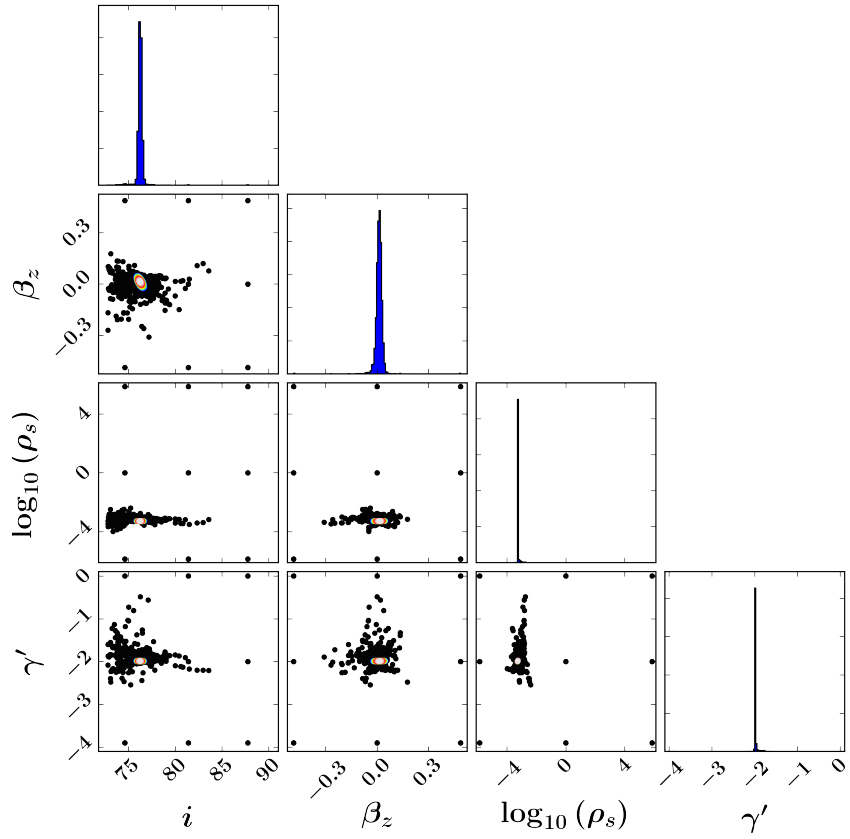

Figure 4.1: Typical MCMC output for the 4-dimensional parameter space of the General Power Law approach. This is completely analogous to Figure 2.10, but shows the correlations between all pairs of parameters.

the regions where we have spectroscopic data.

In order to maintain generality, we describe the dark matter density profile with a generalised NFW profile. It has the same form as Eq. 4.1, but with a fixed slope of -1, respecting the NFW model. This is given in Eq. 4.2

$$\rho_{\rm DM}(r) = \frac{\rho_{{\rm DM},s}}{2}\left(\frac{r}{r_s}\right)^{-1}\left(1+\frac{r}{r_s}\right)^{-2} \tag{4.2}$$

where $\rho_{{\rm DM},s}$ is the density of dark matter at the break radius, and r_s remains fixed at 20 kpc as above.

The stellar profile is constrained by the MGE fit to SDSS imaging data. However, for consistency with the spherical total and dark matter profiles, we must 'circularise' the stellar MGE - that is, transform the shape of the Gaussians from elliptical to circular, whilst conserving their integrated mass. This is done because we aim to compare all three profiles directly, and is achieved with the following mapping (Cappellari et al., 2013a)

$$(\sigma_j, q'_j) \longrightarrow \left(\sigma_j\sqrt{q'_j}, 1\right) \tag{4.3}$$

The profile is constructed directly from the stellar MGE, using the circularised components and the following equation (from Cappellari et al. (2015))

$$\rho_{\rm star}\,(r) = \alpha_{\rm dyn.} \sum_{j=1}^{N} \frac{M_j \exp\left[-r^2 \big/ 2\sigma_j^2\right] \operatorname{erf}\left[r\sqrt{1-\left(q'_j\right)^2} \,\big/\, \left(q'_j\right)\sigma_j\sqrt{2}\right]}{4\pi\sigma_j^2 r\sqrt{1-\left(q'_j\right)^2}} \tag{4.4}$$

where global scaling constant is exactly the $\alpha_{\rm dyn.}$ parameter from previous analyses, and is the only free parameter of this equation. M_j, σ_j, and q'_j are the deprojected mass, dispersion, and axis ratio of the j-th Gaussian, respectively. The deprojected mass of the Gaussians is computed in two steps:

1. Compute the deprojected luminosity, L_j [$\mathrm{L}_\odot$], from the surface brightness of the stellar MGE using

$$L_j = 2\pi T_j \sigma_j^2 q'_j \tag{4.5}$$

   as in Cappellari et al. (2013a).

2. Scale each Gaussian by its corresponding value of the $(M/L)_{\rm Salp}$ profile to convert the deprojected luminosity into a deprojected mass, M_j [$\mathrm{M}_\odot$], as

$$M_j = L_j \times (M/L)_{\rm Salp}\,(\sigma_j) \tag{4.6}$$

In this way, the General Power Law method retains the additional constraint of stellar population information, however it is introduced *after* fitting to the original data (that is, without any direct scaling of the gravitational potential).

It is then necessary to constrain $\alpha_{\rm dyn.}$ and $\rho_{{\rm DM},s}$. To do this, we set $\rho_{\rm Tot.} = \rho_{\rm star} + \rho_{\rm DM}$, and find the best combination of $\alpha_{\rm dyn.}$ and $\rho_{{\rm DM},s}$ to fit $\rho_{\rm Tot.}$. A typical decomposition is presented in Figure 4.2. These fits are conducted only in the region $2'' \leq r \leq r_{\rm max}$. Since the central $2''$ is excluded from the JAM model (§ 2.3), the JAM model is not constrained by the data within this region. We thus omit it from the fit of the density profiles. Furthermore, some galaxies in the sample have an effective radius that is larger than the extent of the SAURON observation (see Column (13) of Table A1). Thus, $r_{\rm max}$ - the largest elliptical coordinate within the SAURON data - is set as the upper limit instead of R_e, meaning we consistently fit only where we have kinematic data.

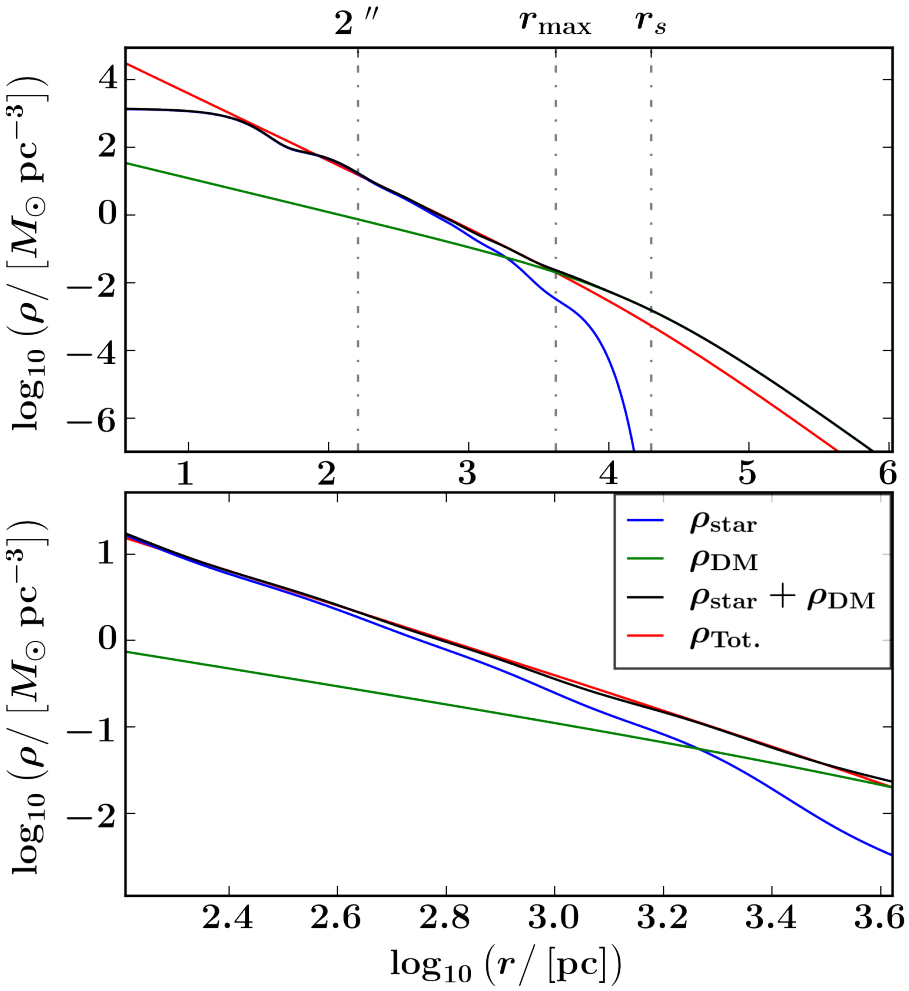

Figure 4.2: The decomposition of the total mass-density profile of NGC2685 into its stellar and dark components. The top panel is the full radial extent of the profiles. The bottom panel zooms in on the region that was used to make the fit, which is bounded by $2'' \leq r \leq r_{\max}$. The break radius is shown for scale.

4.2 Results & Discussion

4.2.1 IMF Constraints

The variation of $\alpha_{\mathrm{dyn.}}$ with $(M/L)_{\mathrm{stars}}$ as computed using the General Power Law method is presented in Figure 4.3. Once again, it is clear that taking into account stellar population effects, as well as the dark matter halo, does not eliminate the systematic trend of the IMF normalisation. In addition, this method produces systematically-lower $\alpha_{\mathrm{dyn.}}$ values compared to both methods presented above. In § 3.2, we posited that the systematic increase from the Scaled Potential method was due to the fact that accounting for the spatial variation in M/L had the net result of reducing $(M/L)_{\mathrm{Salp}}$. Here, however, the dark matter halo is able to account for some of these mass differences. This allows for the mass

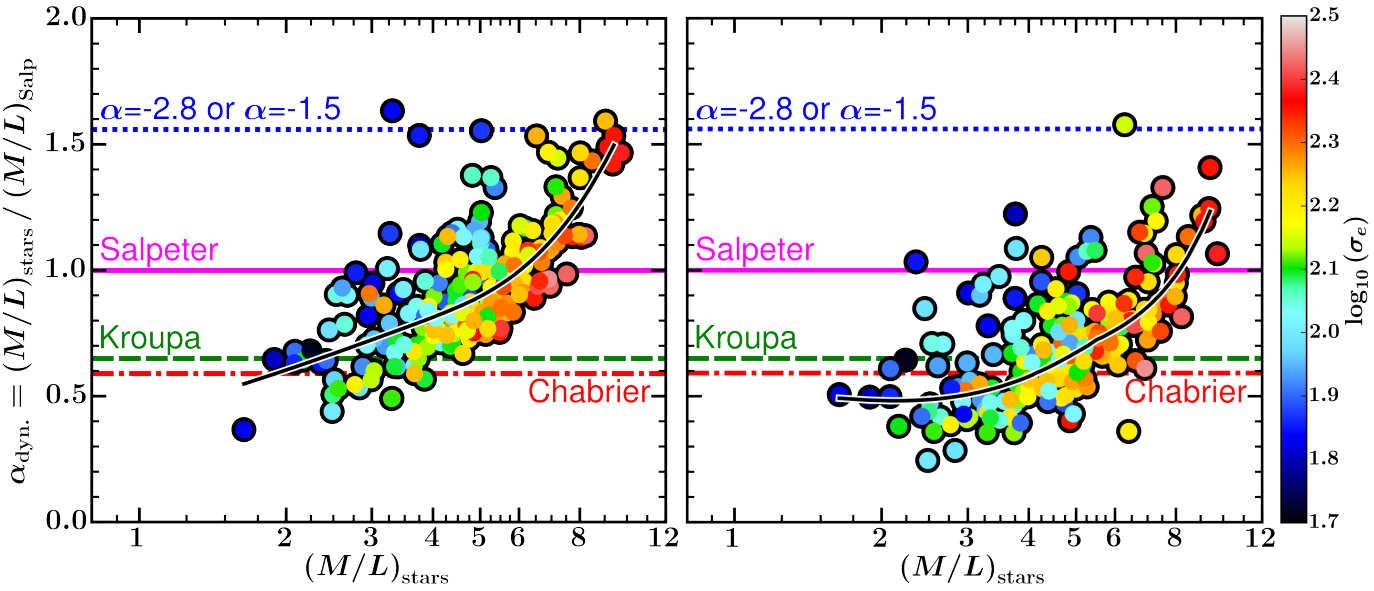

Figure 4.3: The observed variation of $\alpha_{\rm dyn.}$ for the General Power Law method (right panel) contrasted with the initial benchmark (left panel). Note the reduction in $\alpha_{\rm dyn.}$, compared to both methods considered earlier. Crucially, the trend of higher $\alpha_{\rm dyn}$ for higher $(M/L)_{\rm stars}$ persists after taking into account stellar population and dark matter effects, with the generalised potential technique.

attributed to stellar populations to be reduced, and balanced by the dark matter content. That is, the M in $(M/L)_{\rm stars}$ is reduced, consequently reducing the $\alpha_{\rm dyn.}$ parameter. Indeed, this is also observed in the original results from Cappellari et al. (2012), where all models considered in Figure 1.5 (except the mass-follows-light; Panel **a**) show similarly reduced $\alpha_{\rm dyn.}$ values, all of which include explicit treatments of dark matter.

4.2.2 Dark Matter Fractions

Unlike the mass-follows-light approach employed with the Scaled Potential method, the General Power Law approach allows us to explicitly separate the contributions to the gravitational potential into stars and dark matter. The main motivation for this was to further refine our determination of $\alpha_{\rm dyn.}$ by accounting for independent stellar and dark matter profiles, in addition to the spatially-varying stellar M/L. Consequently, we also use this approach to estimate the dark matter fraction using the best-fitting value of $\rho_{\rm DM,s}$ in Eq. 4.2. To do this, we integrate the best-fitting dark matter profile up to R_e, and find the ratio with the total mass profile, which is also integrated up to R_e. These determinations are presented in Figure 4.4. The green curve is given by Cappellari et al. (2013a), and is determined from abundance-matching techniques of cosmological simulations (Moster et al., 2010), which aim to

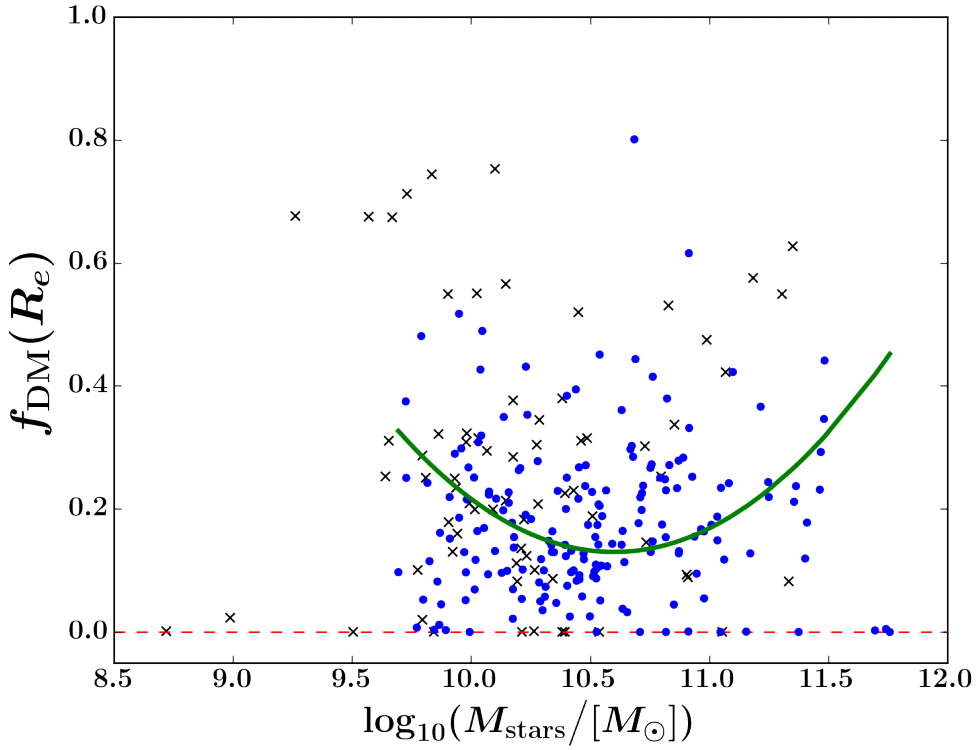

Figure 4.4: The fraction of dark matter within 1 R_e is shown as the blue points for data quality > 0, and crosses for data quality = 0. $M_{\rm star}$ is the stellar mass inferred from the integrated stellar density profile. The green curve (given in Eq. 4.7) is an empirical fit to the dark matter fractions inferred by Cappellari et al. (2013a), assuming dark matter halo masses from abundance-matching in CDM simulations (Moster et al., 2010).

match CDM halos to their corresponding baryonic galaxies, based on the galaxy and DM halo mass functions. As a result, their dark matter fractions have an explicit mass-dependence, determined to be

$$f_{\rm DM} \sim 0.13 + 0.24 \times \left(\log_{10}\left(M_{\rm stars}\right) - 10.6\right)^2 \tag{4.7}$$

The scatter in our estimates is too large to constrain the nature of any trend present. We note that Cappellari et al. (2013b) also find an increase in scatter when the DM halo is fitted explicitly (as is the case for our result), compared to imposing a fixed halo from cosmological simulations.

In the current implementation, the slope of the dark matter power law is fixed at -1. In future work, we look to leave this slope as a free parameter, and fit for it along with $\alpha_{\rm dyn.}$ and $\rho_{{\rm DM},s}$ during the decomposition stage. This will allow more general determinations of both the central dark matter fraction, and the IMF parameter, since they are extracted from the same fit.

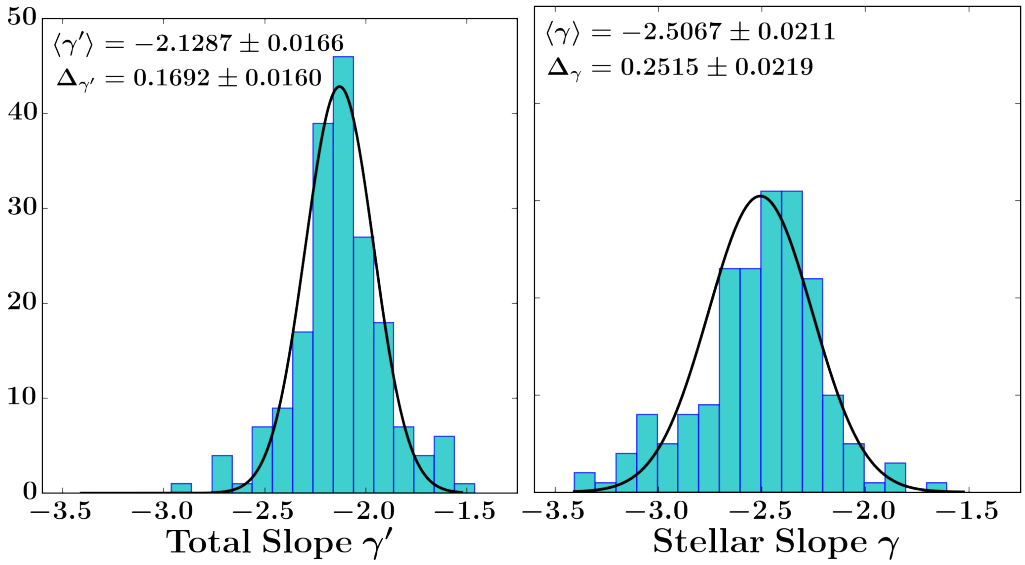

Figure 4.5: A comparison of the total slope distribution (left panel) and the stellar slope distribution (right panel) for all galaxies with a data quality > 0. Inset are the mean and scatter, with associated errors. The stellar slopes are computed directly from the MGE, *after scaling by the* $(M/L)_{\rm Salp}$ *profile*, as the mean logarithmic slope given by $\gamma = -\Delta \log_{10}(\rho_{\rm star}) / \Delta \log_{10}(r)$. This is calculated within the region $2'' \leq r \leq r_{\rm max}$.

4.2.3 Mass-Density Profile Slopes

The slopes of both the total and stellar mass-density profiles can be extracted as a result of the modelling conducted in the General Power Law approach, and are used to explore the relationship between these profiles, if any. The total mass-density profile slope, γ', is a free parameter of the fit to the ATLAS^{3D} kinematics, and is thus determined directly from the MCMC optimisation. The slope of the stellar profile, γ, is found by decomposing the total density profile into its stellar and dark matter components, as described in §4.1. The slope is then computed as the mean logarithmic slope of the best-fitting stellar profile, given by $\gamma = -\Delta \log_{10}(\rho_{\rm star}) / \Delta \log_{10}(r)$. As with the component decomposition, the stellar slopes are computed in the region $2'' \leq r \leq r_{\rm max}$. In addition, since we are computing the slope of the stellar profile given in Eq. 4.4, the result already contains information on the stellar population variation (as per Eq. 4.6). Figure 4.5 shows the comparison between total and stellar slope distributions. The mean total slope found by this work is $\langle\gamma'\rangle = -2.1295 \pm 0.0161$ with a scatter of $\Delta_{\gamma'} = 0.1690 \pm 0.0168$. The mean stellar slope is found to be $\langle\gamma\rangle = -2.5067 \pm 0.0212$ with a scatter of $\Delta_{\gamma} = 0.2515 \pm 0.0212$. The scatter for these results is computed using the Normalised Median Absolute Deviation (NMAD). The NMAD is defined as

$$\Delta = 1.4826 \times \text{median}(|x_i - \text{median}(\mathbf{x})|) \tag{4.8}$$

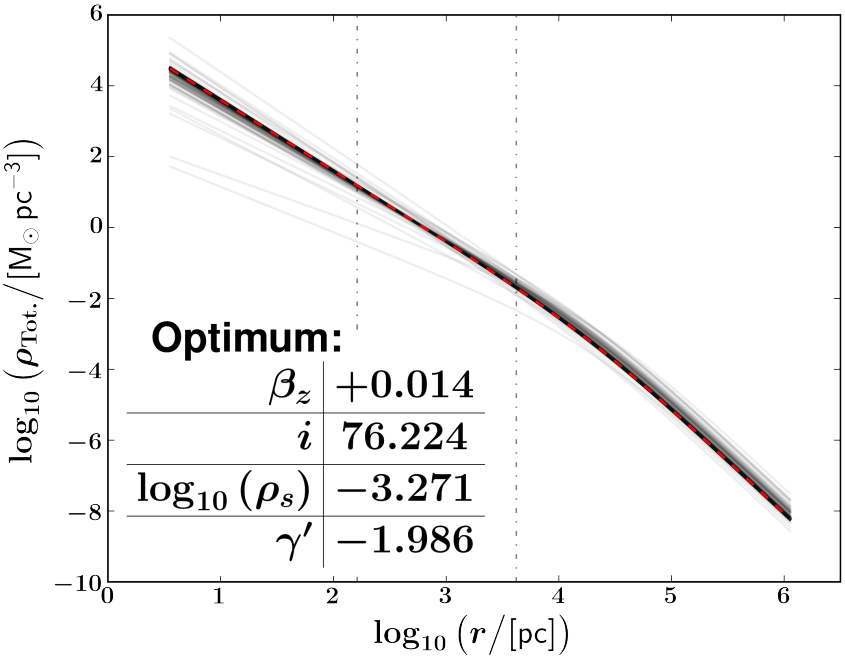

Figure 4.6: 1000 randomly-drawn iterations from a total of 24,000 from the Markov Chain for NGC2685. A very high transparency value is used to emphasise the region with the most curves. The overlaid red curve is produced from the final optimum, given in the inset table. The dashed grey lines represent the region on which all fits are computed, bounded by $2'' \leq r \leq r_{\mathrm{max}}$.

where x_i is a single measurement, and $\mathbf{x}$ is the vector of all measurements. The NMAD is used here to compute the statistical dispersion since it is more robust to outliers compared to, for example, the standard deviation (for example, see Leys et al., 2013; Rousseeuw & Croux, 1993). Errors on both quantities are computed using Monte Carlo methods. A subset of slopes is drawn randomly assuming a uniform distribution, and the mean and NMAD are computed. This is repeated 2000 times, and the dispersion on the set of means and NMADs is given as the error of the mean and NMAD, respectively.

In addition to the corner plots presented in Figures 2.10 and 4.1, another convenient visualisation of Bayesian inference techniques is presented in Figure 4.6 to emphasise the tendency of the total density profiles towards nearly-isothermal slopes. In this type of visualisation, iterations of the Markov Chain are drawn at random, and plotted on the same axes. In this way, the region with the highest density of curves is that which was probed the most by the Monte Carlo walkers (based on the probability of it being selected from the chain from a random draw), indicating that it has a high likelihood. It can be seen that the number of curves increases smoothly, from both above and below, as the slope tends towards isothermal. Furthermore, it is clear from the contrast that the majority of curves are approximately isothermal. These features indicate that optimal slopes of ~ -2 are genuinely favoured over any other slope in the parameter space, and are not statistical artefacts of the MCMC

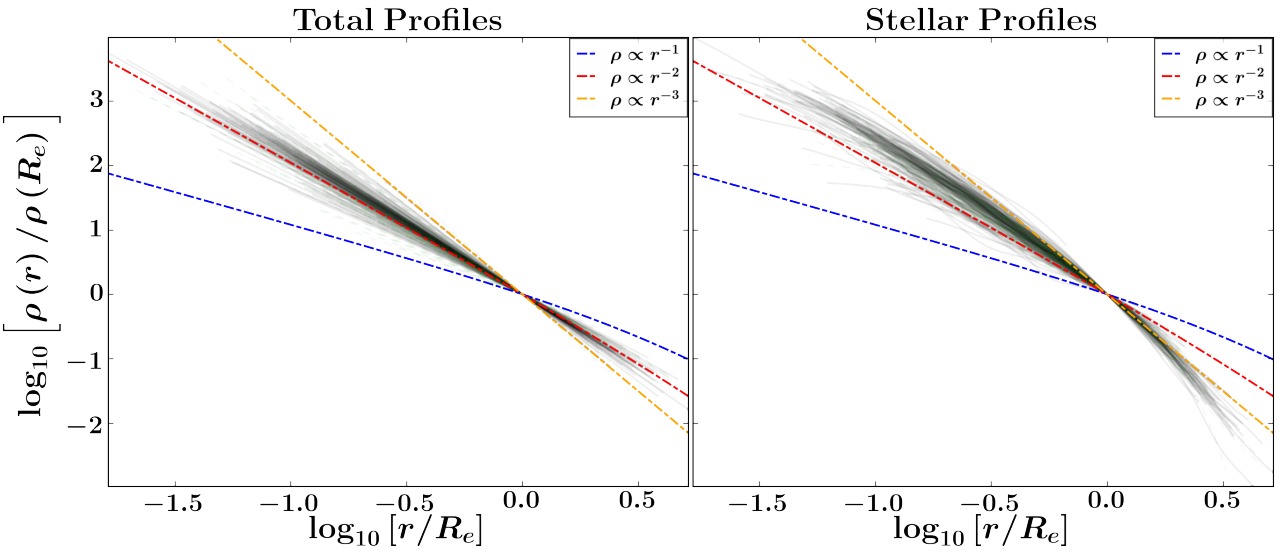

Figure 4.7: The profiles of the full ATLAS^{3D} samples of the total mass-density (left panel) and the stellar mass-density (right panel). All curves are plotted with very high transparency to accentuate the densest regions. Green dashed curves represent galaxies with a data quality of 0.

process.

It is clear that the total mass profiles have a smaller scatter around a nearly-isothermal slope of −2.1, compared to the stellar-only mass profiles. This suggests that the total slope is the more fundamental property, since we observe a strong tendency towards this mean value for all of our galaxies. Despite the significant scatter in the stellar-only slopes, and the 2 orders of magnitude in stellar mass that is spanned by the sample of 258 galaxies, we find remarkably low scatter about this mean value. It thus appears that differences in the stellar densities among galaxies are compensated for by their respective dark matter components in a way that consistently results in a total mass-density profile that is nearly-isothermal. This finding is consistent with the so-called Bulge-Halo Conspiracy.

These results are in very good agreement with previous work. Auger et al. (2010) report $\langle\gamma'\rangle = 2.078 \pm 0.027$ with a scatter of $\Delta_{\gamma'} = 0.16 \pm 0.02$ from gravitational lensing of 73 early-type galaxies, by constructing mass models assuming isotropic (that is, with strictly zero vertical anisotropy) velocity distributions. Cappellari et al. (2015) report $\langle\gamma'\rangle = 2.19 \pm 0.03$ with a scatter of $\Delta_{\gamma'} = 0.11$ from dynamical modelling out to much larger radii, with a sample of 14 early-type galaxies. They also report $\langle\gamma'\rangle = 2.15 \pm 0.03$ with a scatter of $\Delta_{\gamma'} = 0.10$ for $R_e/10 < r < R_e$, which is similar to the range used in this work. To further compare to Cappellari et al. (2015), Figure 4.7 shows both the total and stellar profiles of our sample. The agreement here is excellent. Despite the differences in data

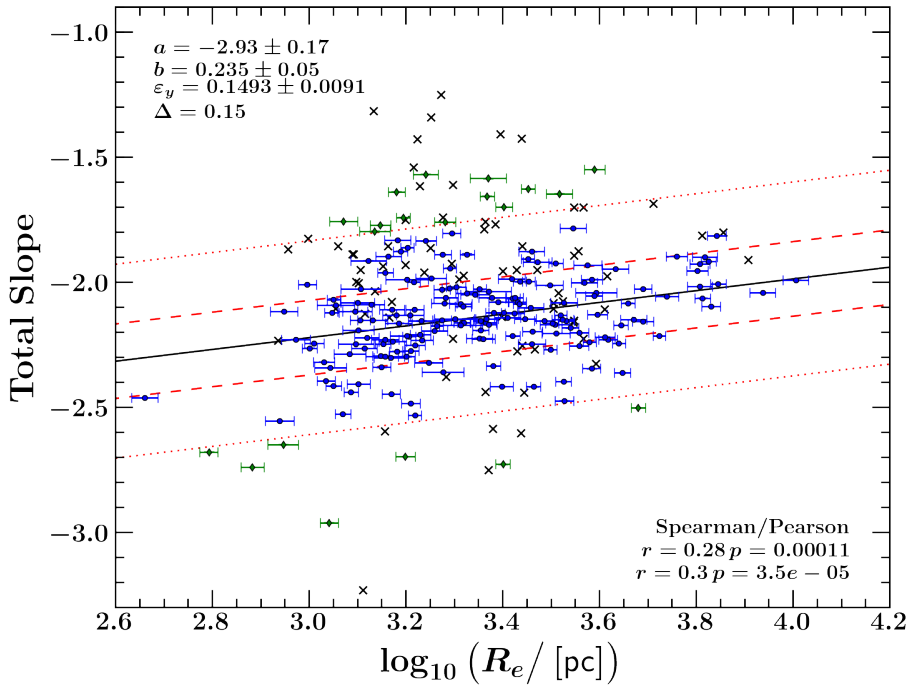

Figure 4.8: The trend of total mass-density profile slope with effective radius. A small correlation is observed, with significant scatter.

range and sample size, the results of both Cappellari et al. (2015) and our work show nearly-isothermal slopes over the full radial range of the total mass profiles. Additionally, it can be seen that the stellar profiles are steeper than isothermal in the central regions, and steepen further to $\rho \propto r^{-3}$ in the outer regions, which is also in very good agreement with Cappellari et al. (2015).

4.2.4 Scaling Relations with γ'

The results of the General Power Law method can be used to further constrain scaling relations of the total mass-density profile slope with galactic observables that have been studied previously. Such relations may illuminate the physical processes behind the so-called Bulge-Halo Conspiracy, as well as its implications for galaxy formation. The correlations constrained here are those of total slope with R_e and σ_e (Cappellari et al., 2015; Dutton & Treu, 2014), presented in Figures 4.8 and 4.9, respectively.

Both figures show weak correlations. Trends with R_e are in qualitative agreement with those of Dutton & Treu (2014). They report that the weakest correlation of total slopes is with velocity dispersion, as is the case in our work also, however the difference in aperture definitions for effective velocity dispersion between our work and Dutton & Treu (2014) prevents direct comparison. Our results also agree qualitatively with those of Auger et al. (2010). Conversely, Cappellari et al. (2015) report no

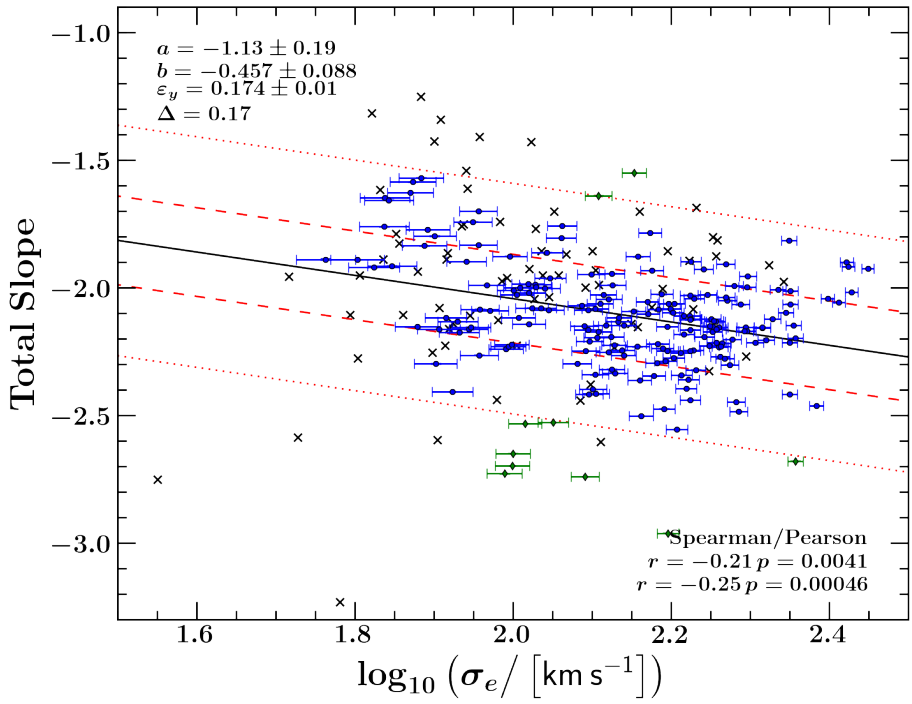

Figure 4.9: The trend of total mass-density profile slope with effective velocity dispersion. A very weak negative correlation is observed, with significant scatter.

correlations for either R_e and σ_e. However, given the weak statistical significance of the results of our work and the large scatter, we can not make strong statements about possible relations between these parameters. Conclusions in this regard will require more robust statistics, likely from an increase in sample size using data from the next generation of IFU projects, including CALIFA (Sánchez et al., 2012), SAMI (Croom et al., 2012), and MaNGA (Bundy et al., 2015). Indeed, the extension of all studies conducted in this work will benefit from the use of such data, and this is a key driver for future work.

5

Discussion & Conclusions

5.1 Methods Comparison

Presented in Figure 5.1 are the data and JAM models for the Scaled Potential and General Power Law methods of every galaxy in the ATLAS^{3D} sample. This figure highlights the fact that differences between the two methods are typically small. Despite the important differences between the methods, JAM ultimately attempts to fit the observed RMS velocity distribution, which is unaltered throughout this work. Furthermore, the features that result in a data quality of 0 (Table A1) are visible, such as the prominent dust lane in NGC5866 and its impact on the subsequent JAM models.

We see also that the models are able to reproduce the kinematics well in general. This is quantified by the reduced χ^2 values in Table A1, which have a median of 4.37 for the full sample. Furthermore, the models are able to match a wide range of kinematic structures, from typical 'lobe' features such as NGC4564, to centrally-concentrated rotation such as NGC5845, and combinations of these features such as NGC4350.

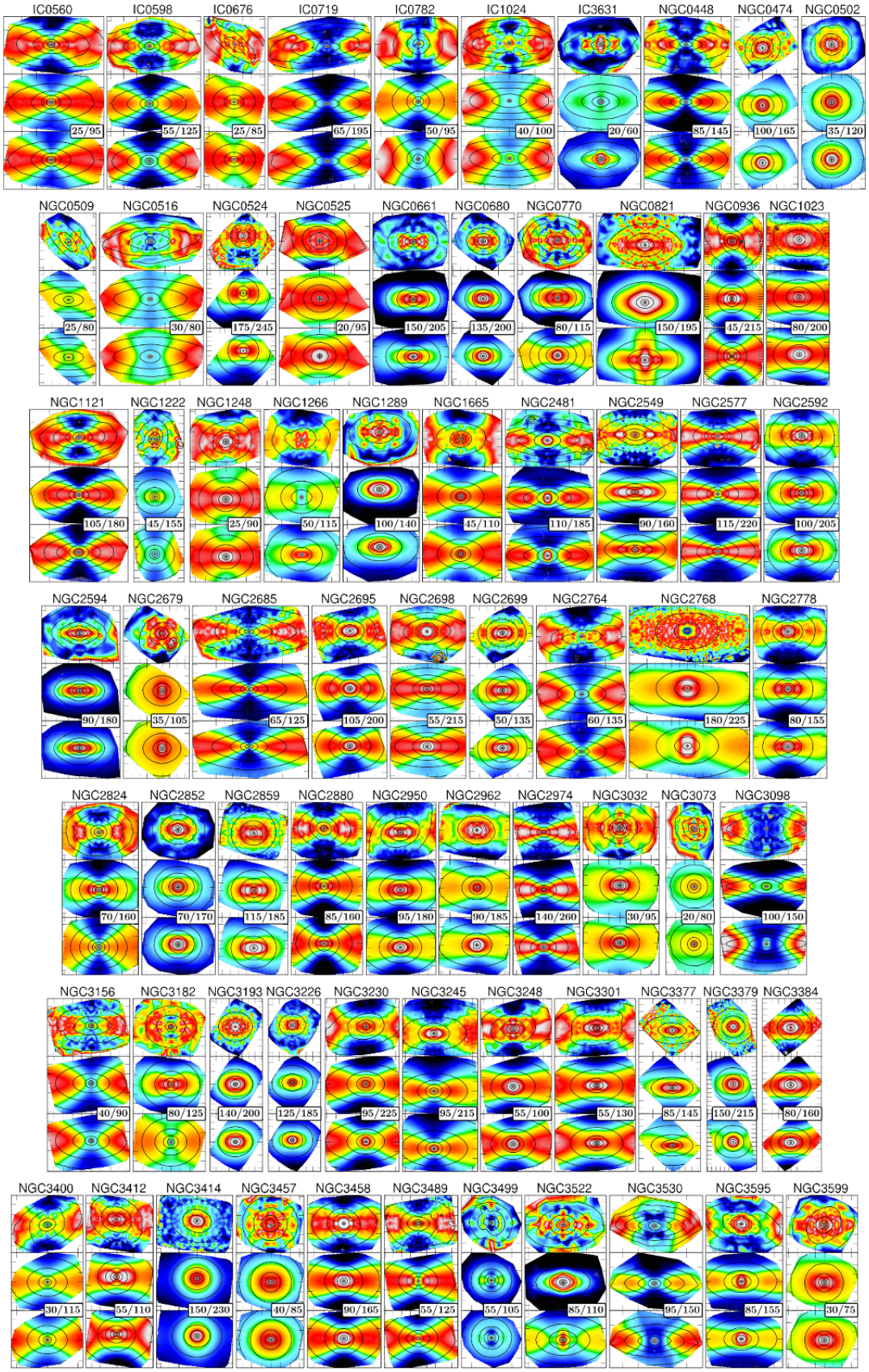
IC0560 IC0598 IC0676 IC0719 IC0782 IC1024 IC3631 NGC0448 NGC0474 NGC0502
25/95 55/125 25/85 65/195 50/95 40/100 20/60 85/145 100/165 35/120
NGC0509 NGC0516 NGC0524 NGC0525 NGC0661 NGC0680 NGC0770 NGC0821 NGC0936 NGC1023
25/80 30/80 175/245 20/95 150/205 135/200 80/115 150/195 45/215 80/200
NGC1121 NGC1222 NGC1248 NGC1266 NGC1289 NGC1665 NGC2481 NGC2549 NGC2577 NGC2592
105/180 45/155 25/90 50/115 100/140 45/110 110/185 90/160 115/220 100/205
NGC2594 NGC2679 NGC2685 NGC2695 NGC2698 NGC2699 NGC2764 NGC2768 NGC2778
90/180 35/105 65/125 105/200 55/215 50/135 60/135 180/225 80/155
NGC2824 NGC2852 NGC2859 NGC2880 NGC2950 NGC2962 NGC2974 NGC3032 NGC3073 NGC3098
70/160 70/170 115/185 85/160 95/180 90/185 140/260 30/95 20/80 100/150
NGC3156 NGC3182 NGC3193 NGC3226 NGC3230 NGC3245 NGC3248 NGC3301 NGC3377 NGC3379 NGC3384
40/90 80/125 140/200 125/185 95/225 95/215 55/100 55/130 85/145 150/215 80/160
NGC3400 NGC3412 NGC3414 NGC3457 NGC3458 NGC3489 NGC3499 NGC3522 NGC3530 NGC3595 NGC3599
30/115 55/110 150/230 40/85 90/165 55/125 55/105 85/110 95/150 85/155 30/75

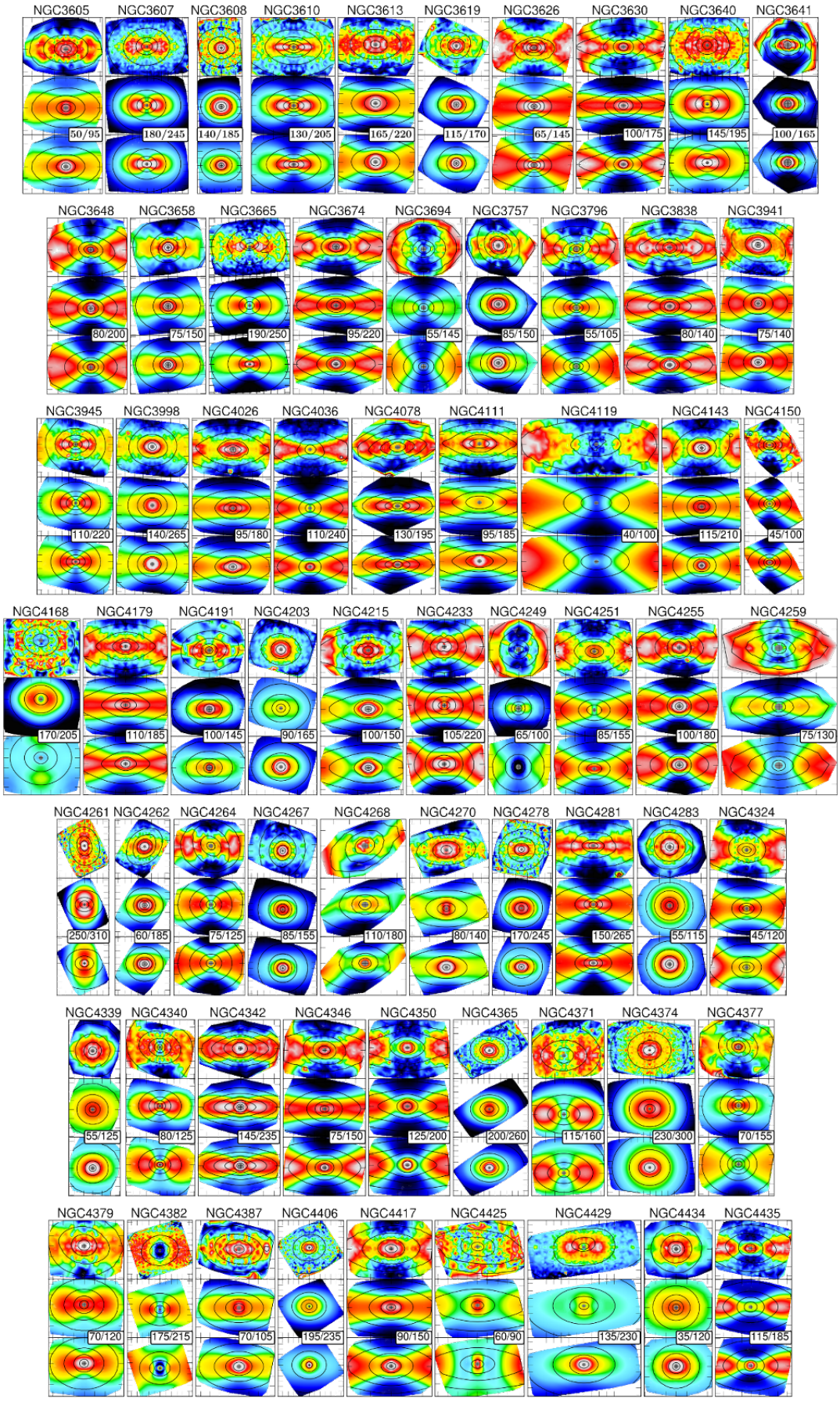
NGC3605 NGC3607 NGC3608 NGC3610 NGC3613 NGC3619 NGC3626 NGC3630 NGC3640 NGC3641
50/95 180/245 140/185 130/205 165/220 115/170 65/145 100/175 145/195 100/165
NGC3648 NGC3658 NGC3665 NGC3674 NGC3694 NGC3757 NGC3796 NGC3838 NGC3941
80/200 75/150 190/250 95/220 55/145 85/150 55/105 80/140 75/140
NGC3945 NGC3998 NGC4026 NGC4036 NGC4078 NGC4111 NGC4119 NGC4143 NGC4150
110/220 140/265 95/180 110/240 130/195 95/185 40/100 115/210 45/100
NGC4168 NGC4179 NGC4191 NGC4203 NGC4215 NGC4233 NGC4249 NGC4251 NGC4255 NGC4259
170/205 110/185 100/145 90/165 100/150 105/220 65/100 85/155 100/180 75/130
NGC4261 NGC4262 NGC4264 NGC4267 NGC4268 NGC4270 NGC4278 NGC4281 NGC4283 NGC4324
250/310 60/185 75/125 85/155 110/180 80/140 170/245 150/265 55/115 45/120
NGC4339 NGC4340 NGC4342 NGC4346 NGC4350 NGC4365 NGC4371 NGC4374 NGC4377
55/125 80/125 145/235 75/150 125/200 200/260 115/160 230/300 70/155
NGC4379 NGC4382 NGC4387 NGC4406 NGC4417 NGC4425 NGC4429 NGC4434 NGC4435
70/120 175/215 70/105 195/235 90/150 60/90 135/230 35/120 115/185

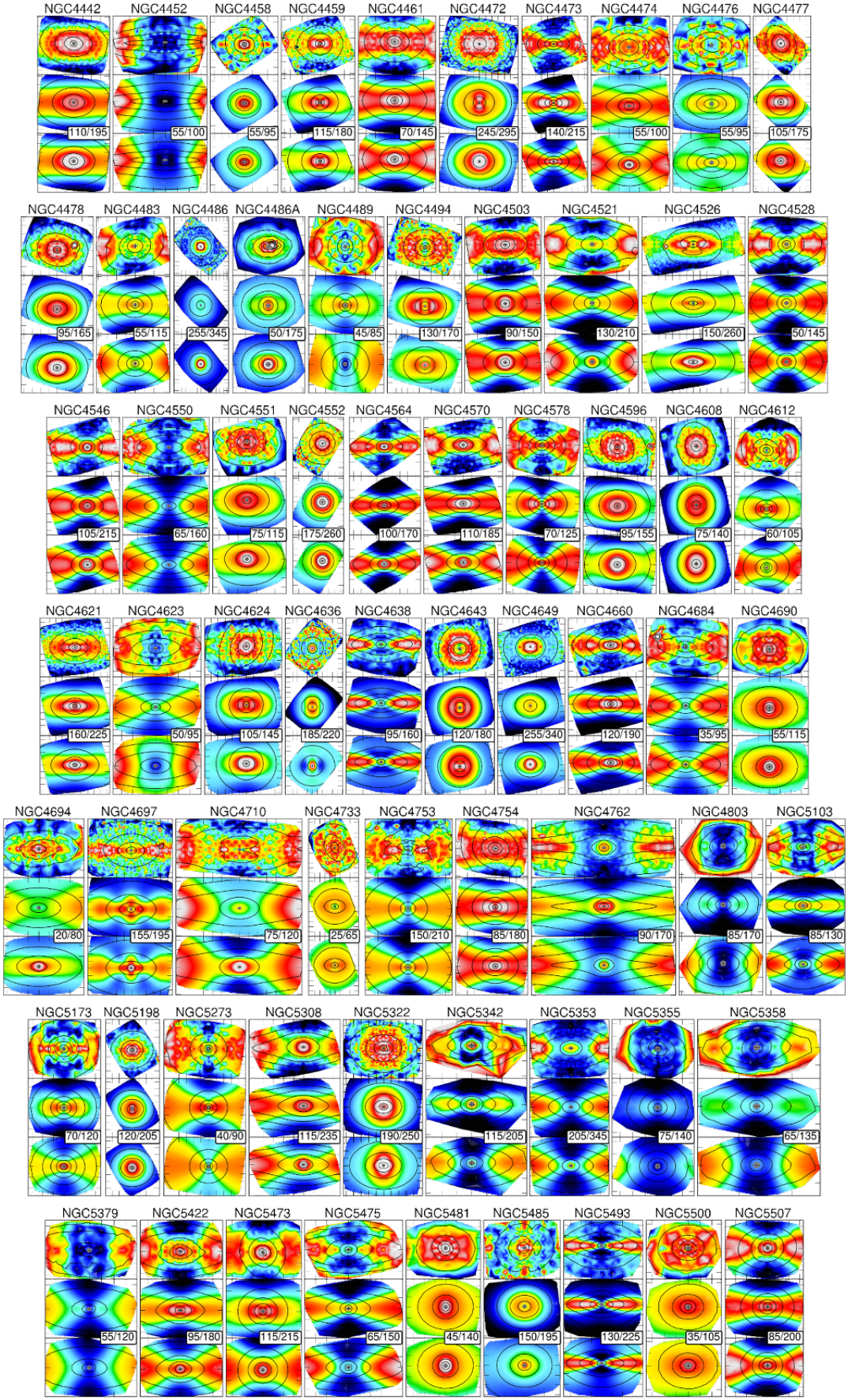
NGC4442 NGC4452 NGC4458 NGC4459 NGC4461 NGC4472 NGC4473 NGC4474 NGC4476 NGC4477
110/195 55/100 55/95 115/180 70/145 245/295 140/215 55/100 55/95 105/175
NGC4478 NGC4483 NGC4486 NGC4486A NGC4489 NGC4494 NGC4503 NGC4521 NGC4526 NGC4528
95/165 55/115 255/345 50/175 45/85 130/170 90/150 130/210 150/260 50/145
NGC4546 NGC4550 NGC4551 NGC4552 NGC4564 NGC4570 NGC4578 NGC4596 NGC4608 NGC4612
105/215 65/160 75/115 175/260 100/170 110/185 70/125 95/155 75/140 60/105
NGC4621 NGC4623 NGC4624 NGC4636 NGC4638 NGC4643 NGC4649 NGC4660 NGC4684 NGC4690
160/225 50/95 105/145 185/220 95/160 120/180 255/340 120/190 35/95 55/115
NGC4694 NGC4697 NGC4710 NGC4733 NGC4753 NGC4754 NGC4762 NGC4803 NGC5103
20/80 155/195 75/120 25/65 150/210 85/180 90/170 85/170 85/130
NGC5173 NGC5198 NGC5273 NGC5308 NGC5322 NGC5342 NGC5353 NGC5355 NGC5358
70/120 120/205 40/90 115/235 190/250 115/205 205/345 75/140 65/135
NGC5379 NGC5422 NGC5473 NGC5475 NGC5481 NGC5485 NGC5493 NGC5500 NGC5507
55/120 95/180 115/215 65/150 45/140 150/195 130/225 35/105 85/200

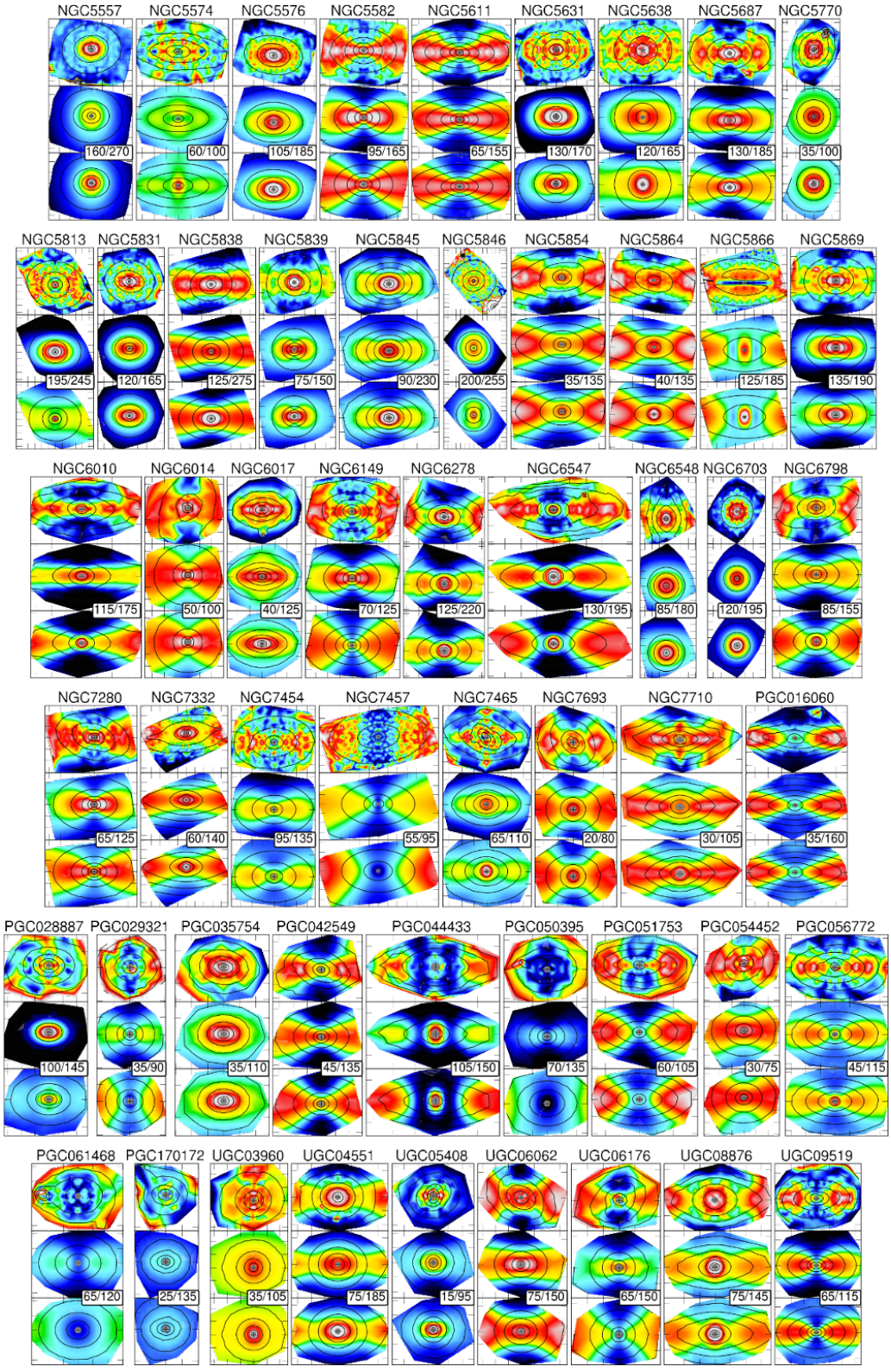

Figure 5.1: Comparison of all observed (and symmetrised) $V_{\rm RMS}$ maps (top row of each set of panels) with the correpsonding JAM model $V_{\rm RMS}$ maps from the Scaled Potential (middle row) and General Power Law (bottom row) methods. The observations have isophote contours overlaid, and the models have the corresponding MGE contours shown. Tick marks are 10 $''$ apart, and the $V_{\rm RMS}$ colour limits are inset. The central 2 $''$, excluded from the JAM model, is masked with the grey ellipse and black cross.

5.2 IMF Variation

This work has provided robust evidence in favour of systematic IMF variation as a function of dynamically-derived galaxy mass from a large sample of early-type galaxies, accounting for dark matter content and spatial variation in age. The implication of this result is that stars of certain mass are more or less likely to form in a particular galaxy based on its total mass. Whereas star formation is typically considered to be a relatively local process, this finding seems to suggest that the star formation process is influenced by the global gravitational potential within which the galaxy resides (however we note the restricted extent of our observations). The determination of the stellar mass in galaxies is further complicated by a variable IMF. As mentioned in § 1.2, the IMF is necessary for the derivation of galaxy mass from the observed light. However, should the IMF depend on galaxy mass, one would need to know the mass a priori in order to determine the most suitable IMF normalisation.

5.3 Galaxies with Strong Hβ Gradients

Without any consideration of the spatial variation in $(M/L)_{\rm Salp}$, the $\alpha_{\rm dyn.}$ parameter is expected to be very high for the strong Hβ gradient galaxies, because young stars contribute significantly to the luminosity of the stellar M/L. That is, the L in $(M/L)_{\rm Salp}$ is increased, reducing $(M/L)_{\rm Salp}$, and subsequently increasing $\alpha_{\rm dyn.}$. Presented in Figure 5.2 are the variations of $\alpha_{\rm dyn.}$ with $(M/L)_{\rm stars}$ for the mass-follows-light, Scaled Potential, and General Power Law methods, *including* those galaxies in the ATLAS$^{\rm 3D}$ sample that are flagged as having strong spatial gradients in Hβ absorption (plotted as star symbols). Indeed, panel **(a)**, which is for the mass-follows-light approach assuming a spatially-constant $(M/L)_{\rm Salp}$, shows exactly this elevation of $\alpha_{\rm dyn.}$, as expected. Panels **(b)** and **(c)** are for the Scaled Potential and General Power Law methods, respectively. It is clear that accounting for the gradients in $(M/L)_{\rm Salp}$ has the effect of reducing $\alpha_{\rm dyn.}$ towards the general galaxy population, which exhibit no strong dust or age variations. This indicates that galaxies with strong $(M/L)_{\rm Salp}$ variation are modelled more consistently (with respect to those without strong variation) in both approaches introduced in this work. Furthermore, it is clear that the General Power Law method offers further improvement on the Scaled Potential results. This may be due to the extra freedom in the mass constraints, and the fact that we avoid any dependence on the extrapolated $(M/L)_{\rm Salp}$ profiles in this approach.

While the $\alpha_{\rm dyn.}$ values of galaxies with strong Hβ gradients are reduced by the two methods used in this work, we observe that they are still slightly elevated. The presence of dust in the photometry has detrimental effects on the MGE model (Davis et al., 2013), which subsequently impacts the inferred M/L. Dust corrections were applied to the r-band photometry from Scott et al. (2013) prior to

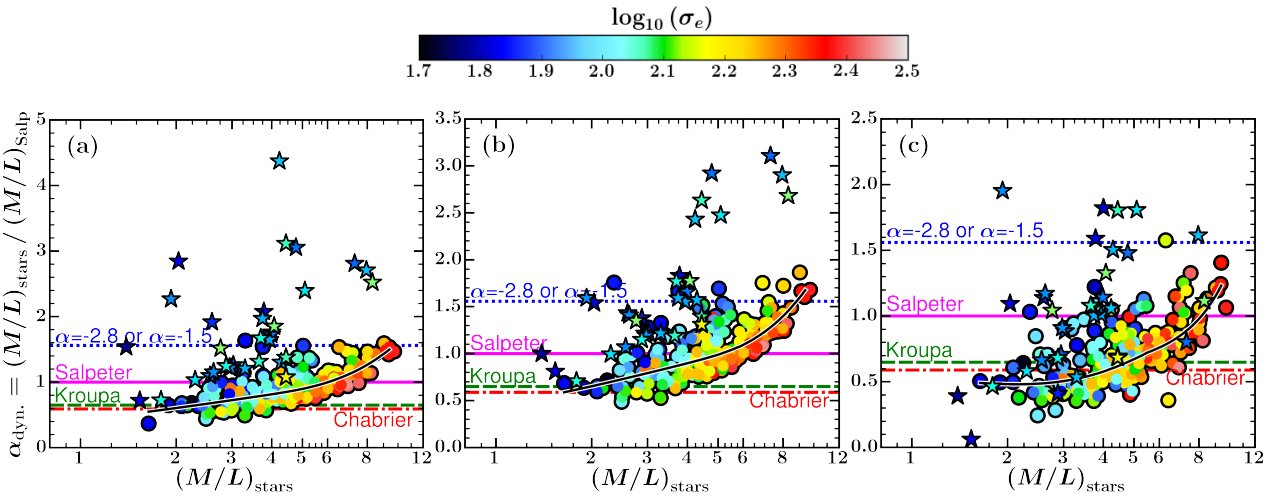

Figure 5.2: The variation in $\alpha_{\rm dyn.}$ with galaxy mass, including galaxies with strong spatial variation in Hβ absorption. Panel **(a)** is for the mass-follows-light method. Panel **(b)** is for the Scaled Potential method. Panel **(c)** is for the General Power Law methods. The round points are the objects which were included in previous sections of this work. The objects which exhibit strong gradients in Hβ are denoted as stars. All points are coloured by effective velocity dispersion.

constructing the MGE. This correction is based on the identification and correction of outlier pixels in a $g-i$ colour map. However, this technique may be inadequate in the presence of strong and extended dust features. Such dust is typical in galaxies exhibiting strong stellar age gradients, as discussed in Davis et al. (2013). The inclusion of photometric and spectroscopic observations at near-infrared wavelengths in future studies would make our techniques much more robust against these detrimental dust effects.

5.4 Mass Profiles and the Bulge-Halo Conspiracy

We have placed very strong constraints on the distribution of total mass-density profile slopes with the modelling conducted in the General Power Law method. The strength of these results arises from a number of factors. Our models are both accurate and general, in that they fit high quality spatially-resolved maps of the stellar kinematics; accurately reproduce a wide variety of surface brightness distributions and isophote shapes; and allow for different orbital anisotropies as a free parameter. Furthermore, our sample is large and volume-limited, and thus representative of the near-by Universe. These results highlight the total mass-density of galaxies as a fundamental property, and support the notion of a 'conspiracy' towards consistent slopes of the total mass density, despite varying stellar density profiles. This conspiracy, suggested previously by earlier work with stronger assumptions, now appears to form a key piece in the puzzle of how dark matter and ordinary matter interact and arrange

themselves in galaxies. Should this conpiracy be further corroborated in future work, it is particularly compelling due the consideration highlighted by Abadi et al. (2010), who state that their models suggest "that the response of the halo does not depend solely on the final mass and radial distribution of baryons in the central galaxy, but also on the mode of their assembly", and yet this tendency towards a slope of -2 still exists. It will be very interesting to see if this conspiracy is reproduced by the next generation of high-resolution numerical simulations, such as EAGLE (Schaye et al., 2015), and if it is sensitive to the detailed baryonic physics and feedback processes included in such simulations.

5.5 Conclusions

This work has undertaken distinct methodologies to constrain the observed variation of the stellar IMF in early-type galaxies. By first treating the dark and luminous matter as co-spatial in Chapter 3, we accounted for stellar population effects by fitting SSP templates to spectra from the ATLAS^{3D} survey and producing dynamical models. The inclusion of stellar population fitting has accounted for subtle variations in age within the population that had yet to be included in such dynamical modelling. The stellar IMF was still seen to vary systematically with galaxy mass, being consistent with a Milky Way-like IMF at lower masses, and with a heavier IMF at the highest masses.

By then considering the dark and luminous matter as spatially separate in Chapter 4, we accounted for stellar population and dark matter effects simultaneously. This further allowed for constraints on the central dark matter content of these galaxies, which is shown to agree well with previous works that did not include such consideration of the stellar population. Once again, the stellar IMF was seen to vary systematically with galaxy mass.

By producing mass profiles of the galaxies in our sample from the modelling results, we constrained the distributions of total and stellar profile slopes. We found that the total slopes show small scatter of $\Delta_{\gamma'} = 0.1690 \pm 0.0168$ about a nearly-isothermal mean slope of $\langle\gamma'\rangle = -2.1295 \pm 0.0161$, while the stellar slope distribution showed steeper slopes ($\langle\gamma\rangle = -2.5067 \pm 0.0212$) and larger scatter $\Delta_{\gamma} = 0.2515 \pm 0.0212$. These results provide strong evidence in favour of the Bulge-Halo Conspiracy. They place constraints on theories and simulations of galaxy formation, which must produce early-type galaxies that are described by approximately-isothermal total mass-density profiles, regardless of their stellar density, stellar population effects, or dark matter density, individually.

These analyses should now be applied to late-type galaxies to constrain foremost the universality of

the IMF. While variations with galaxy mass were constrained in this work, it would be interesting to investigate possible variations with galaxy type. The inclusion of both star-forming early-type galaxies and (likely star-forming) late-type galaxies would provide much more general conclusions on the nature of the IMF, in addition to improving the statistical significance of the trends that were investigated. We included similar objects, which highlighted that difficulties introduced by dust at optical wavelengths, and the advantages that near-IR observations would provide (for example, see Norris et al., 2014). Should these galaxies also show similar trends with total mass-density slope, it would allude to some fundamental facet of galaxy formation that enforces this tendency towards $\gamma' = -2.1$.

The results found here are one of the first to simultaneously constrain stellar populations effects, dark matter content, and total mass-density scaling relations on a sample of this size. Progress has already been made, however, with the conception of broader IFU surveys, including CALIFA (Sánchez et al., 2012), SAMI (Croom et al., 2012), and MaNGA (Bundy et al., 2015), making use of larger IFUs, such as MUSE (Bacon et al., 2010) and KOALA (Ellis et al., 2012). The size and diversity of the galaxy samples resulting from these works will make it possible to reach stronger statistical conclusions concerning the nature of the IMF, the distribution of dark matter within these galaxies, and the significance of the total mass-density profile as a fundamental galactic property.

References

Abadi M. G., Navarro J. F., Fardal M., Babul A., Steinmetz M., 2010, MNRAS, 407, 435

Agertz O., Teyssier R., Moore B., 2011, MNRAS, 410, 1391

Auger M. W., Treu T., Bolton A. S., Gavazzi R., Koopmans L. V. E., Marshall P. J., Moustakas L. A., Burles S., 2010, The Astrophysical Journal, 724, 511

Bacon R., et al., 2001, Monthly Notices of the Royal Astronomical Society, 326, 23

Bacon R., et al., 2010, in Society of Photo-Optical Instrumentation Engineers (SPIE) Conference Series. p. 8, doi:10.1117/12.856027

Barnabè M., et al., 2012, MNRAS, 423, 1073

Bastian N., Covey K. R., Meyer M. R., 2010, Annual Review of Astronomy and Astrophysics, 48, 339

Begeman K. G., Broeils A. H., Sanders R. H., 1991, MNRAS, 249, 523

Bolton A. S., Burles S., Koopmans L. V. E., Treu T., Moustakas L. A., 2006, The Astrophysical Journal, 638, 703

Boylan-Kolchin M., Springel V., White S. D. M., Jenkins A., Lemson G., 2009, MNRAS, 398, 1150

Bundy K., et al., 2015, ApJ, 798, 7

Cappellari M., 2002, Monthly Notices of the Royal Astronomical Society, 333, 400

Cappellari M., 2008, Monthly Notices of the Royal Astronomical Society, 390, 71

Cappellari M., Emsellem E., 2004, The Publications of the Astronomical Society of the Pacific, 116, 138

Cappellari M., et al., 2006, Monthly Notices of the Royal Astronomical Society, 366, 1126

Cappellari M., et al., 2011, Monthly Notices of the Royal Astronomical Society, 413, 813

Cappellari M., et al., 2012, Nature, 484, 485

Cappellari M., et al., 2013a, Monthly Notices of the Royal Astronomical Society, 432, 1709

Cappellari M., et al., 2013b, Monthly Notices of the Royal Astronomical Society, 432, 1862

Cappellari M., et al., 2015, The Astrophysical Journal Letters, 804, L21

Chabrier G., 2003, ApJ, 586, L133

Cleveland W. S., 1979, Journal of the American statistical association, 74, 829

Conroy C., van Dokkum P., 2012, The Astrophysical Journal, 747, 69

Croom S. M., et al., 2012, MNRAS, 421, 872

Davis T. A., et al., 2013, MNRAS, 429, 534

Dutton A. A., Treu T., 2014, Monthly Notices of the Royal Astronomical Society, 438, 3594

Eisenhauer F., 2001, in Tacconi L., Lutz D., eds, Starburst Galaxies: Near and Far. p. 24 (arXiv:astro-ph/0101321)

Ellis S. C., et al., 2012, in Society of Photo-Optical Instrumentation Engineers (SPIE) Conference Series. p. 0, doi:10.1117/12.925812

Emsellem E., Monnet G., Bacon R., 1994, A&A, 285, 723

Ferrarese L., Merritt D., 2000, The Astrophysical Journal Letters, 539, L9

Fonnesbeck C., Patil A., Huard D., Salvatier J., 2015, PyMC: Bayesian Stochastic Modelling in Python, Astrophysics Source Code Library (ascl:1506.005)

Forbes D. A., Spitler L. R., Strader J., Romanowsky A. J., Brodie J. P., Foster C., 2011, Monthly Notices of the Royal Astronomical Society, 413, 2943

Foreman-Mackey D., Hogg D. W., Lang D., Goodman J., 2013, PASP, 125, 306

Gnedin O. Y., Kravtsov A. V., Klypin A. A., Nagai D., 2004, ApJ, 616, 16

Hastings W. K., 1970, Biometrika, 57, 97

Hubble E., 1929, Proceedings of the National Academy of Science, 15, 168

Hubble E. P., 1936, Realm of the Nebulae. Yale University Press

Ishiyama T., et al., 2013, ApJ, 767, 146

Koopmans L. V. E., et al., 2009, ApJ, 703, L51

Krajnović D., et al., 2011, Monthly Notices of the Royal Astronomical Society, 414, 2923

Kroupa P., 2001, Monthly Notices of the Royal Astronomical Society, 322, 231

Kroupa P., 2002, Science, 295, 82

Kuntschner H., et al., 2010, MNRAS, 408, 97

Kuzio de Naray R., McGaugh S. S., de Blok W. J. G., 2008, ApJ, 676, 920

La Barbera F., Ferreras I., de Carvalho R. R., Bruzual G., Charlot S., Pasquali A., Merlin E., 2012, MNRAS, 426, 2300

La Barbera F., Ferreras I., Vazdekis A., de la Rosa I. G., de Carvalho R. R., Trevisan M., Falcón-Barroso J., Ricciardelli E., 2013, MNRAS, 433, 3017

Lada C. J., 2006, The Astrophysical Journal Letters, 640, L63

Leys C., Ley C., Klein O., Bernard P., Licata L., 2013, Journal of Experimental Social Psychology, 49, 764

Martig M., Bournaud F., 2010, ApJ, 714, L275

Martig M., Bournaud F., Croton D. J., Dekel A., Teyssier R., 2012, ApJ, 756, 26

Martín-Navarro I., et al., 2015, ApJ, 806, L31

McDermid R. M., et al., 2015, MNRAS, 448, 3484

Miller G. E., Scalo J. M., 1979, Astrophysical Journal Supplement Series, 41, 513

Momjian E., Carilli C. L., Walter F., Venemans B., 2014, AJ, 147, 6

Monnet G., Bacon R., Emsellem E., 1992, Astronomy and Astrophysics, 253, 366

Moster B. P., Somerville R. S., Maulbetsch C., van den Bosch F. C., Macciò A. V., Naab T., Oser L., 2010, ApJ, 710, 903

Navarro J. F., Frenk C. S., White S. D. M., 1996, ApJ, 462, 563

Navarro J. F., et al., 2004, MNRAS, 349, 1039

Norris M. A., Meidt S., Van de Ven G., Schinnerer E., Groves B., Querejeta M., 2014, ApJ, 797, 55

Oh S.-H., de Blok W. J. G., Walter F., Brinks E., Kennicutt Jr. R. C., 2008, AJ, 136, 2761

Oh S.-H., de Blok W. J. G., Brinks E., Walter F., Kennicutt Jr. R. C., 2011, AJ, 141, 193

Peacock J. A., et al., 2001, Nature, 410, 169

Peacock M. B., Zepf S. E., Maccarone T. J., Kundu A., Gonzalez A. H., Lehmer B. D., Maraston C., 2014, The Astrophysical Journal, 784, 162

Rousseeuw P. J., Croux C., 1993, Journal of the American Statistical Association, 88, 1273

Rubin V. C., Ford Jr. W. K., 1970, The Astrophysical Journal, 159, 379

Salpeter E. E., 1955, Astrophysical Journal, 121, 161

Sánchez S. F., et al., 2012, A&A, 538, A8

Sandberg O., 2007, Markov Chain Properties, http://www.math.chalmers.se/Stat/Grundutb/Chalmers/TMS081/oldpage/Lecture_notes/lecture3.pdf

Schaye J., et al., 2015, MNRAS, 446, 521

Schilbach E., Röser S., 2008, Astronomy and Astrophysics, 489, 105

Scott N., et al., 2013, Monthly Notices of the Royal Astronomical Society, 432, 1894

Shanahan R. L., Gieles M., 2015, Monthly Notices of the Royal Astronomical Society: Letters, 448, L94

Spiniello C. c., Trager S., Koopmans L., Conroy C., 2014, Monthly Notices of the Royal Astronomical Society, 438, 1483

Springel V., et al., 2005, nature, 435, 629

Steinmetz M., Navarro J. F., 2002, New Astronomy, 7, 155

Strader J., Smith G. H., Larsen S., Brodie J. P., Huchra J. P., 2009, AJ, 138, 547

Ueda J., et al., 2014, The Astrophysical Journal Supplement, 214, 1

Vazdekis A., Ricciardelli E., Cenarro A. J., Rivero-González J. G., Díaz-García L. A., Falcón-Barroso J., 2012, MNRAS, 424, 157

Weidner C., Ferreras I., Vazdekis A., La Barbera F., 2013, MNRAS, 435, 2274

White S. D. M., Rees M. J., 1978, Monthly Notices of the Royal Astronomical Society, 183, 341

Wilkins S. M., Trentham N., Hopkins A. M., 2008, MNRAS, 385, 687

Wyithe J. S. B., Turner E. L., Spergel D. N., 2001, ApJ, 555, 504

Wyse R. F. G., 1997, The Astrophysical Journal Letters, 490, L69

Zhao H., 1996, MNRAS, 278, 488

de Souza R. S., Ishida E. E. O., Whalen D. J., Johnson J. L., Ferrara A., 2014, MNRAS, 442, 1640

van Dokkum P. G., 2008, ApJ, 674, 29

van Dokkum P. G., Conroy C., 2010, Nature, 468, 940

van Dokkum P. G., Conroy C., 2012, ApJ, 760, 70

Parameter Table

Name	β_z	i	$\log_{10}(\rho_s)$	γ'	$\hat{\chi}^2$	$\alpha_{\mathrm{dyn.}}$	$\log_{10}(\rho_{\mathrm{DM},s})$	M/L_{stars}	$f_{\mathrm{DM}}(R_e)$	Hβ	Quality	r_{max}/R_e
(1)	(2)	(3)	(4)	(5)	(6)	(7)	(8)	(9)	(10)	(11)	(12)	(13)
IC0560	−0.499	72.790	−3.749	−2.160	6.444	0.896	−3.381	3.030	0.13	0	2	1.713
IC0598	+0.360	73.186	−3.128	−1.879	6.675	0.685	−2.821	2.877	0.21	0	2	2.986
IC0676	−0.419	59.068	−3.469	−1.949	12.501	1.581	−3.700	3.781	0.09	0	0	1.063
IC0719	+0.500	76.102	−2.594	−1.641	8.949	1.116	−2.331	8.310	0.35	0	3	3.553
IC0782	−0.201	71.504	−3.001	−1.629	8.090	0.869	−2.744	5.028	0.52	1	1	1.207
IC1024	+0.495	77.908	−3.193	−1.776	15.151	1.472	−2.934	4.772	0.23	0	2	3.245
IC3631	+0.477	70.335	−5.182	−2.746	10.694	0.099	−4.832	0.738	0.02	0	0	2.413
NGC0448	+0.217	81.284	−3.095	−1.962	4.219	0.389	−2.664	3.378	0.20	1	2	3.841
NGC0474	−0.004	89.770	−3.367	−2.363	5.452	0.516	−3.098	4.081	0.16	1	1	0.993
NGC0502	−0.070	63.135	−4.344	−2.715	6.921	0.276	−4.287	2.828	0.01	1	1	1.281
NGC0509	+0.442	81.144	−3.457	−1.790	12.640	0.886	−3.295	3.751	0.25	1	0	3.278
NGC0516	+0.333	81.203	−3.306	−1.644	11.851	0.469	−3.096	3.400	0.40	1	2	2.291
NGC0524	−0.498	39.519	−2.482	−1.971	2.944	0.961	−2.791	6.621	0.09	1	0	1.237
NGC0525	−0.052	69.757	−3.836	−2.301	8.963	0.759	−3.252	4.907	0.11	1	1	1.622
NGC0661	+0.084	89.530	−2.883	−2.118	2.733	1.201	−2.424	9.036	0.23	1	1	1.526
NGC0680	+0.015	89.716	−3.048	−2.272	3.895	0.655	−2.618	5.625	0.19	1	1	1.401
NGC0770	+0.250	63.752	−3.097	−1.951	6.170	0.432	−2.585	3.337	0.23	1	0	2.434
NGC0821	+0.500	62.138	−2.889	−2.124	2.741	0.789	−2.531	6.377	0.29	1	2	1.036
NGC0936	−0.500	36.926	−2.453	−1.900	8.600	0.724	−2.314	5.226	0.37	1	2	1.392
NGC1023	+0.082	74.196	−3.281	−2.360	4.827	0.428	−3.883	3.297	0.01	1	3	1.296

Name	β_z	i	$\log_{10}(\rho_s)$	γ'	$\hat{\chi}^2$	$\alpha_{\rm dyn.}$	$\log_{10}(\rho_{{\rm DM},s})$	$M/L_{\rm stars}$	$f_{\rm DM}(R_e)$	Hβ	Quality	$r_{\rm max}/R_e$
(1)	(2)	(3)	(4)	(5)	(6)	(7)	(8)	(9)	(10)	(11)	(12)	(13)
NGC1121	+0.055	78.013	−3.046	−2.124	5.394	0.794	−2.471	6.647	0.13	1	2	3.379
NGC1222	+0.500	33.053	−2.238	−1.364	48.364	1.017	−2.014	4.233	0.79	0	0	1.449
NGC1248	+0.228	42.843	−3.576	−2.175	5.898	0.553	−3.305	2.085	0.11	1	2	1.549
NGC1266	−0.235	89.682	−3.697	−2.255	10.343	1.135	−6.286	3.987	0.00	0	0	1.157
NGC1289	+0.220	89.678	−3.241	−2.155	5.729	0.860	−2.894	4.177	0.22	1	1	1.556
NGC1665	+0.292	59.742	−3.375	−2.076	6.243	0.901	−3.614	3.175	0.09	1	1	1.410
NGC2481	+0.343	80.264	−3.191	−2.248	6.909	0.562	−2.682	5.044	0.10	1	2	3.789
NGC2549	+0.247	81.321	−3.108	−2.090	6.812	0.825	−2.368	6.036	0.22	1	3	2.177
NGC2577	−0.033	69.720	−2.941	−2.165	3.180	0.881	−2.510	7.687	0.18	1	3	1.793
NGC2592	−0.334	87.814	−3.457	−2.446	5.291	0.814	−2.877	7.197	0.06	1	1	1.892
NGC2594	+0.027	89.191	−3.593	−2.418	8.694	0.752	−2.991	5.328	0.05	1	1	4.129
NGC2679	+0.159	89.635	−3.629	−2.229	28.331	0.971	−3.710	3.478	0.08	1	0	1.114
NGC2685	+0.014	76.224	−3.271	−1.986	5.405	0.464	−2.817	2.930	0.24	1	3	2.340
NGC2695	+0.289	48.455	−2.973	−2.215	4.914	0.746	−2.603	5.458	0.16	1	2	1.765
NGC2698	−0.022	74.045	−3.432	−2.483	20.016	0.560	−2.901	5.215	0.05	1	3	2.722
NGC2699	−0.015	37.113	−3.519	−2.352	6.368	0.562	−2.909	3.856	0.09	1	1	2.134
NGC2764	+0.166	71.923	−3.149	−1.952	9.936	1.804	−3.150	4.438	0.14	0	2	2.173
NGC2768	+0.330	89.959	−2.538	−1.955	2.645	1.133	−2.850	8.482	0.13	1	1	0.893
NGC2778	+0.500	41.237	−3.282	−2.256	3.577	1.243	−2.824	7.154	0.10	1	2	1.414
NGC2824	−0.500	89.926	−2.953	−1.935	9.600	1.319	−2.544	4.074	0.23	0	0	2.475

Name	β_z	i	$\log_{10}(\rho_s)$	γ'	$\hat{\chi}^2$	$\alpha_{\rm dyn.}$	$\log_{10}(\rho_{{\rm DM},s})$	$M/L_{\rm stars}$	$f_{\rm DM}(R_e)$	Hβ	Quality	$r_{\rm max}/R_e$
(1)	(2)	(3)	(4)	(5)	(6)	(7)	(8)	(9)	(10)	(11)	(12)	(13)
NGC2852	−0.111	89.633	−4.365	−2.841	9.325	0.469	−3.691	6.407	0.01	1	1	2.403
NGC2859	−0.113	89.882	−3.123	−2.264	3.250	0.406	−2.632	3.655	0.27	1	2	0.953
NGC2880	−0.422	55.449	−3.001	−2.047	4.500	0.758	−2.472	4.686	0.29	1	1	1.268
NGC2950	+0.130	55.458	−3.296	−2.287	4.053	0.621	−2.450	3.924	0.15	1	1	1.601
NGC2962	−0.043	75.826	−3.474	−2.501	5.340	0.697	−5.572	6.162	0.00	1	1	1.063
NGC2974	+0.424	57.342	−2.722	−2.149	2.621	1.407	−2.421	9.396	0.17	1	3	1.496
NGC3032	+0.051	34.444	−3.673	−2.224	10.746	2.184	−3.216	1.929	0.14	0	0	1.062
NGC3073	−0.042	84.709	−3.873	−2.109	20.763	1.091	−3.400	2.036	0.32	0	0	0.972
NGC3098	+0.380	89.972	−2.840	−1.851	3.360	0.583	−2.432	5.029	0.22	1	0	4.588
NGC3156	+0.500	64.381	−3.248	−1.765	10.110	1.131	−3.232	2.595	0.17	0	1	1.928
NGC3182	+0.157	46.309	−2.775	−1.708	6.887	0.690	−2.501	3.857	0.53	1	0	1.012
NGC3193	+0.030	87.540	−2.905	−2.172	2.457	0.482	−2.717	3.668	0.20	1	2	0.944
NGC3226	+0.005	88.568	−3.154	−2.221	3.980	1.195	−4.958	7.290	0.00	1	2	0.743
NGC3230	+0.249	68.396	−2.852	−2.132	4.637	0.727	−2.665	5.887	0.16	1	2	1.832
NGC3245	+0.012	65.642	−3.108	−2.228	5.586	0.549	−2.672	4.351	0.15	1	3	1.547
NGC3248	+0.305	59.805	−3.524	−2.166	4.542	0.609	−2.979	2.992	0.24	1	2	1.363
NGC3301	+0.213	75.280	−3.259	−2.095	4.051	0.703	−2.977	2.535	0.14	1	3	1.606
NGC3377	+0.211	89.935	−3.371	−2.174	7.323	0.528	−2.697	3.782	0.28	1	1	1.249
NGC3379	+0.268	36.365	−2.637	−2.040	2.042	0.683	−2.042	5.131	0.37	1	3	0.862
NGC3384	+0.213	61.962	−3.115	−2.148	1.912	0.407	−2.320	2.990	0.38	1	3	0.914

Name	β_z	i	$\log_{10}(\rho_s)$	γ'	$\hat{\chi}^2$	$\alpha_{\rm dyn.}$	$\log_{10}(\rho_{{\rm DM},s})$	$M/L_{\rm stars}$	$f_{\rm DM}(R_e)$	Hβ	Quality	$r_{\rm max}/R_e$
(1)	(2)	(3)	(4)	(5)	(6)	(7)	(8)	(9)	(10)	(11)	(12)	(13)
NGC3400	+0.222	57.394	−3.153	−1.835	7.279	0.945	−2.845	4.249	0.26	1	2	1.631
NGC3412	−0.077	58.431	−3.187	−1.989	3.136	0.465	−2.438	2.513	0.43	1	1	1.028
NGC3414	+0.116	82.144	−2.924	−2.200	3.482	0.791	−2.695	6.113	0.17	1	1	0.898
NGC3457	−0.051	80.676	−3.664	−2.112	8.024	0.465	−3.151	2.081	0.12	1	0	1.735
NGC3458	−0.129	56.208	−3.261	−2.305	4.168	0.602	−2.705	4.509	0.09	1	2	2.218
NGC3489	−0.239	61.995	−3.235	−2.026	4.112	0.455	−2.525	1.793	0.29	0	2	1.328
NGC3499	−0.248	26.752	−3.406	−2.032	12.234	0.668	−2.757	2.782	0.19	1	0	2.302
NGC3522	+0.319	89.559	−3.202	−1.972	5.229	0.799	−2.671	5.015	0.30	1	0	1.795
NGC3530	+0.370	84.455	−2.928	−1.874	3.440	0.680	−2.437	5.213	0.20	1	0	4.382
NGC3595	+0.381	66.865	−3.451	−2.338	6.714	0.490	−3.107	3.898	0.10	1	1	1.812
NGC3599	−0.497	39.882	−4.012	−2.278	5.797	0.487	−3.500	1.892	0.19	1	0	0.766
NGC3605	+0.273	66.532	−3.966	−2.356	4.771	0.518	−3.299	2.874	0.09	1	1	1.826
NGC3607	+0.309	44.569	−2.694	−2.154	1.957	0.653	−2.492	4.837	0.23	1	2	0.777
NGC3608	+0.101	87.297	−2.896	−2.083	3.997	0.632	−2.533	5.181	0.27	1	0	0.980
NGC3610	+0.008	89.749	−3.115	−2.230	6.144	0.539	−2.468	3.173	0.18	1	3	1.702
NGC3613	+0.235	89.396	−2.788	−2.148	2.393	0.691	−2.540	5.873	0.19	1	2	1.422
NGC3619	+0.008	41.452	−3.152	−2.232	5.071	0.853	−2.751	4.899	0.27	1	1	0.756
NGC3626	−0.263	70.482	−3.260	−2.151	6.265	1.041	−2.773	2.762	0.22	0	1	1.345
NGC3630	+0.026	82.486	−3.079	−2.155	3.844	0.491	−2.437	4.662	0.16	1	3	2.562
NGC3640	−0.000	89.970	−2.743	−2.023	3.487	0.540	−2.536	4.016	0.31	1	2	0.875

Name	β_z	i	$\log_{10}(\rho_s)$	γ'	$\hat{\chi}^2$	$\alpha_{\rm dyn.}$	$\log_{10}(\rho_{{\rm DM},s})$	$M/L_{\rm stars}$	$f_{\rm DM}(R_e)$	Hβ	Quality	$r_{\rm max}/R_e$
(1)	(2)	(3)	(4)	(5)	(6)	(7)	(8)	(9)	(10)	(11)	(12)	(13)
NGC3641	−0.474	27.706	−3.368	−2.322	7.072	1.199	−2.454	6.285	0.20	1	0	1.159
NGC3648	+0.389	58.171	−2.826	−2.031	4.402	0.823	−2.350	6.902	0.24	1	2	2.098
NGC3658	+0.166	41.759	−3.505	−2.395	4.173	0.655	−3.600	3.696	0.04	1	3	1.168
NGC3665	−0.079	88.347	−2.532	−2.005	3.286	0.840	−2.651	6.267	0.20	1	2	0.798
NGC3674	+0.182	75.932	−3.087	−2.276	3.310	0.709	−2.507	7.000	0.11	1	2	2.428
NGC3694	+0.366	43.811	−2.552	−1.525	10.925	0.602	−2.226	3.298	0.58	0	0	1.855
NGC3757	+0.326	35.137	−3.208	−2.237	5.946	0.839	−2.350	4.828	0.13	1	0	2.391
NGC3796	+0.500	56.389	−3.190	−1.891	6.182	0.882	−2.677	2.970	0.27	0	0	2.112
NGC3838	+0.188	78.685	−3.529	−2.317	5.314	0.469	−2.780	3.817	0.09	1	2	2.827
NGC3941	+0.215	58.680	−3.528	−2.298	2.784	0.438	−2.944	2.495	0.10	1	1	1.280
NGC3945	−0.401	88.372	−2.914	−2.148	5.373	0.513	−2.508	4.268	0.26	1	1	1.155
NGC3998	+0.499	38.088	−2.719	−2.210	2.180	1.243	−1.909	9.347	0.26	1	2	1.042
NGC4026	+0.132	83.063	−3.250	−2.250	3.394	0.565	−2.623	4.705	0.11	1	2	1.802
NGC4036	−0.095	74.979	−2.861	−2.154	4.650	0.627	−2.803	5.057	0.11	1	2	1.687
NGC4078	+0.231	89.836	−3.090	−2.218	7.111	0.863	−2.649	7.357	0.11	1	1	3.908
NGC4111	+0.306	88.580	−3.394	−2.345	3.683	0.681	−2.926	4.439	0.05	0	2	2.973
NGC4119	+0.277	71.689	−3.136	−1.645	6.836	0.777	−3.071	3.304	0.35	1	3	1.257
NGC4143	+0.185	64.607	−2.975	−2.153	3.538	0.659	−2.343	5.665	0.17	1	1	1.566
NGC4150	−0.156	53.734	−3.545	−2.108	5.305	1.174	−3.375	2.626	0.06	0	3	1.704
NGC4168	+0.117	72.676	−2.365	−1.682	2.574	0.973	−2.242	8.019	0.48	1	0	0.761

Name	β_z	i	$\log_{10}(\rho_s)$	γ'	$\hat{\chi}^2$	$\alpha_{\rm dyn.}$	$\log_{10}(\rho_{{\rm DM},s})$	$M/L_{\rm stars}$	$f_{\rm DM}(R_e)$	Hβ	Quality	$r_{\rm max}/R_e$
(1)	(2)	(3)	(4)	(5)	(6)	(7)	(8)	(9)	(10)	(11)	(12)	(13)
NGC4179	+0.155	83.888	−3.022	−2.160	2.693	0.645	−2.466	5.918	0.16	1	3	1.944
NGC4191	+0.115	88.640	−3.140	−2.091	4.541	0.763	−2.804	4.453	0.21	1	1	1.627
NGC4203	+0.025	89.650	−3.951	−2.598	3.594	0.347	−5.472	3.291	0.00	1	0	0.634
NGC4215	+0.283	89.860	−3.223	−2.195	5.085	0.585	−3.007	4.021	0.10	1	2	2.440
NGC4233	−0.156	67.463	−2.698	−2.068	6.790	0.787	−2.257	6.686	0.28	1	2	1.315
NGC4249	−0.191	88.427	−2.842	−1.466	7.796	0.414	−2.580	3.846	0.72	1	0	1.103
NGC4251	−0.004	80.009	−3.098	−2.062	3.443	0.341	−2.563	2.560	0.26	1	1	1.675
NGC4255	−0.062	72.559	−3.183	−2.276	4.704	0.875	−2.637	6.406	0.11	1	3	2.024
NGC4259	+0.239	88.751	−2.996	−1.842	5.200	0.490	−2.500	4.398	0.34	1	0	2.340
NGC4261	+0.222	89.971	−2.256	−1.923	1.830	0.818	−2.073	8.218	0.45	1	1	0.702
NGC4262	+0.110	26.431	−3.600	−2.549	6.946	0.661	−2.524	5.846	0.06	1	2	2.177
NGC4264	−0.049	38.525	−2.751	−1.770	4.377	0.771	−2.506	3.908	0.33	1	0	1.479
NGC4267	−0.394	25.879	−3.318	−2.247	3.263	0.510	−2.545	3.843	0.42	1	1	0.850
NGC4268	+0.142	75.869	−2.909	−2.028	12.010	1.121	−2.425	6.898	0.25	1	1	1.530
NGC4270	+0.257	89.828	−3.567	−2.409	4.891	0.558	−3.873	3.365	0.02	1	1	2.219
NGC4278	+0.489	28.222	−2.561	−2.123	4.161	1.139	−2.090	6.747	0.24	1	1	0.993
NGC4281	−0.015	75.895	−2.742	−2.164	7.764	1.173	−2.502	9.135	0.15	1	2	1.546
NGC4283	−0.010	16.860	−4.279	−2.653	3.837	0.470	−4.212	3.661	0.00	1	1	1.560
NGC4324	+0.173	65.401	−3.029	−1.842	5.187	0.550	−2.546	3.030	0.34	1	1	1.432
NGC4339	−0.089	37.098	−3.876	−2.433	6.346	0.770	−5.129	4.609	0.00	1	0	0.680

Name	β_z	i	$\log_{10}(\rho_s)$	γ'	$\hat{\chi}^2$	$\alpha_{\rm dyn.}$	$\log_{10}(\rho_{{\rm DM},s})$	$M/L_{\rm stars}$	$f_{\rm DM}(R_e)$	Hβ	Quality	$r_{\rm max}/R_e$
(1)	(2)	(3)	(4)	(5)	(6)	(7)	(8)	(9)	(10)	(11)	(12)	(13)
NGC4340	−0.225	89.515	−3.200	−2.043	4.411	0.627	−2.731	4.060	0.39	1	0	0.875
NGC4342	+0.311	89.933	−3.379	−2.457	3.906	1.069	−2.322	9.730	0.04	1	3	5.284
NGC4346	+0.117	76.366	−3.132	−2.083	3.530	0.602	−2.477	4.348	0.20	1	3	1.776
NGC4350	+0.180	87.028	−3.051	−2.194	2.914	0.607	−2.437	6.091	0.13	1	3	2.679
NGC4365	+0.138	89.171	−2.625	−2.099	1.019	0.677	−2.695	5.481	0.19	1	2	0.676
NGC4371	−0.064	89.810	−2.760	−1.871	2.805	0.577	−2.396	5.117	0.40	1	1	0.811
NGC4374	+0.069	87.863	−2.426	−2.058	1.362	0.780	−2.357	6.569	0.23	1	1	0.680
NGC4377	+0.231	33.280	−2.500	−1.738	17.833	0.540	−1.923	3.338	0.49	1	0	1.528
NGC4379	−0.069	88.994	−3.544	−2.232	4.279	0.540	−2.940	3.942	0.13	1	1	1.294
NGC4382	+0.362	46.495	−2.374	−1.800	1.023	0.685	−2.130	4.291	0.65	1	0	0.461
NGC4387	+0.189	89.502	−3.616	−2.219	4.356	0.462	−3.110	3.733	0.10	1	1	1.882
NGC4406	+0.121	89.334	−2.590	−1.991	1.162	0.733	−2.599	5.688	0.35	1	1	0.317
NGC4417	+0.257	80.947	−3.182	−2.138	3.160	0.500	−2.607	4.416	0.17	1	2	1.757
NGC4425	+0.472	89.928	−3.283	−1.865	4.922	0.644	−2.960	4.122	0.25	1	0	2.351
NGC4429	+0.142	89.837	−3.131	−2.325	4.786	0.814	−5.030	6.019	0.00	1	0	1.011
NGC4434	−0.123	89.032	−4.417	−2.698	6.346	0.229	−4.071	2.486	0.02	1	1	1.382
NGC4435	+0.172	68.175	−2.993	−2.085	3.062	0.524	−2.490	4.011	0.22	1	3	1.515
NGC4442	+0.184	72.444	−3.203	−2.323	2.876	0.570	−3.240	4.609	0.03	1	3	1.247
NGC4452	+0.308	88.321	−3.173	−1.778	4.365	0.547	−2.849	5.163	0.26	1	3	4.674
NGC4458	+0.170	45.906	−3.666	−2.155	5.873	0.651	−3.433	3.385	0.09	1	1	1.106

Name	β_z	i	$\log_{10}(\rho_s)$	γ'	$\hat{\chi}^2$	$\alpha_{\rm dyn.}$	$\log_{10}(\rho_{{\rm DM},s})$	$M/L_{\rm stars}$	$f_{\rm DM}(R_e)$	Hβ	Quality	$r_{\rm max}/R_e$
(1)	(2)	(3)	(4)	(5)	(6)	(7)	(8)	(9)	(10)	(11)	(12)	(13)
NGC4459	+0.071	47.000	−2.890	−2.077	3.867	0.808	−2.714	4.370	0.18	1	1	0.851
NGC4461	+0.103	71.007	−3.266	−2.197	3.251	0.631	−2.779	4.384	0.15	1	3	1.293
NGC4472	+0.082	89.754	−2.407	−2.041	0.956	0.819	−4.336	5.519	0.00	1	1	0.358
NGC4473	+0.205	68.481	−2.755	−2.052	1.505	0.548	−2.219	5.267	0.30	1	2	1.537
NGC4474	+0.051	85.966	−3.537	−2.134	5.366	0.475	−2.931	3.189	0.20	1	2	1.780
NGC4476	+0.443	62.827	−3.385	−1.938	7.589	0.677	−2.794	2.945	0.31	0	0	1.560
NGC4477	+0.331	26.191	−2.323	−1.789	2.263	0.845	−1.910	5.395	0.61	1	1	0.628
NGC4478	+0.074	88.615	−3.296	−2.265	3.140	0.659	−3.283	5.196	0.03	1	3	1.808
NGC4483	+0.116	66.720	−3.160	−1.897	4.173	0.563	−2.625	4.362	0.31	1	1	1.390
NGC4486	+0.043	88.790	−2.239	−1.927	1.980	1.316	−5.351	7.523	0.00	1	2	0.567
NGC4486A	−0.025	88.687	−4.673	−2.870	13.077	0.484	−5.145	4.462	0.00	1	1	2.148
NGC4489	−0.490	48.819	−3.062	−1.634	6.459	0.443	−2.578	2.946	0.64	1	0	0.975
NGC4494	+0.033	87.780	−2.781	−1.934	2.914	0.495	−2.402	3.983	0.44	1	1	0.799
NGC4503	+0.205	69.345	−3.275	−2.227	3.389	0.693	−3.006	5.293	0.10	1	3	1.196
NGC4521	+0.204	83.392	−2.609	−1.906	3.859	0.654	−2.330	7.128	0.30	1	3	1.916
NGC4526	+0.164	77.312	−2.836	−2.204	2.988	0.754	−4.664	5.565	0.00	1	1	1.206
NGC4528	−0.135	58.387	−3.313	−2.113	6.557	0.695	−2.563	3.716	0.16	1	2	1.980
NGC4546	+0.168	69.008	−3.159	−2.298	4.093	0.669	−2.519	5.361	0.12	1	3	1.864
NGC4550	+0.248	78.835	−2.802	−1.756	9.409	0.579	−2.393	5.011	0.30	1	3	2.743
NGC4551	+0.148	89.660	−3.342	−2.090	3.556	0.669	−3.025	4.923	0.10	1	2	1.625

Name	β_z	i	$\log_{10}(\rho_s)$	γ'	$\hat{\chi}^2$	$\alpha_{\rm dyn.}$	$\log_{10}(\rho_{{\rm DM},s})$	$M/L_{\rm stars}$	$f_{\rm DM}(R_e)$	Hβ	Quality	$r_{\rm max}/R_e$
(1)	(2)	(3)	(4)	(5)	(6)	(7)	(8)	(9)	(10)	(11)	(12)	(13)
NGC4552	+0.229	30.786	−2.426	−2.014	2.445	0.807	−1.928	6.452	0.42	1	2	0.712
NGC4564	+0.134	75.367	−3.268	−2.239	2.715	0.562	−2.659	4.789	0.14	1	3	2.239
NGC4570	+0.253	82.985	−2.950	−2.114	2.936	0.522	−2.449	4.992	0.16	1	3	2.743
NGC4578	−0.140	50.802	−3.108	−1.988	3.842	0.668	−2.549	4.454	0.44	1	1	1.092
NGC4596	+0.494	37.155	−2.744	−1.954	3.901	0.861	−2.495	4.773	0.35	1	2	0.659
NGC4608	+0.217	25.880	−2.997	−2.002	3.081	0.657	−2.542	4.151	0.44	1	2	0.484
NGC4612	+0.444	41.709	−2.877	−1.763	5.734	0.617	−2.393	2.607	0.58	1	0	0.983
NGC4621	+0.130	79.570	−2.860	−2.168	1.464	0.716	−2.585	5.847	0.18	1	3	0.900
NGC4623	+0.343	89.499	−2.925	−1.568	4.955	0.452	−2.629	4.736	0.50	1	1	2.051
NGC4624	−0.083	83.070	−3.191	−2.148	3.238	0.618	−3.112	4.342	0.17	1	1	0.557
NGC4636	+0.108	89.917	−2.429	−1.820	1.729	0.928	−2.341	7.976	0.41	1	0	0.424
NGC4638	+0.218	78.241	−3.232	−2.117	3.336	0.406	−2.686	3.029	0.14	1	3	3.550
NGC4643	+0.355	25.028	−2.848	−2.103	2.875	0.711	−2.474	4.760	0.23	1	2	0.672
NGC4649	+0.186	48.706	−2.283	−2.017	1.004	1.081	−3.609	6.957	0.01	1	2	0.502
NGC4660	+0.138	71.708	−3.170	−2.229	2.896	0.557	−2.395	4.918	0.12	1	2	2.778
NGC4684	+0.325	74.152	−3.389	−1.913	5.968	1.011	−2.882	2.353	0.26	1	2	1.797
NGC4690	+0.202	58.732	−3.497	−2.230	7.123	1.112	−6.075	3.772	0.00	1	1	1.095
NGC4694	+0.281	72.412	−4.736	−2.585	12.131	0.387	−6.115	1.393	0.00	0	0	1.096
NGC4697	+0.420	67.177	−2.837	−2.043	2.019	0.720	−2.641	4.861	0.24	1	3	0.629
NGC4710	+0.133	89.983	−3.322	−2.143	5.117	0.628	−3.321	4.492	0.08	1	1	2.535

Name	β_z	i	$\log_{10}(\rho_s)$	γ'	$\hat{\chi}^2$	$\alpha_{\rm dyn.}$	$\log_{10}(\rho_{{\rm DM},s})$	$M/L_{\rm stars}$	$f_{\rm DM}(R_e)$	Hβ	Quality	$r_{\rm max}/R_e$
(1)	(2)	(3)	(4)	(5)	(6)	(7)	(8)	(9)	(10)	(11)	(12)	(13)
NGC4733	+0.008	87.515	−3.805	−1.959	9.138	0.641	−6.428	2.240	0.00	1	0	0.900
NGC4753	−0.172	89.198	−2.610	−1.927	3.701	1.025	−3.663	4.251	0.03	1	1	0.689
NGC4754	+0.129	60.130	−2.864	−2.063	3.779	0.619	−2.336	4.745	0.31	1	2	1.188
NGC4762	+0.134	89.685	−2.922	−1.990	3.960	0.355	−2.772	3.733	0.24	1	3	3.049
NGC4803	+0.314	63.805	−2.440	−1.435	6.723	0.357	−2.191	4.936	0.61	1	0	2.215
NGC5103	+0.051	89.740	−3.246	−2.036	5.663	0.407	−2.696	3.488	0.20	1	0	2.949
NGC5173	+0.451	33.889	−3.011	−1.976	10.551	0.796	−2.614	2.452	0.25	1	0	1.830
NGC5198	+0.104	89.725	−3.031	−2.246	3.471	0.794	−4.951	6.158	0.00	1	1	1.165
NGC5273	−0.500	89.919	−3.433	−1.922	6.472	0.908	−3.376	3.013	0.18	1	1	0.879
NGC5308	+0.320	85.495	−2.799	−2.152	3.220	0.620	−2.521	6.613	0.13	1	3	3.422
NGC5322	+0.259	89.603	−2.574	−2.062	3.781	0.972	−2.500	4.829	0.27	1	1	0.807
NGC5342	+0.208	80.534	−2.813	−1.956	18.513	0.760	−2.283	7.027	0.23	1	0	3.100
NGC5353	+0.129	79.581	−2.298	−1.927	5.227	0.616	−2.114	6.912	0.25	1	2	1.962
NGC5355	+0.167	60.153	−2.780	−1.607	7.204	0.853	−2.506	3.743	0.46	0	0	1.715
NGC5358	+0.143	89.898	−2.986	−1.751	5.892	0.646	−2.598	4.859	0.36	1	0	2.198
NGC5379	+0.038	89.866	−3.058	−1.700	11.247	1.559	−2.982	7.952	0.27	0	1	1.751
NGC5422	+0.129	85.021	−2.893	−2.060	5.851	0.679	−2.574	6.072	0.21	1	1	1.983
NGC5473	+0.271	37.746	−2.385	−1.878	3.709	0.777	−2.014	4.848	0.48	1	0	1.037
NGC5475	+0.229	79.080	−2.907	−1.806	5.721	0.664	−2.618	4.818	0.29	1	2	2.686
NGC5481	+0.090	89.166	−3.682	−2.423	10.588	1.111	−5.385	5.466	0.00	1	0	0.951

Name	β_z	i	$\log_{10}(\rho_s)$	γ'	$\hat{\chi}^2$	$\alpha_{\rm dyn.}$	$\log_{10}(\rho_{{\rm DM},s})$	$M/L_{\rm stars}$	$f_{\rm DM}(R_e)$	Hβ	Quality	$r_{\rm max}/R_e$
(1)	(2)	(3)	(4)	(5)	(6)	(7)	(8)	(9)	(10)	(11)	(12)	(13)
NGC5485	+0.134	88.340	−2.645	−1.895	3.388	0.831	−2.399	7.046	0.34	1	0	0.916
NGC5493	+0.008	75.815	−2.789	−1.999	3.538	0.496	−2.475	2.963	0.25	1	3	3.036
NGC5500	+0.100	65.205	−3.530	−2.140	16.579	1.027	−3.327	5.045	0.12	1	0	1.207
NGC5507	−0.041	63.641	−2.917	−2.109	4.075	0.797	−2.373	6.653	0.19	1	3	1.804
NGC5557	+0.145	89.039	−2.862	−2.233	13.722	0.676	−2.788	4.674	0.16	1	1	0.849
NGC5574	+0.426	89.882	−3.541	−2.065	6.907	0.668	−3.182	2.559	0.13	0	0	2.528
NGC5576	+0.130	89.957	−3.514	−2.473	3.997	0.376	−3.041	2.767	0.13	1	2	1.015
NGC5582	+0.389	52.017	−2.924	−2.055	4.858	0.722	−2.436	5.265	0.45	1	1	0.921
NGC5611	+0.166	72.172	−3.375	−2.235	6.206	0.755	−2.678	4.992	0.11	1	3	3.125
NGC5631	+0.002	89.343	−2.955	−2.077	3.158	0.692	−2.540	4.251	0.32	1	0	0.965
NGC5638	+0.214	27.746	−2.365	−1.705	3.288	0.672	−2.074	4.707	0.55	1	0	0.819
NGC5687	+0.067	77.351	−3.030	−2.183	3.730	0.940	−2.566	8.012	0.28	1	1	1.013
NGC5770	−0.018	25.910	−4.396	−2.603	11.072	0.406	−4.089	2.418	0.02	1	0	1.244
NGC5813	+0.057	89.470	−2.425	−1.905	2.535	0.744	−2.204	7.439	0.57	1	0	0.684
NGC5831	+0.105	64.087	−3.108	−2.154	3.617	0.806	−2.809	4.601	0.21	1	0	0.898
NGC5838	−0.029	70.163	−3.074	−2.418	3.429	0.862	−2.899	7.732	0.05	1	3	1.383
NGC5839	−0.170	88.855	−3.650	−2.379	6.435	0.600	−3.059	5.170	0.11	1	0	1.286
NGC5845	+0.190	63.266	−3.840	−2.680	3.360	0.397	−2.723	4.854	0.02	1	3	3.943
NGC5846	+0.115	46.328	−2.337	−1.830	2.303	0.962	−2.422	8.059	0.28	1	1	0.723
NGC5854	+0.238	73.110	−3.218	−2.020	5.141	0.724	−3.115	2.670	0.11	1	3	1.988

Name	β_z	i	$\log_{10}(\rho_s)$	γ'	$\hat{\chi}^2$	$\alpha_{\rm dyn.}$	$\log_{10}(\rho_{{\rm DM},s})$	$M/L_{\rm stars}$	$f_{\rm DM}(R_e)$	Hβ	Quality	$r_{\rm max}/R_e$
(1)	(2)	(3)	(4)	(5)	(6)	(7)	(8)	(9)	(10)	(11)	(12)	(13)
NGC5864	+0.391	75.506	−3.225	−2.081	4.996	0.773	−3.270	3.705	0.09	1	3	2.430
NGC5866	+0.376	89.212	−2.661	−1.860	3.856	0.926	−2.929	4.548	0.09	1	0	1.242
NGC5869	+0.013	86.473	−2.950	−2.128	4.277	0.914	−2.396	7.020	0.31	1	1	1.030
NGC6010	+0.165	84.061	−2.991	−2.099	4.732	0.809	−2.667	5.843	0.15	1	1	2.603
NGC6014	−0.460	85.597	−3.472	−2.116	7.914	1.508	−7.000	4.288	0.00	0	0	0.878
NGC6017	+0.051	88.602	−4.091	−2.526	11.159	0.404	−3.363	2.636	0.05	1	1	3.159
NGC6149	−0.149	85.840	−3.103	−1.925	7.468	0.636	−2.699	4.622	0.28	1	0	2.168
NGC6278	+0.210	66.121	−3.023	−2.273	5.543	0.713	−2.874	5.514	0.09	1	0	2.007
NGC6547	+0.133	89.950	−2.963	−2.160	7.578	0.806	−2.519	6.526	0.17	1	1	2.484
NGC6548	−0.446	18.602	−2.674	−1.941	5.083	1.193	−2.156	7.209	0.62	1	1	0.838
NGC6703	+0.058	26.270	−3.233	−2.330	3.354	0.901	−3.433	5.832	0.05	1	1	0.736
NGC6798	+0.198	72.841	−3.027	−2.029	4.559	0.570	−2.619	4.552	0.24	1	2	2.061
NGC7280	+0.497	52.266	−3.239	−2.077	6.894	1.071	−2.822	3.651	0.24	0	1	1.379
NGC7332	+0.234	83.351	−3.355	−2.210	6.513	0.363	−2.967	2.168	0.10	1	1	3.605
NGC7454	+0.300	60.366	−3.045	−1.948	4.978	1.069	−2.897	5.261	0.19	1	0	1.117
NGC7457	+0.311	65.875	−2.972	−1.592	6.310	0.488	−2.683	3.267	0.54	1	1	1.160
NGC7465	+0.224	88.361	−3.470	−2.128	16.508	0.560	−2.853	2.297	0.17	0	0	2.444
NGC7693	+0.334	42.606	−3.384	−1.906	8.734	1.830	−3.280	4.005	0.16	0	1	1.303
NGC7710	+0.227	76.217	−3.773	−2.263	11.581	0.431	−3.040	3.257	0.10	1	1	2.901
PGC016060	+0.214	76.400	−3.030	−1.863	11.383	0.679	−2.705	4.439	0.23	0	2	4.320

Name	β_z	i	$\log_{10}(\rho_s)$	γ'	$\hat{\chi}^2$	$\alpha_{\rm dyn.}$	$\log_{10}(\rho_{{\rm DM},s})$	$M/L_{\rm stars}$	$f_{\rm DM}(R_e)$	Hβ	Quality	$r_{\rm max}/R_e$
(1)	(2)	(3)	(4)	(5)	(6)	(7)	(8)	(9)	(10)	(11)	(12)	(13)
PGC028887	+0.445	59.413	−3.032	−1.994	6.372	1.017	−2.518	7.149	0.31	1	0	2.015
PGC029321	−0.473	89.522	−2.786	−1.319	15.375	0.341	−2.561	2.878	0.73	0	0	1.698
PGC035754	+0.337	56.481	−3.946	−2.453	10.568	0.550	−3.171	3.565	0.11	1	1	1.927
PGC042549	+0.285	54.539	−3.150	−2.002	6.103	0.917	−2.750	3.227	0.19	1	1	2.438
PGC044433	+0.408	89.796	−3.130	−2.072	4.514	0.740	−2.544	6.184	0.16	1	1	2.863
PGC050395	+0.275	54.966	−2.549	−1.368	9.330	0.483	−2.329	4.377	0.69	1	0	1.796
PGC051753	+0.376	72.635	−3.066	−1.746	6.251	0.639	−2.744	4.986	0.31	1	1	2.836
PGC054452	+0.500	41.530	−3.364	−1.913	7.111	1.164	−3.056	3.757	0.22	1	1	1.642
PGC056772	+0.372	65.700	−3.606	−2.176	11.274	1.010	−3.237	3.938	0.12	0	1	2.554
PGC061468	+0.192	89.694	−2.562	−1.252	15.619	0.608	−2.435	7.305	0.75	0	0	1.693
PGC170172	+0.083	89.610	−3.483	−1.890	49.108	0.486	−2.974	1.639	0.26	1	0	2.294
UGC03960	+0.080	88.894	−3.587	−2.165	15.637	1.120	−3.340	5.361	0.19	1	0	0.866
UGC04551	−0.040	75.622	−3.408	−2.394	3.619	0.489	−2.619	4.772	0.08	1	2	2.465
UGC05408	−0.499	89.133	−6.000	−3.234	19.254	0.048	−5.031	1.537	0.00	0	0	2.501
UGC06062	+0.198	57.472	−2.851	−1.946	4.122	0.767	−2.409	5.838	0.28	1	1	1.923
UGC06176	−0.500	89.791	−2.798	−1.742	11.767	1.817	−2.500	5.092	0.34	0	0	1.677
UGC08876	+0.312	89.880	−3.612	−2.416	5.967	0.642	−2.945	5.562	0.06	1	1	3.057
UGC09519	+0.052	66.392	−3.295	−2.000	7.782	1.056	−2.739	3.696	0.17	0	1	3.700

Name	β_z	i	$\log_{10}(\rho_s)$	γ'	$\hat{\chi}^2$	$\alpha_{\rm dyn.}$	$\log_{10}(\rho_{{\rm DM},s})$	$M/L_{\rm stars}$	$f_{\rm DM}(R_e)$	Hβ	Quality	$r_{\rm max}/R_e$
(1)	(2)	(3)	(4)	(5)	(6)	(7)	(8)	(9)	(10)	(11)	(12)	(13)

Table A1: A table of galactic properties, as found using the General Power Law method of Chapter 4. Column (1): The galaxy name. Column (2): The best-fitting value of the vertical anisotropy. Column (3): The best-fitting value of inclination, in degrees. Column (4) The best-fitting value of the total mass-density at the break radius, in [$M_\odot\,pc^{-3}$]. Column (5): The best-fitting value of the total mass-density profile slope. Column (6): The reduced χ^2 (χ^2 per degree-of-freedom) of the JAM model fit to the data, computed from the values of Columns (2)-(5). Column (7): The best-fitting value of the $\alpha_{\rm dyn.}$ parameter. Column (8): The best-fitting value of the global scaling of the dark matter mass-density at the break radius, in [$M_\odot\,pc^{-3}$]. Column (9): The best-fitting M/L from JAM for the mass-follows-light model. This is the only model that allows the dynamical M/L to be fit for, and so these values were used as a consistent baseline throughout this work. Column (10): The fraction of dark matter within $1\,R_e$. Column (11): A flag denoting those galaxies with sufficiently small observed Hβ emission (< 2.3Å), from Table 1 of Cappellari et al. (2013b). Column (12): A rating of the data and model quality, from 0 (very poor data quality) to 3 (excellent data quality and model fit), from Table 1 of Cappellari et al. (2013a). Column (13): The ratio of $r_{\rm max}$ to R_e. All results of this work (except the dark matter fractions) were constrained by $r_{\rm max}$, rather than R_e, since some of these ratios are less than 1.